KU LEUVEN

ARENBERG DOCTORAL SCHOOL
Faculty of Science

Tuning Shear Banding and Wall Slip in Entangled Polyelectrolytes by Intermolecular Interactions

Hu TANG

Supervisors:
Prof. dr. Pavlik Lettinga
Prof. dr. Carmen Bartic

Dissertation presented in partial fulfillment of the requirements for the degree of Doctor of Science (PhD): Physics

March 2018

Tuning Shear Banding and Wall Slip in Entangled Polyelectrolytes by Intermolecular Interactions

Hu TANG

Examination committee:
Prof. dr. Christian Maes, chair
Prof. dr. Pavlik Lettinga, supervisor
Prof. dr. Carmen Bartic, supervisor
Prof. dr. Christian Clasen
Prof. dr. Enrico Carlon
Prof. dr. Jan Karel George Dhont
Prof. dr. Renko de Vries
(Far Away)

Dissertation presented in partial fulfillment of the requirements for the degree of Doctor of Science (PhD): Physics

March 2018

Uitgegeven in eigen beheer, Hu TANG, Celestijnenlaan 200d box 2416, B-3001 Leuven (Belgium)

Preface

I would like to express my special appreciation and thanks to my supervisor Prof. Pavlik Lettinga. Thank you for always being supportive along the way. I would also like to thank Prof. Carmen Bartic, Prof. Enrico Carlon, and Prof. Christian Clasen for serving as my supervisory committee members even at hardship. I would like to extend my gratitude to Dr. Emmanuel Stiakakis for the patient guidance in the DNA experiments. Without his help, this thesis would not be possible. Dr. Hartmut Kriegs is thanked for building up the heterodyne light scattering setup and being helpful on the experiments. Miss Tatiana Kochetkova helped me with some of the experiments on xanthan. It was enjoyable experience working with her. I would especially like to thank Prof. Jan K.G. Dhont for the good atmosphere in the group and all the group members in Juelich soft matter group for being kind and helpful all the time. I acknowledge the Chinese Scholarship Council for financial support to work here.

I feel deeply indebted to my friends and family. Words cannot express how grateful I am to my mother-in-law, father-in-law, my mother, and father for all of the sacrifices that they've made on my behalf. I would also like to thank all of my friends who supported me in the last 4 years, and encouraged me to strive towards my goal. At the end I would like express appreciation to my beloved wife Yuanying Liang who is always my support in the moments when there is no one there.

Abstract

The study of flow instabilities such as shear banding and wall slip in entangled polymers is of great significance for both fundamental science and industry. There is, however, an ongoing debate in the polymer rheology community whether shear banding is generic for polymers. This discussion is involved as the molecular mechanism for shear banding in entangled polymers is poorly known and the interplay of shear banding with wall slip makes the problem even more complicated. Therefore we try to answer three questions in this thesis: 1) Is shear banding a generic phenomenon for entangled polymers or a more system-specific phenomenon? 2) Will the shear banded systems always show classic shear banded velocity profiles, with a constant shear rate within both bands, independent of the applied shear rate? 3) What is the molecular mechanism for shear banding in entangled polymers?

In order to address these questions, we performed in this thesis standard rheology measurements, birefringence and velocity profile experiments in order to characterize the linear and non-linear flow behavior of polymers for which the interactions and properties can be tuned. Polyelectrolytes are a logical choice, as both the interactions and particle properties can be tuned by varying the ionic strength. To access the generic character, we used two different polyelectrolytes, namely the semi-flexible xanthan and DNA. In addition, we synthesized an attractive polymer system namely DNA grafted with PNIPAm, which becomes hydrophobic above a critical temperature. This allowed us to also access the effect of attraction.

We demonstrate that shear banding and wall slip in entangled xanthan and DNA can be finely tuned by intermolecular interactions such as the electrostatic repulsions and intermolecular attraction. For xanthan and DNA we observe sharp shear banding at low ionic strength, though for DNA there is a strong competition with wall slip. The sharp interfaces broaden upon addition of salt, up to a point at high salt where no shear bands are observed and the velocity profile becomes linear. We introduced a new analysis method to quantify this

broadening and also the difference between a shear thinning factor as obtained from the rheological flow curve and the velocity profile. For the attractive PNIPAm-DNA we find a reentrant behavior as upon increasing temperature first wall slip is suppressed in favor of shear band formation, while shear banding is suppressed when the system tends to gel. These observations suggest that shear band formation is generic for polymers when they are sufficiently stiff and when the friction between the polymers is low. Shear banding is suppressed when the disentangled polymers can easily collapse either by screening the charges along its backbone or increasing attraction. The mechanism of suppression is related with the widening of the interface. We claim that generally polymeric systems that display a curvature in the velocity profile which is stronger than expected from the rheology, do display shear banding, but with an interface which is too broad for the gap of the shear cell geometry.

Beknopte samenvatting

Het onderzoek aan stromingsinstabiliteiten, zoals bandformatie onder afschuiving, is van groot fundamenteel belang zowel als van belang voor de industrie. Er is echter een voortgaande discussie in de gemeenschap van polymeer rheologen of deze bandvorming generiek is voor polymeren. Dit is een ingewikkelde discussie aangezien het moleculaire mechanisme voor de band formatie van polymeren slecht begrepen is en de wisselwerking tussen band formatie en glijden aan de wand maakt de discussie no ingewikkelder. Daarom proberen wij drie vragen te beantwoorden in dit proefschrift: 1) is de formatie van afschuifbanden een generiek fenomeen voor verstrikte polymeren of is het meer een systeem-specifiek probleem? 2) Zullen systemen die deze bandformatie ondergaan klassieke bandvorming laten zien, waar de afschuifsnelheid constant is binnen beide banden, onafhankelijk van de afschuif snelheid) 3) Wat is het moleculaire mechanisme voor de formatie van de afschuifbanden in het geval van verstrikte polymeren?

Om deze vragen te behandelen hebben wij in dit proefschrift standaard rheologische experiment, dubbel-brekingsexperimenten en stromingsprofiel metingen gedaan om het lineaire en niet-lineaire stromingsgedrag te karakteriseren van polymeren, waarvan de interacties en eigenschappen afgestemd kunnen worden. Polyelectrolyten vormen een logische keuze, aangezien de interactie zowel als de deeltjes eigenschappen afgestemd kunnen worden door het zoutgehalte van de oplossing te variëren. Om het generieke karakter te bestuderen hebben wij twee verschillende polyelectrolyten gebruikte, namelijk xanthaan en DNA. Bovendien hebben wij een attractief polymeer systeem gesynthetiseerd door een laag PNIPAm, dat hydrofoob wordt boven een kritische temperatuur, aan te brengen op DNA. Dit stelt ons in staat om ook het effect van aantrekking te bestuderen.

Wij laten zien dat afschuifbanden en glijden aan de wand in verstrikt xanthaan en DNA fijn afgestemd kan worden door intermoleculaire interacties zoals elektrostatische afstoting en intermoleculaire aantrekking. Voor xanthaan en

DNA nemen wij scherpe afschuifbanden waar bij lage zoutsterkte, hoewel er bij DNA een harde competitie is tussen glijden aan de wand en bandformatie. De grensvlak tussen de banden verbreedt wanneer zout wordt toegevoegd, tot het punt bij hoge zout sterkte waar geen banden maar waargenomen worden en het stromingsprofiel homogeen is. Wij introduceren een nieuwe analyse methode om deze verbreding te kwantificeren en om het verschil te bepalen tussen de stromingsverdunning factor die wij uit stromingskurves verkrijgen en welke wij uit het stromingsprofiel halen. Voor de PNIPAm-DNA vinden we een herintreding met toenemende temperatuur omdat eerst glijden aan de wand onderdrukt wordt, zodat afschuifbanden kunnen ontstaan, terwijl bij het verdere verhogen van de temperatuur afschuifbanden onderdrukt worden wanneer het systeem een gel lijkt te vormen. Deze observaties suggereren dat het formeren van afschuifbanden is generiek wanneer het polymeer stijf is en wanneer de wrijving tussen de polymeren gering is. De formatie van banden wordt onderdrukt wanneer de ontrafelde polymeren makkelijke kunnen instorten doordat de lading afgeschermd is of door de toegenomen aantrekking. Het mechanisme voor de onderdrukking houd verband met het verbreden van het grensvlak. Wij stellen dat over het algemeen polymeren waarvoor de kromming in het stromingsprofiel sterker is dan verwacht afgaande op de rheologie, wel afschuifbanden hebben, maar met een grensvlak dat zo breed is dat het niet in de spleet van de gebruikte geometrie past.

List of Abbreviations

AFM	atomic force microscopy
CT DNA	calf thymus deoxyribonucleic acid
DMF	dimethylformamide
DNA	deoxyribonucleic acid
EDTA	ethylenediaminetetraacetic acid
HDLS	heterodyne dynamic light scattering
LAOS	large amplitude oscillation shear
LCST	lower critical solution temperature
NHS ester	N-hydroxysuccinimide ester
NMR	nuclear magnetic resonance
PBD	polybutadiene
PIV	particle imaging velocimetry
PMT	photomultiplier
PNIPAm	poly(N-isopropylacrylamide)
PS	polystyrene
PWLF	piece wise linear function
SBI	shear banding instability
STF	shear thinning function
Tris-HCl	tris(hydroxymethyl)aminomethane hydrochloride
USV	ultrasound velocimetry
UV	ultraviolet
UV-Vis	ultraviolet–visible spectroscopy

List of Symbols

σ	shear stress
η	shear viscosity
η_0	zero shear viscosity
V	velocity
$V(0)$	velocity of the inner cylinder
$V(R_2 - R_1)$	velocity at position $R_2 - R_1$
$V(x)$	velocity at position x
ω	angular velocity
V_0	applied velocity
V_1	apparent velocity
V_s	slip velocity
V_s/V_0	relative slip velocity
$\triangle V$	residue of a fit to the experimental data
Γ	torque
L	length of blob of the shear cell
C	constant
d	gap distance
$\dot{\gamma}$	shear rate
$\dot{\gamma}_{app}$	applied shear rate
$\dot{\gamma}_{eff}$	effective shear rate
$\dot{\gamma}_{true}$	true shear rate
$\dot{\gamma}_x$	shear rate at position x
$\dot{\gamma}_{high}$	shear rate of the high shear rate band
$\dot{\gamma}_{low}$	shear rate of the low shear rate band
ϵ	fraction of the high shear rate band in the gap
W_{int}	interface width between the low and high shear rate bands
m	shear-thinning exponent
m_{fc}	shear thinning exponent derived from flow curve
F	force
A	area

$g_2(\tau)$	intensity auto-correlation function
B	base line
A_0, A_1	amplitude of the correlation function
τ	correlation time
x	distance from the outer cylinder
R_1, R_2	radius of the inner and outer cylinder of the Couette shear cell
c	concentration
$c*$	overlap concentration
t	time
G'	storage modulus
G''	loss modulus
I	ionic strength
I_b	birefringence intensity
f_c	crossover frequency
T	temperature
Z	entanglement number
D_{eff}	effective diameter
l_p	persistence length

Contents

Beknopte samenvatting v

List of Symbols xi

Contents xi

List of Figures xv

1 Introduction 1

1.1 Rheological Tests 2

1.2 What is Gradient Shear Banding? 4

1.3 A Minimal Model for Gradient Banding 6

1.4 Shear Banding Systems 9

1.5 Experimental Techniques: Velocimetry and Shear Cell 11

1.6 Organization of the Thesis 13

2 Velocity Profiling: Experiment and Analysis 15

2.1 Introduction 15

2.2 Spatially Resolved Heterodyne Light Scattering 17

2.3 Analysis of Velocity Profiles 19

2.4 Summary 25

3 Shear Banding in Xanthan **27**

3.1 Introduction 27

3.2 Materials and Methods 29

3.3 Results 30

3.3.1 Rheology 30

3.3.2 Velocity Profiles 35

3.3.3 Birefringence Measurements 45

3.4 Discussion 47

3.5 Summary 49

4 Shear Banding and Wall Slip in DNA **51**

4.1 Introduction 51

4.2 Material and Methods 53

4.3 Results 57

4.3.1 Gel Electrophoresis 57

4.3.2 Rheology 57

4.3.3 Velocity Profiles and Analysis 61

4.3.4 Diagram of States and Birefringence 62

4.4 Discussion 64

4.5 Summary 67

5 Shear Banding and Wall Slip in DNA-PNIPAm **68**

5.1 Introduction 68

5.2 Material and Methods 69

5.2.1 Materials 69

5.2.2 Synthesis of DNA-PNIPAm Brushlike Polymer 70

5.2.3 Gel Electrophoresis 71

5.2.4 Rheology 71

5.2.5 Velocity Profile Measurements 72
5.3 Results and Discussion 73
5.3.1 Gel Electrophoresis 73
5.3.2 Rheology 74
5.3.3 Velocity Profile and Analysis 80
5.4 Discussion 84
5.5 Summary 86

6 Conclusions **87**

Bibliography **91**

List of Figures

1.1 The flow behavior of four different materials as characterized by flow curves of the viscosity vs shear rate representation (a) and stress vs shear rate (b): Newtonian (black); shear thinning (red); shear thickening (blue); yield stress fluid (green). 2

1.2 Velocity profiles for homogeneous shear flow (a), wall slip (b) and shear banding (c). d refers to the gap distance. v is the applied velocity on the moving plate and v_s is the slip velocity which can occur on either (both) the moving or (and) the stationary plate. 3

1.3 Gradient banding in a co-centric couette cell (a) and a cone-plate or plate-plate cell (b). In both case the shear rate has two distinct values when moving in the direction where the velocity varies from the velocity at the wall $\mathbf{v}_{wall}$ to the standing wall, and hence in the gradient direction of the velocity as indicated by $\nabla\mathbf{v}$. Both shear rates can be associated with a local viscosity. . 5

1.4 Shear banded flow:(a) Viscosity vs. shear rate for a shear thinning fluid, with the different shear rate regions.(b) Shear stress vs. shear rate., with unstable (black line) and meta-stable (dashed lines) region. The horizontal section is the stress plateau, bordered by he vertical dash lines, indicating the shear rates in the high and low shear band, respectively. 5

2.1 (a)Experimental setup for velocity profile measurement along the gradient direction.(b)Schematics of the setup.(c) Unit vector of incident beams and the scattered light and the interference fringe of the incident beams, γ is the beam crossing angle and θ is the scattering angle. 16

2.2 Typical correlation functions and its fits by Eq. 2.1:(a) good fit due to single frequency,(b) bad fit due to multiple frequencies. . 17

2.3 (a) linear velocity profiles, (b) shear banded profiles with sharp interface, (c) curved velocity profiles with broad interface, and (d-e) corresponding velocity profiles with wall slip. Vs is slip velocity. 20

2.4 (a) Schematics showing the geometry of the shear cell, ω_0 is the applied angular velocity. R_1 and R_2 are the radii of the inner and outer cylinder. (b) Calculated velocity profiles depending on different shear thinning factor m for a shear rate of 50 s^{-1} using eq. 2.8 with fixed Radii of $R_1 = 22.5\ mm$ and $R_2 = 24\ mm$, which is the same as the shear cell we use. (c) Calculated velocity profiles depending on different R_2 for a shear rate of 50 s^{-1} using eq. 2.8 with fixed m of 0.1. 21

2.5 Logic flowchart for velocity profile analysis 22

2.6 Interface width determination of a classic banded velocity profile(a) and a curved velocity profile(c):for a shear banded veloctity profile the slopes of PWLF fit are defined by true high and low shear rate in the bands $\dot{\gamma}_{low}$ and the $\dot{\gamma}_{high}$ while the slops for the PWLF fit of a curved velocity profile are shear rates calculated from the shear thinning function near the wall. The corresponding residues of the PWLF fits from the velocity profile are given in (b) and (d) and the interface width is determined by fitting the residue from the crossover linearly toward the x axis. 23

3.1 The viscosity vs. shear rate (a) and zero shear viscosity vs. concentration (b) for xanthan in water at 20 ^oC. The numbers in (b) show the slopes of zero viscosity dependence on concentration in different concentration regimes. 30

3.2 The stress development in startup shear flow for 0 M(a), 5 mM(b), 10 mM(c) and 1 M(d) added salt concentration for 0.7 wt% xanthan 31

3.3 (a) The storage G' and loss modulus G'' and (b) the stress σ in the stationary state as a function of the shear rate $\dot{\gamma}$, for various xanthan concentrations without added salt. (c) is the same as in (a), and (d) the same as in (b), but now for various salt concentrations at a fixed xanthan concentration of $0.7\,wt\%$. The lines in (b) and (d) are linear fits to the experimental data, which indicate the sloped stress plateaus, with an indication of the shear-thinning exponent m_{fc} , which is defined as $\sigma \sim \dot{\gamma}^{m_{fc}}$. Note that the fitting range is from 1 to $100 s^{-1}$. 32

3.4 Master curves for the storage G' and loss modulus G'' by (a) time-concentration and (b) time-ionic strength superposition. The shifts of the logarithmic frequency scale are indicated in the figures. 33

3.5 Velocity profiles at different shear rates at various xanthan concentrations and added salt concentrations, as indicated. The color bar indicates the applied shear rate in s^{-1}. 34

3.6 The suspension velocity as a function of the position in the gap of the Couette cell, for the $0.7\,wt\%$ sample with no added salt. (a) Velocity profiles for applied shear rates up to $50\,s^{-1}$, and (b) from 50 up to $130\,s^{-1}$. The numbers on the right axis indicate the applied shear rate. The dashed curves through the data points are guides-to-the-eye, while the straight lines correspond to the linear profiles near the walls of the shear cell. 35

3.7 Reproducibility of velocity profiles: (a) 3 data points are taken at each position with an interval of 3 seconds per point. The insert shows the magnification of the 3 data points. (b) a comparison between two repeated measurements taken at an interval of 30 minutes. Velocity profile were taken at $30 s^{-1}$ for $0.7 wt\%$ xanthan with no added salt. 36

3.8 (a) Typical velocity profiles for the $0.7 wt\%$ xanthan with no added salt. The numbers indicates the applied shear rate in s^{-1}. The vertical dash lines indicated the position where the correlation functions are shown. (b) Correlation functions at varying positions from the stationary outer cylinder shown on the bottom for different shear rates which are indicated on the left. 37

3.9 (a) Typical velocity profiles at $50s^{-1}$ for varying added salt concentration for $0.7wt\%$ xanthan. The vertical dash lines indicated the position where the correlation functions are shown. (b) Correlation functions at varying positions from the stationary outer cylinder shown on the bottom for different salt concentrations which are indicated on the left. 38

3.10 The determination of interface width W_{int} for the $0.7\,wt\%$ xanthan concentration, for two velocity profiles. (a) A broad interface with the shear-thinning function fit given by the red curve. The blue lines are linear curves with a slope equal to that of the slope of the shear-thinning function at the walls of the shear cell. Panel (b) illustrates the determination of the width W_{int} of the interface from the residual ΔV. (c) For a relatively sharp interface, the corresponding linear curves in blue are determined directly from the data points near the wall of the cell. The slopes of the linear curves are taken as the high shear rate $\dot{\gamma}_h$ and low shear rate $\dot{\gamma}_l$, respectively. The fraction of high shear rate band ϵ is thus defined by the crossover of the two linear curves. The same procedure is used to determine the interface width, as plotted in (d). 39

3.11 The width of the shear-band interface as a function of the applied shear rate, for the samples of 0.7 $wt\%$ xanthan without added salt and with 5 and 10 mM added salt. The open points are for sharp interfaces, the filled symbols for broad interfaces. The solid lines are guides-to-the-eye. Note that the gap width is $1.5\,mm$. 42

3.12 The lever-rule plot for $0.7\,wt\%$ xanthan without added salt (solid circles), and for the $5\,mM$ salt (open squares), where the fraction ϵ of the volume occupied by the high shear-rate band is plotted against the applied shear rate. The data points are based on the determination of ϵ from the velocity profiles with a sharp interface. The vertical dashed lines indicate the resulting range $6 - 113\,s^{-1}$ of applied shear rates where shear-banding occurs. The inset shows the shear rates in the high and low shear-rate bands as a function of the applied shear rates (in s^{-1}) for the system without added salt. 43

3.13 The difference of the exponents m_{fc} as determined from the flow curve and m as determined from the shear-thinning-function fit for $0.7\,wt\%$ xanthan, with $0\,M$, $5\,mM$ and $10\,mM$ added salt. The solid lines are guides-to-the-eye. The vertical dashed lines indicate the shear-banding region as obtained from the lever-rule plot. The gap in the data for the sample without salt is due to the fact that the interface is too sharp to be able to be well fitted with the shear-thinning function. Typical errors in the data points are ± 0.05. 44

3.14 The diagram-of-states in the added-salt-concentration I versus the shear-rate plane, where velocity profiles are distinguished depending on the shear-thinning parameter m. The open points refer to banded profiles with a sharp interface. The black solid curves indicate m higher or lower than m_{fc}, which is about 0.2. The vertical dashed lines indicate the shear-banding region as obtained from the lever rule. 45

3.15 (a)The transmitted intensity I_b and (b) images taken between crossed polarizers at varying applied shear rate for 0.7 $wt\%$ xanthan solutions at different salt concentrations.The lines indicate the boundaries shown in Fig. 9. The flow and vorticity direction are indicated by the arrows and the scale bar is $3cm$. 46

4.1 Gel electrophoresis of the samples on 0.5% agrose gel under 130 V for 3 hours at room temperature. Lane 1-5 are $10kb$ DNA, $20kb$ DNA, Calf thymus DNA, $30kb$ DNA and Lambda DNA which has a Mw of $48.5kb$, respectively. 54

4.2 (a) The storage G' and loss modulus G'' and (b) the stress σ in the stationary state as a function of the shear rate $\dot{\gamma}$, for 6 mg/ml Calf Thymus DNA with 0.01 M, 0.1 M and 1 M salt at 20 ^oC. The inset in (a) shows the magnification of the crossover frequency. The lines in (b) are linear fits to the experimental data, which indicate over what range the shear-thinning exponent m_{fc} , as defined by $\sigma \sim \dot{\gamma}^{m_{fc}}$, was determined. 55

4.3 Stress development in startup shear at various shear rates, as indicated in the legend in s^{-1}, for 6 mg/ml Calf Thymus DNA with 0.01 M (a), 0.1 M (b) and 1 M (c) added salt at 20^oC. . . 56

4.4 Steady state velocity profiles at different shear rates which are indicated in the color bar in s^{-1} for 6 mg/ml Calf Thymus with 0.01 M (a), 0.1 M (b) and 1 M (c) added salt at 20 ^oC. The open points indicate the applied velocity for each shear rate. . . 58

4.5 (a) Relative slip velocity V_s/V_0; (b) the difference of the exponents m_{fc} as determined from the flow curve and m as determined from the shear-thinning-function fit; (c) the width of the shear-band interface versus applied shear rate for 6 mg/ml Calf Thymus DNA at different ionic strengths as indicated in the figure. The solid lines are guides-to-the-eye. Note that the gap width is 1.5 mm. 59

4.6 The lever-rule plots for 6 mg/ml with 0.01 M added salt, where the fraction ϵ of the volume occupied by the high shear-rate band is plotted against the effective shear rate(a) and applied shear rate(b). The data points are based on the determination of ϵ from the velocity profiles with a sharp interface. The inset in (b) shows the shear rates in the high and low shear-rate bands as a function of the applied shear rates (in s^{-1}) for the system with 0.01 M added salt. 60

4.7 The diagram-of-states in the ionic strength I versus the applied shear-rate plane, where velocity profiles are distinguished depending on the shear-thinning parameter m. The open points indicated by the black dash line refer to banded profiles with a sharp interface(when R^2 of the PWLF fit overtakes the R^2 of the ST fit). The black solid curves indicate m higher or lower than m_{fc}, which is about 0.2. The region below the red solid line displays substantial wall slip($> 20\%$). 62

4.8 The transmitted intensity I_b at varying applied shear rate for 6 mg/ml DNA solutions at different salt concentrations. 63

4.9 Images taken between crossed polarizers at varying applied shear rate for 6 mg/ml DNA solutions at different salt concentrations.The flow and vorticity direction are indicated by the arrows and the scale bar is 0.5 cm. 63

5.1 Structure of the DNA-PNIPAm brushlike polymer synthesized by a photoreaction between DNA and PsoPNIPAm 70

5.2 Gel electrophoresis of the samples at 6 ^oC under 130 V for 3 hours. Lane 1 to Lane 6 are DNA, DNA-PNIPAm with low grafting density, DNA-PNIPAm with high grafting density and their denatured counterparts, respectively. 72

5.3 The storage G' and loss modulus G'' from 20 to 50^oC for DNA(a), DNA-PNIPAm brush-like polymer with low PNIPAm grafting density(b), and DNA-PNIPAm brush-like polymer with high PNIPAm grafting density(c). The crossover frequency vs. temperature for the samples(d).The lines are guilds to the eyes. 73

5.4 The stationary stress σ versus the shear rate $\dot{\gamma}$ from 20 to 50 ^oC, for DNA (a), DNA-PNIPAm brush-like polymer with low grafting density (b), and DNA-PNIPAm brush-like polymer with high grafting density (c). (d) The slope of the plateau for the flow curves m_{fc} vs. temperature for all samples. Note that the values plotted in (d) correspond to the slopes of the second plateau in case two plateaus are present, i.e. between $\dot{\gamma} = 1 - 100\ s^{-1}$. The lines are guilds to the eyes. 74

5.5 The stationary stress σ versus the shear rate $\dot{\gamma}$ from 20 to 50 ^oC on a linear scale in the low shear rate region for DNA, DN-PNIPAm with low grafting density(b) and DNA-PNIPAm with high grafting density(c). The lines show the extrapolation to zero shear at 20 and 50 ^oC.(d) Yield stress σ_{yield} for all samples at different temperatures. 75

5.6 Velocity profiles at different shear rates for DNA at 20 ^oC(a), 35 ^oC(b), and 50 ^oC(c). The open points indicate the applied velocities for each shear rate. The applied shear rates in s^{-1} are indicated in the color bar. 77

5.7 Velocity profiles at different shear rates for DNA-PNIPAm brush-like polymer with low PNIPAm grafting density at 20 ^oC(a), 25 ^oC(b), 30 ^oC(c), 35 ^oC(d), 40 ^oC(e), 45 ^oC(f), and 50 ^oC(g). The open points indicate applied velocities for each shear rate. The applied shear rates in s^{-1} are indicated in the color bar. . 78

5.8 Velocity profiles at different shear rates for DNA-PNIPAm brush-like polymer with high PNIPAm grafting density at 20 ^oC(a), 25 ^oC(b), 30 ^oC(c), 35 ^oC(d), 40 ^oC(e), 45 ^oC(f), and 50 ^oC(g). The open points indicate applied velocities for each shear rate. The applied shear rates in s^{-1} are indicated in the color bar. . 79

5.9 (a-c) Relative slip velocity V_s/V_0, (d-f) The difference of the exponents m_{fc} as determined from the flow curve and m as determined from the STF fit, and (g-i) the width of the shear-band interface at various temperature as indicated in the figure versus applied shear rate for 6mg/ml DNA, DNA-PNIPAm brush-like polymer with low PNIPAm grafting density, and DNA-PNIPAm brush-like polymer with high PNIPAm grafting density. The lines are guides-to-the-eye. Typical errors in the data points are ± 0.05 for $m_{fc} - m$. 81

5.10 The lever-rule plot at various temperatures for 6mg/ml DNA (a), DNA-PNIPAm brush-like polymer with low PNIPAm grafting density (b), and DNA-PNIPAm brush-like polymer with high PNIPAm grafting density (c), where the fraction ϵ of the volume occupied by the high shear-rate band is plotted against the true shear rate, so after correction for the slip. The data points are based on the determination of ϵ from the velocity profiles with a sharp interface. The lines are guides to the eyes. 82

5.11 The diagram-of-states in the temperature T versus the applied shear-rate plane, where velocity profiles are classified depending on the shear-thinning parameter m which is indicated by the color bar. The open points refer to banded profiles with a sharp interface. The black solid curves indicate the region where more than 20% wall slip occurs. The arrows in (b) show the re-entrance of linear velocity profiles from shear banded velocity profiles . . 83

Chapter 1

Introduction

Everything flows. This famous saying due to the Greek philosopher Heraclitus is the motto of the branch of science called 'rheology', the logics of flow. Rheological measurements are standard used to characterize materials and typically yield the viscosity of a material, when it is a fluid, or the modulus, when it is a solid. Many materials have, however, a dual character, where the fluidity depends on the time scale at which the material is probed and the force with which the material is deformed. The material can soften or harden, so it can turn into a solid or fluid, depending on the applied field. These are complex fluids. Complex fluids was the term for what nowadays is called Soft Matter, after de Gennes [1]. Soft Matter can be deformed with moderate force, as the constituents, so the particles that are suspended in some host solvent, are Brownian due to the constant bombardment of solvent molecules. Soft Matter is often divided into three types of materials: colloids, polymers, and membranes. As such, most biological materials as well as many industrial products can be considered as soft matter.

The properties of many materials, such as the viscosity, can dramatically change as the materials is subjected a shearing field, quantified by the shear rate $\dot{\gamma}$, which we will define below, see 1.1. With increasing shear flow the viscosity can increase, shear thickening, or decrease, shear thinning. Some material initial behave like a solid, but starts to flow when the applied stress exceeds the yield stress σ_{yield}. As a result of this non-linear behavior (see 1.1b), it might happen that the resulting flow becomes unstable even at very low flow rates where inertia does not play a role. The material may separate, for example, in regions with different viscosity and velocity profile, or it can stay intact as it slips only at the all. Flow instabilities are interesting from a fundamental point of view, but

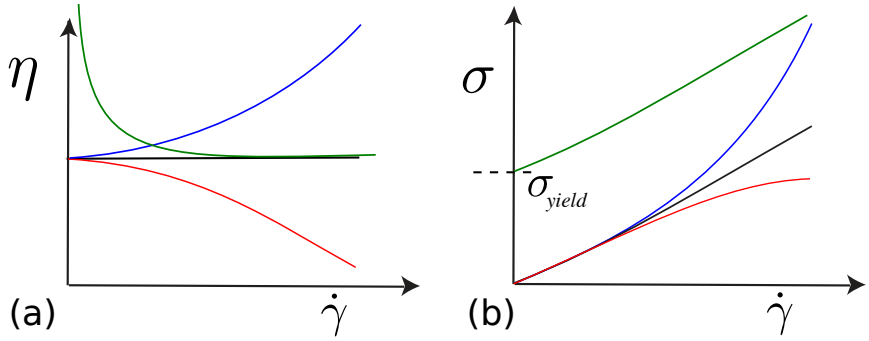

Figure 1.1: The flow behavior of four different materials as characterized by flow curves of the viscosity vs shear rate representation (a) and stress vs shear rate (b): Newtonian (black); shear thinning (red); shear thickening (blue); yield stress fluid (green).

its understanding is also of practical use as they might interfere with standard rheological characterization or cause problems when transporting the complex fluids. Industrial polymer processing, for example, sees huge wastage through product defects through phenomena like sharkskin, melt fracture, roughness of the extrudate, which are caused by unstable flows during processing.[2, 3, 4] An understanding of these phenomena could avoid wastage on a rational basis, and lead to the production of materials with better quality at lower cost. In this respect the behavior of polymeric systems is of particular interest and this is the focus of the thesis.

In this introduction we will first discuss the most basic rheological concepts and also the geometries that are used to perform rheological experiments. Then we will introduce the concept of 'gradient Banding' which is one of the main instabilities that is encountered in the flow of complex fluids. A minimal model for gradient banding is introduced in order to explain the connection between shear banding and extreme shear thinning. Here we will also give an overview of typical systems that display gradient banding and techniques used for shear banding study.

1.1 Rheological Tests

In the rheological characterization of complex fluids, one typically assumes that the flow is laminar. This is a flow that can be thought of as being composed of sliding layers of fluid. For such flows, one can define the shear rate $\dot{\gamma}$ as the

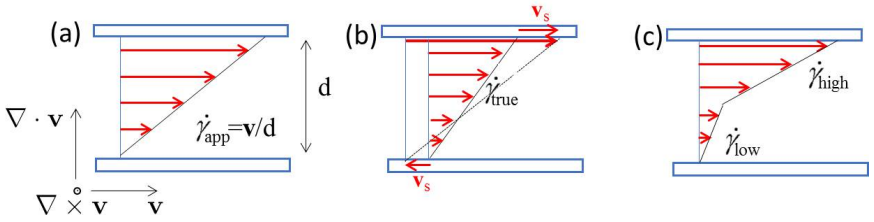

Figure 1.2: Velocity profiles for homogeneous shear flow (a), wall slip (b) and shear banding (c). d refers to the gap distance. v is the applied velocity on the moving plate and v_s is the slip velocity which can occur on either (both) the moving or (and) the stationary plate.

spatial derivative of the flow velocity in the direction y perpendicular to the sliding layers,

$$\dot{\gamma} \;=\; \frac{dv(y)}{dy} = v/d, \tag{1.1}$$

for a plate-plate geometry with a gap of d, where the top plate is moving with a velocity v as compared to the bottom plate,see Fig. 1.2a. The shear rate is usually an experimental control parameter, while a standard rheology experiment then probes the mechanical response as a function of the shear rate. In particular, the stress σ is probed, which is defined as the force per unit area that is needed to sustain a given shear rate. This force is proportional to the shear rate, which accounts for the velocity differences between the sliding layers of fluid, and the proportionality constant accounts for the friction force between the sliding layers, which is by definition the shear viscosity η,

$$\sigma \;=\; \eta\,\dot{\gamma} \tag{1.2}$$

Since flow affects micro-structural order, and thus friction between sliding layers, the viscosity is in general a function of the shear rate. A decrease of the viscosity with increasing shear rate is referred to as shear thinning, contrary to shear thickening for cases where the viscosity increases.

The shear rate dependence of the viscosity suggests that complex fluids can be characterized by one or more relation times. The reason is that complex fluids actually never behave as pure fluids but also have a solid-like component, which actually causes non-Newtonian behavior. The most straightforward way to characterize this visco-elasticity is by subjecting the material to an oscillatory deformation with some amplitude γ_0 and frequency ω. In the case of shear flow

this is given by a time-dependent strain of

$$\gamma(t) = \gamma_0 \sin(\omega t). \tag{1.3}$$

This is the so called dynamic test. Again, when applying this oscillatory deformations the strain amplitude γ_0 should be chosen such that the sample does not change its character and that no slip occurs. When this is the case then the response is generally given by

$$\sigma(t) = G^* \gamma_0 \sin(\omega t + \delta) = [G' \sin(\omega t) + G'' \cos(\omega t)]\gamma_0. \tag{1.4}$$

The sample can thus be characterized by the dynamic modulus G^* and the phase angle δ, or equivalently by the storage modulus G' and loss modulus G''. The system behaves like a solid when $G' \gg G''$ and $\delta = 0^o$, and like a fluid when $G' \ll G''$ and $\delta = 90^o$. The system is visco-elastic when $G' \approx G''$ or $0 < \delta < 90^o$. Most complex fluids will show transitions as a function of the applied frequency, where the $G'(\omega)$ and $G''(\omega)$ cross. These crossing frequencies are important because they hint to relaxation times within the system, which couples back to the shear rate where flow instabilities could be expected as the system does not have enough time to react. For that reason dynamic frequency sweeps are a prerequisite to characterize systems before testing them for flow instabilities.

1.2 What is Gradient Shear Banding?

There are two common assumptions in the rheological characterization of complex fluids, namely

- There are no instabilities or flow-induced phase transitions that lead to strongly inhomogeneous velocity profiles. When such phenomena occur, they will affect the measured stress, and thus prohibit standard rheological measurements of, for example, the viscosity.

- The velocity of the fluid at the geometry boundaries is the same as the velocity of the boundary itself, like the upper moving plate in Fig.1.2a. This condition is commonly referred to as a no-slip or stick boundary condition. When such conditions are not fulfilled, the sample partly slips along the boundary, as depicted in Fig.1.2b, so that the true applied shear rate becomes unknown.

For many systems these conditions are not fulfilled and, depending on the applied shear rate, the will be instable and/or wall slip will occur. One of

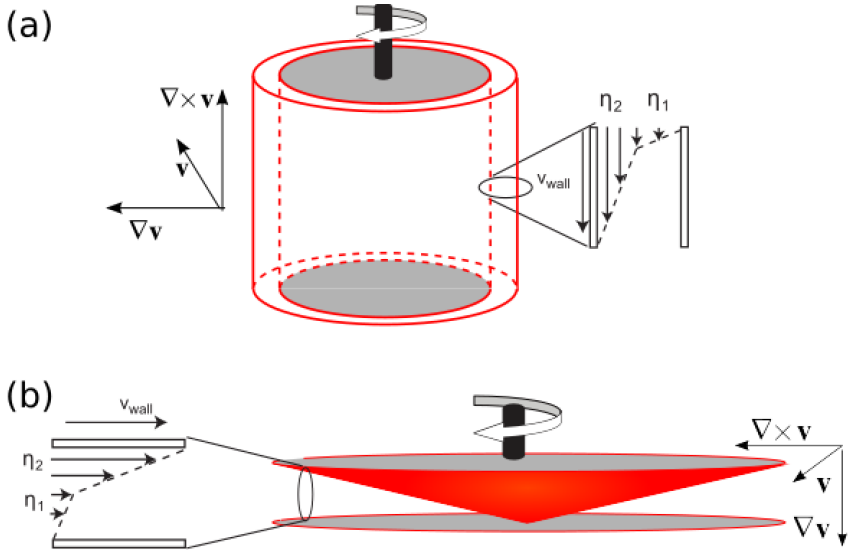

Figure 1.3: Gradient banding in a co-centric couette cell (a) and a cone-plate or plate-plate cell (b). In both case the shear rate has two distinct values when moving in the direction where the velocity varies from the velocity at the wall $\mathbf{v}_{wall}$ to the standing wall, and hence in the gradient direction of the velocity as indicated by $\nabla\mathbf{v}$. Both shear rates can be associated with a local viscosity.

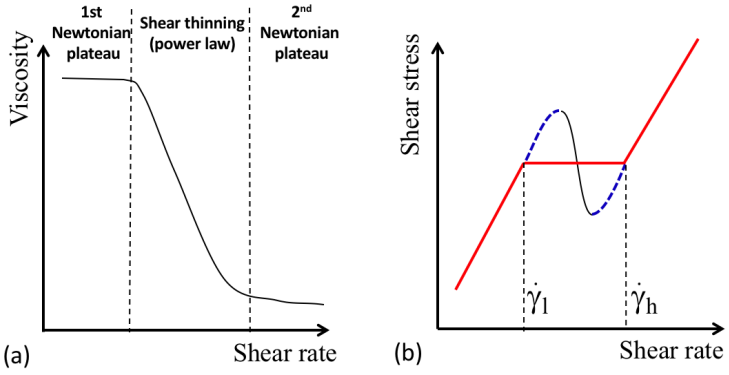

Figure 1.4: Shear banded flow:(a) Viscosity vs. shear rate for a shear thinning fluid, with the different shear rate regions.(b) Shear stress vs. shear rate., with unstable (black line) and meta-stable (dashed lines) region. The horizontal section is the stress plateau, bordered by he vertical dash lines, indicating the shear rates in the high and low shear band, respectively.

the most common instabilities is usually referred to as *gradient shear banding*, where in the stationary state two regions (the "bands") with different shear rates coexist, as depicted in Fig.1.2c. Gradient banding and slip phenomena are often found to occur simultaneously. Fig. 1.3 shows how gradient banding can be thought of in two typical measuring geometries: a cone-plate cell and a cocentric couette cell. It is important to know under which conditions these phenomena occur, while the molecular reasons for the occurrence of instabilities and slip are interesting in itself. Thus, the study of flow instabilities and wall slip is crucial for the understanding of the flow behavior of complex fluids.

Shear banding usually comes aside with extreme shear thinning, that is, with a strong decrease of the shear viscosity with increasing shear rate, as schematically plotted in Fig. 1.1 and again in Fig.1.4. When extreme shear thinning occurs for a homogeneously sheared system, the shear stress can decrease with increasing shear rate, that is $d\sigma(\dot{\gamma})d\dot{\gamma} < 0$ (as depicted by the black line in Fig.1.4b). As will be discussed below, a homogeneous velocity profile is unstable in such cases (see, for example, Refs.[5, 6, 7, 8]). The initially homogeneous velocity profile now evolves into a stationary shear banded velocity profile (Fig.1.2c). When the stress is measured after shear banding has fully developed, the stress now exhibits a plateau in an intermediate shear rate regime, as schematically indicated by the red curve in Fig.1.4b. The stress plateau can be positively sloped, however, due to specific features such as polydispersity, shear-induced mass transport, and/or a variation in orientational order [9, 10]. In the high- and low shear rate regime, the viscosity is independent of the shear rate. Such shear rate regimes are commonly referred to as Newtonian plateaus, as indicated in Fig.1.4a).

1.3 A Minimal Model for Gradient Banding

The most simple empirical model [5, 11, 12] that describes shear banding, and leads to an understanding of its most important characteristics, is as follows.

Let us first show that a linear velocity profile is unstable when the stress decreases with increasing shear rate. Consider without loss of generality a laminar velocity profile in a two-plate geometry, with x the flow direction, and with y the gradient direction. The standard Navier-Stokes equation reads in this case,

$$\rho_m \frac{\partial v(y,t)}{\partial t} = \frac{\partial \sigma(y,t)}{\partial y} \tag{1.5}$$

with ρ_m the specific mass density of the fluid. The local velocity of the linear velocity profile is equal to $\dot{\gamma}$, which is perturbed with a small velocity $\delta v(y,t)$, that is, $v(y,t) = \dot{\gamma}\, y + \delta v(y,t)$. This expression for the velocity is substituted into eq.(1.5), and subsequent linearization with respect to δv, gives,

$$\rho_m \frac{\partial v(y,t)}{\partial t} = \frac{\partial^2 \delta v(y,t)}{\partial y^2} \frac{d\,\sigma(\dot{\gamma})}{d\,\dot{\gamma}} \tag{1.6}$$

where it is assumed that the stress is solely determined by the local shear rate, complying with the standard expression (1.2) for the stress. Decomposing $\delta v(y,t)$ in sinusoidally varying components with wavelengths $\Lambda = 2\,\pi/k$, with k the wave vector, leads to the following equations of motion for each of these Fourier components,

$$\rho_m \frac{\partial \tilde{v}(k,t)}{\partial t} = -k^2 \frac{d\,\sigma(\dot{\gamma})}{d\,\dot{\gamma}} \delta\tilde{v}(k,t) \tag{1.7}$$

where $\delta\tilde{v}(k,t)$ denotes the amplitude of each of the sinusoidal modes, that is, the Fourier transform of $\delta v(y,t)$. Hence,

$$\delta\tilde{v}(k,t) = \delta\tilde{v}(k,t=0)\, \exp\left\{-k^2\, \rho_m^{-1} \frac{d\,\sigma(\dot{\gamma})}{d\,\dot{\gamma}}\, t\right\} \tag{1.8}$$

This result shows that when $d\sigma(\dot{\gamma})/d\,\dot{\gamma} < 0$, the initial perturbation growth exponentially in time, which implies that the homogeneous velocity profile is unstable. Very strong shear thinning leads to the van der Waals loop-like dependence of the stress as a function of shear rate as depicted in Fig.1.2c by the black curve. In cases of very strong shear thinning, a homogeneous velocity profile is therefore unstable.

The above linear stability analysis shows that perturbations with an arbitrary small wavelength, corresponding to arbitrary large wave vectors k, grow arbitrarily fast. This implies that the standard Navier-Stokes equation (1.5) is insufficient to describe shear banding. The standard expression (1.2) for the stress, which states that the stress is a function of the shear rate, is formally derived as the leading term in an expansion of the stress with respect spatial gradients of the shear rate. Within the typically narrow region that connects the two bands, which is referred to as the *interface* between the bands, spatial variations of the shear rate are sufficiently large that the above mentioned formal expansion of the stress with respect to the shear rate must be extended to include the next higher order term. This leads to [5, 11, 12],

$$\sigma(y,t) = \eta(\dot{\gamma}(y,t))\, \dot{\gamma}(y,t) - \kappa(\dot{\gamma}(y,t)) \frac{\partial^2 \dot{\gamma}(y,t)}{\partial y^2} \tag{1.9}$$

where we denoted the position and time dependence explicitly. The parameter κ is referred to as the *shear-curvature viscosity* [5]. Since the additional contribution to the stress is related to higher order derivatives of the shear rate, such contributions are referred to as *non-local stresses*. Non-local stresses can alternatively be included implicitly by adding a stress-diffusion contribution to an equation of motion for the stress [12, 13, 14, 15, 16].

There are a few omissions in the constitutive equation (1.9):

- The concentration dependence of the stress is not accounted for. Concentration differences between the bands are thus neglected.

- Elastic stresses are not considered. Such stresses come into play when one of the bands develops a yield stress.

- Phase transitions induced by flow are assumed not to occur.

- Normal stresses, in directions perpendicular to the flow direction, are not considered.

Let us first ask about the stress σ_{plat} that is selected corresponding to the plateau in the flow curve, that is, the stress where the plateau in Fig.1.4b occurs. First of all, the Navier-Stokes equation (1.5) implies that the stress in the stationary state is constant throughout the sample. According to the constitutive equation (1.9), we therefore have that the constant value of the stress in the stationary state is equal to,

$$\sigma_{stat} \;=\; \eta(\dot\gamma(y))\,\dot\gamma(y) - \kappa(\dot\gamma(y))\,\frac{d^2\dot\gamma(y)}{dy^2} \tag{1.10}$$

For a constant shear rate within both bands, we have,

$$\int_{\dot\gamma_l}^{\dot\gamma_h} d\dot\gamma\;\frac{d^2\dot\gamma(y)}{dy^2} \;=\; \tfrac{1}{2}\int_{y_-}^{y_+} dy\;\frac{d}{dy}\left(\frac{d\dot\gamma(y)}{dy}\right)^2 \;=\; 0 \tag{1.11}$$

where $\dot\gamma_h$ and $\dot\gamma_l$ denote the shear rates within the band with the highest and lowest shear rate, respectively, and where y_+ and y_- are positions within the two bands. It thus follows from eq.(1.10) that,

$$\int_{\dot\gamma_l}^{\dot\gamma_h} d\dot\gamma\;\frac{\eta(\dot\gamma)\,\dot\gamma - \sigma_{stat}}{\kappa(\dot\gamma)} \;=\; 0\;, \tag{1.12}$$

This is the *stress-selection rule* that complies with the minimal model [5, 11, 12]. The complex fluid will thus select a stress σ_{stat} in its stationary state such that

eq.(1.12) is satisfied. As a result the low shear rate band the viscosity is high and in the high shear rate band the viscosity is low, following eq. 1.2. For a shear-rate independent shear-curvature viscosity, the stress selection rule implies an equal-area Maxwell construction of the flow curve of the homogeneously sheared system.

Note that the shear rates within the two bands are independent of the applied shear rate. This follows from the fact that the banded velocity profiles remain to be a solution of the Navier-Stokes equation for all applied shear rates independent of the location of the interface. The location of the interface, however, depends on the applied shear rate, so as to match stick boundary conditions. Since the shear rates within the bands uniquely connect to the corresponding stress, this also explains the constant value of σ_{stat} of the plateau stress, independent of the applied shear rate. In addition, this implies that the relative extent of the bands as a function of the applied shear rate obey the so-called lever rule, stating that the extent of the bands is proportional to the applied shear rate. Experiments [17, 18, 19, 20, 21, 22] and computer simulations [23] confirm these predictions and this will be also frequently used throughout the thesis.

1.4 Shear Banding Systems

So far we did not use any specific information about the system other then that it should have sufficient shear thinning in order to form shear bands. Indeed, gradient shear banding has been observed in a large variety of systems, which all have in common that they display strong shear thinning. Gradient banding involving a shear-induced new phase has been observed for lamellar surfactants, where an "onion phase" is induced [24, 25, 26], for poly-crystalline colloids [27, 28, 29] and micellar cubic phases [30, 31], where crystals are shear-melted. For systems with a yield stress, shear-banding can also occur due to shear-gradient induced mass transport, without any shear thinning [10, 32, 33, 34].

The hallmark of shear-banding systems are, however, wormlike micelles, which can be considered as stiff and living polymers. In these systems shear can induce breakage of the constitutive chains as well as alignment [17, 18, 35, 36, 37, 38, 39], which both contribute to the stress relaxation required for strong shear thinning. Theoretical models for worms concerned with banding can be found in Refs.[13, 40, 41]. The same features are shared by supra-molecular polymer solutions, which even display two banding regimes[42]

Systems that show no alignment, but which are transient can also display shear banding[43, 44]. Vise versa, there are many systems which do not have a transient character, but where shear induced alignment causes extreme

shear thinning, resulting in shear banding. This includes complex systems like thermotropic side chain liquid crystal polymers [45], and hexagonal phases of surfactant solutions [46]. There are, however, quite a few semi-flexible rod-like systems, or for the same matter stiff polymers, where shear induce nematic-like ordering causes shear thinning and shear banding, such as actin filaments[47], and block-copolymer worm-like micelles[48].

Thus, literature indicates that both stiffness and the transient character worm-like micelles can cause shear banding independently. The questions is if can also be caused due to the polymeric character of a system, so in other words, due to the fact that systems can be highly entangled. Polymers can display shear thinning, but does this necessarily mean that polymeric systems can form shear bands? This is the main question we want to address in this thesis. Stress plateaus for polymeric systems are generally not very pronounced [49, 50], while the shape of the measured flow curves is very sensitive of the experimental conditions [51, 52, 53]. Shear-banded states for entangled polymers have been reported, but this extremely depends on the experimental conditions. Shear-banding is mainly observed as a transient state in LAOS (Large Amplitude Oscillation Shear) and startup experiments on polybutadiene [54, 55, 56, 57] and DNA solutions [58, 59, 60, 61]. For DNA shear banding could be suppressed by a ramp-up or quench down shear protocol. Therefore, it has been suggested that these stationary shear banded states are meta-stable[61]. Control experiments on entangled polybutadiene and polystyrene are reported in Refs.[62, 63, 64, 65], where it is concluded that there is no shear banding neither in transient nor steady state. Moreover, no clear shear banded velocity profiles are observed in many of the experiments where shear banding is claimed, but rather highly curved profiles. Such curved velocity profiles can also occur, however, when shear banding is absent, for example due to the stress gradient in a Couette cell in combination with a strong shear thinning fluid.

Overall the questions on shear banding in entangled polymers are:

1) Is shear banding a generic phenomenon for entangled polymers or a more system-specific phenomenon?

2) Will the shear banded systems always show classic shear banded velocity profiles in the sense of the minimal model described above, with a constant shear rate within both bands, independent of the applied shear rate and with a typically narrow interface?

3) What is the molecular mechanism for shear banding in entangled polymers?

A factor that complicates the discussion is that not only shear banding but also wall slip (see Fig.1.2c) is observed for many systems[19, 66, 67]. Wall slip is especially a prominent process for entangled polymers [55, 68, 69]. It is

believed to be due to a sudden disentanglement of the polymer chains in the bulk from those in the mono-layer adsorbed at the wall. Since wall slip is always related to the interaction between polymer solution and the solid surface, it is of course system specific and thus difficult predict. For polymeric systems, studies show a relation between wall slip and the roughness of the shear cell, the entanglement number(or bulk strength) and hydrophobicity of the solution. Wang et al[58, 60] showed that the wall slip in entangled DNA solution can be suppressed by sanded shear cell [61]. Limited studies have investigated the interplay between wall slip and shear banding in entangled polymers, though for worm-like micelles it has been shown that wall slip competes with shear banding [67]. While wormlike micelles can release stress by chain breakage, we want to further explore if the competition between wall slip and shear banding is also at hand for polymers whose segments are chemically bonded.

1.5 Experimental Techniques: Velocimetry and Shear Cell

In this thesis, the flow stability is studied for complex fluids composed of entangled polymeric systems. The main signature of a flow instability is when the velocity profile throughout the gap of a shear cell is nonlinear, as it should linear for the case of Newtonian fluids. This study therefore requires that the velocity is measured at the highest possible spatial and time-resolution, while deviations of a linear flow profile need to be interpreted in view of the macroscopic response of the system as measured by rheology. Commonly used velocimetric techniques used in combination with rheology are particle tracking velocimetry(PTV), ultrasound velocimetry(USV) and nuclear magnetic resonance(NMR), optical coherence tomography velocimetry(OCT) and laser Doppler velocimetry(LDV).

PTV[54, 65] is based on the measurement of the velocity of the individual particles tracked in the flow field. The particles are illuminated by a laser sheet(in a thin plane) and the low density of seeded particles allow for the tracking each of them individually for several frames. It has a high time and spatial resolution($1\mu m$), however the sample needs to be transparent since it is usually based on optical methods. Moreover, tracer particles might affect the rheological response.

In comparison to PTV, USV[67, 70] is non-optical imaging technique using ultrasound. Therefore, it is specially useful for optically opaque fluids. However, contrasts agents have to be seeded into the sample so that it scatters the high frequency pulses used. It has a lower spatial resolution of about $100\mu m$. A

full velocity profile can be obtained typically in 0.02s to 2s depending on the required accuracy.

NMR[68, 71] is based on the fact that nuclei in a magnetic field absorb and re-emit electromagnetic radiation. It has a good spatial resolution of a few tens of μm without any requirement for optical transparency. Furthermore,it can also give us the structure information of the sample such as the molecular orientation at the same time. However, it is rather slow. Normally, tens of minutes are required to constructed a single velocity profile because the acquisition time is long. Moreover, molecular labeling is compulsory and the equipment itself is costly to implement.

OCT[72, 73] is an imaging technique that uses coherent light to capture micrometer resolution, two- and three-dimensional images from within optical scattering media.Typically used light source is near-infrared light. The use of relatively long wavelength light allows it to penetrate into the sample to about 2mm. However, sometimes particles have to be added into the sample in order to get sufficient scattering. The resolution at shear rates lower than 1 s^{-1} need to be improved and the signal to noise ratio can be problem sometimes. Furthermore, it takes about 10 minutes to construct the velocity profile.

The experimental technique we applied is a differential Laser-Doppler velocimeter which is based upon the Doppler shift of scattering of light from the sample[74]. In general, it has the following characteristics. First, the sample is optically transparent without any tracing particles, meaning it is noninvasive to the flow of the sample. Second, the spatial resolution is in the order of 100 μm, such that one obtains between the 10 and 20 independent points throughout the gap of the shear cell. This is important for good resolution of the interface between the bands. Finally, the time needed per point is in the order of a few seconds and the whole time needed to construct a velocity profile is several minutes. The time revolution is sufficient for the stable steady state velocity profiles. We will describe the details of the technique in the following chapter.

The shear cells used in these studies can be co-centric couette, plate-plate, or cone plate geometry, see Fig. 1.3. Each of these geometries has its own advantages and drawbacks. For example, there is a free edge for plate-plate and cone plate geometry, where edge fracture would also produce unstable flow, which is not necessary shear banding[64, 65, 75, 76]. Especially for polymer melts the rod-climbing effect can be observed in co-centric couette shear cell, due to the stretching of the polymer chains in solution generated by the rotation of the rod, which can result in a positive normal forces and the fluid rising up the rod. This would also lead to unstable flow. However, for the systems we use, we do not observe rod climbing even for the highest applied shear rates. Therefore for the velocity profile measurements, we use a co-centric couette

shear cell. Still, the inhomogeneous stress distribution in the co-centric couette shear cell in combination with a shear thinning fluid can lead to the curved velocity profile. The distinction between true shear banding and curvature in the velocity profile due to shear shinning is not clearly made in literature[77]. This issue will be addressed in the next chapter.

1.6 Organization of the Thesis

The goal of this thesis is to investigate the nature of flow instabilities in entangled polymers by answering the three questions in the previous paragraph. In order to do so, we used polymers for which the interactions and properties can be tuned, and tested for these systems the linear and non-linear flow behavior. Polyelectrolytes are a logical choice, as both the interactions and particle properties can be tuned by varying the ionic strength.

DNA is, apart from the carrier of genetic information, also an important model poly-electrolyte. Flow instabilities in sheared DNA have been reported as well as the dependence on ionic strength [37]. This study was rather limited, especially in the analysis of the velocity profiles. Moreover, it is questionable if the results for DNA are generic. For that reason we study in Chapter 3 the flow behavior of xanthan, a highly charged polysaccharide. Xanthan is a popular product in many industrial applications exactly for the same reason why it is interesting for us, as the rheology can be strongly modified already at low concentrations of xanthan. Although xanthan is a relatively ill-defined polymer, it shares important features with DNA, as they are both stiff and highly charged. The ionic strength dependence of xanthan, is stronger than for DNA: The persistence length of DNA changes from 54 nm in 10mM salt to 35 nm in 3 M NaCl [78] while for xanthan the persistence length varies from 417 nm in pure water to 150 nm in $0.1 - 0.5$ M KCl [79]. In Chapter 4 we revisit the ionic strength dependence of flow instabilities in DNA suspensions. We will show that there are indeed surprising similarities in the flow behavior of both systems.

These two systems are however limited in the sense that in terms of the interaction between the particles only repulsion is tunable as the Debye length, which is a measure of the range of repulsion, changes from 0.3 nm at 1M ionic strength to 3nm at 0.01M ionic strength at 25 ^oC in water. It could however be that attraction is actually the key player. For that reason we developed an attractive polymer system namely DNA grafted with PNIPAm. The introduction of PNIPAm on the DNA backbone adds an intermolecular attraction on DNA chains when the PNIPAm chains undergo a coil-to-globule

transition at elevated temperatures. In Chapter 5, temperature effects on the wall slip and shear banding in entangled DNA-PNIPAm brush-like polymers are presented. Before we start off describing the flow behavior of these tunable systems, however, we will introduce in Chapter 2 the way we measure velocity profiles using the heterodyne light scattering setup, and the way we analyze these profiles, as we are going to use this throughout the thesis. In the analysis we will introduce the concept of the width of the interface and contrast this to curvature of the velocity profile due to the combination of shear thinning and curvature of the shear cells. Finally, in Chapter 6 we summarize the conclusion and give an outlook as we do give answers but certainly not all answers.

Chapter 2

Velocity Profiling: Experiment and Analysis

2.1 Introduction

The central theme of this thesis is the study of the stability of shear flow for complex fluids of entangled polymeric systems. The main signature of a flow instability is when the velocity profile throughout the gap of a shear cell is nonlinear, as it should linear for the case of Newtonian fluids. Hence, there is the experimental requirement that the velocity needs to be measured at the highest possible spatial and time-resolution, while deviations of a linear flow profile need to be interpreted in view of the macroscopic response of the system as measured by rheology. In this chapter we will introduce both the experimental set-up used to acquire velocity profiles as well as the analysis methodology we choose to analyze the velocity profiles. Both the experimental set-up and analysis will then be used later in chapters 3 to 5.

As mentioned, the experimental technique we applied is a differential Laser-Doppler velocimeter in combination with an optically transparent Couette shear cell of co-centric cylinders. In general, it has the following characteristics. First, the spatial resolution is in the order of 100 μm, such that one obtains between the 10 and 20 independent points throughout the gap of the shear cell. This is important for good resolution of the interface between the bands. Second, the time needed per point is in the order of a few seconds, depending on the contrast. Finally, the sample needs to be optically transparent. In the experimental section we will explain this technique in detail. We will also show

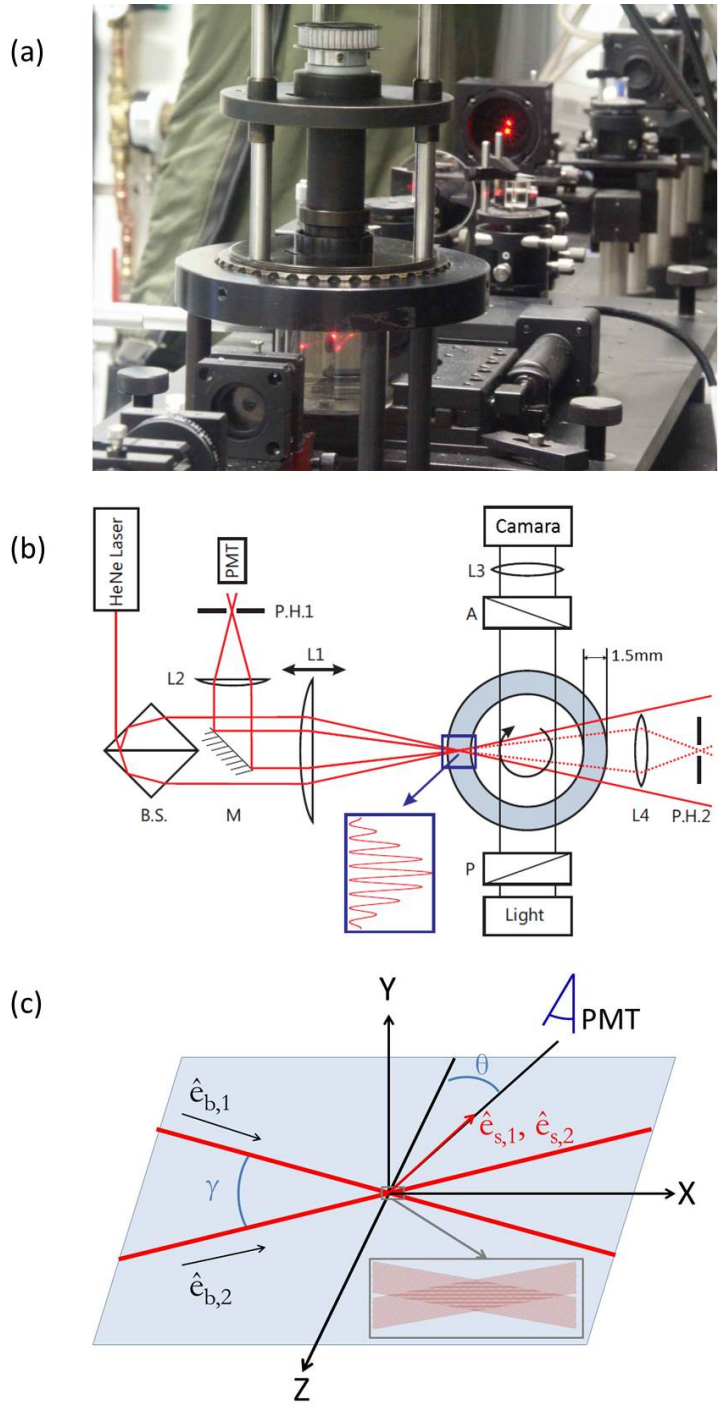

Figure 2.1: (a)Experimental setup for velocity profile measurement along the gradient direction.(b)Schematics of the setup.(c) Unit vector of incident beams and the scattered light and the interference fringe of the incident beams, γ is the beam crossing angle and θ is the scattering angle.

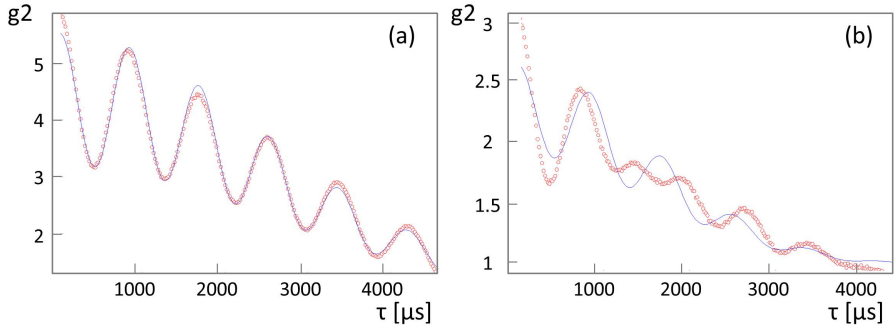

Figure 2.2: Typical correlation functions and its fits by Eq. 2.1:(a) good fit due to single frequency,(b) bad fit due to multiple frequencies.

later that the time-resolution of the laser Doppler velocimetry is sufficient for our purposes as we use optical transparent samples.

The analysis of the flow profiles is a more fundamental issue that has been addressed in many papers[50, 77]. Generally, the first and second derivative are calculated to find the local shear rate and the interface between shear bands, where the shear rate changes between the shear bands. Still, there are ambiguities in the interpretation of the profiles. One main reason is that the combination of a shear thinning fluid and the intrinsic curvature of a shear cell, such as a Couette cell, will always render a non-linear profile, which dos not necessarily mean that the flow is unstable. In many experiments, especially on polymeric systems, this distinction between a shear banded state and a curved velocity profile is not clearly made[57, 59, 80]. Often the profiles are categorized as shear banding, though the mentioned shear thinning in combination could also yield an equally curved profile[19, 77]. In view of this ambiguity we develop here criteria for a proper categorization which we again will use in the chapters 3 to 5. This chapter is thus organized as follows. We first introduce the experimental set up and then discuss the analysis methodology.

2.2 Spatially Resolved Heterodyne Light Scattering

Velocity profiles were measured along the gradient direction in an optical Couette cell by heterodyne dynamic light scattering (HDLS). In this technique laser beams are combined inside the shear cell to produce an interference pattern,

see the inset of Fig. 2.1b and c. When particles pass through they will generate an oscillating signal with a oscillation frequency of Δf, which will be observed when correlating the signal. Δf is the measured Doppler frequency, which is directly related the the local velocity of sample that passed through the measurement volume. As shown in Fig. 2.1, a He-Ne laser beam is split into two beams by the beam splitter and then focused by the lens L1 at the same point within the gap of the shear cell, by which a standing interference pattern is created, see Fig. 2.1b. The extent of the overlap volume of the two lasers is about 100 micron with a beam waist of about 20 micron, see Fig. 2.1c. The lens L1 is mounted on a motorized translation stage, in order to sweep the focal point through the gap. The lenses L2 or L4 focus the scattered light through pinholes onto a photomultiplier(PMT), which is connected to a correlator with a linear time spacing. The vertical optical train in Fig. 2.1a is used to image structures under flow using a camera. Images of the sample during steady shear were taken between two crossed sheet polarizers using a white light box. Both a back- and forward-scattering configuration with a difference about a factor of 10 in the scattering wave vector can be used, for slow and fast decaying correlation functions. Here in this thesis, all the measurements are done using the back scattering configuration.

Typical correlation functions are shown in Fig 2.2. The function is fitted by,

$$g_2(\tau) = B + A_0 e^{-\tau/t_{lin} - (\tau/t_{sqr})^2} [A_1 + e^{(-\tau/t_{flu})^2} \cos(2\pi\tau/t_{osc})] \tag{2.1}$$

where B is the base, A_0, A_1 are the amplitudes, t_{lin} and t_{sqr} are linear and squared decay of the oscillation which are related to the Brownian motion of the particles and the motion of particles passing through the measurement volume, and t_{osc} is the period of the correlation function ($t_{osc} = 1/\Delta f$) which is directly related to the local velocity. The velocity at each point in mm/s is then given by,

$$V = (1/t_{osc})[\lambda/2sin(\gamma/2)] \tag{2.2}$$

The factor $\lambda/2sin(\gamma/2)$ here is the fringe spacing, λ is the wavelength of the beam and γ is the beam crossing angle as shown in Fig.2.1c. The local velocity at each position is calculated according to the frequency shift and the velocity profile is thus constructed for a applied shear rate. Note that the correlation function can show multiple frequencies due to fluctuation of the velocity within measurement time. In this case, the correlation function cannot be well fitted to equation 2.1 see Fig. 2.2b and the measured velocity should not be trusted.

As mentioned before, the time-resolution of heterodyne light scattering as a technique is rather low, since it needs a few seconds to construct the correlation function at each measurement volume. The construction of a velocity profile takes several minutes[74]. Therefore direct measurements of fluctuations in the velocity profile, which could affect the interpretation of the results, are not possible. Despite of the fact that velocity profiles will be always taken when the steady state in the viscosity measurements has been reached, we still critically review the stability of the velocity profile on the base of the HDLS data in order to demonstrate that the shear flow is steady in all occasions.

The stability of the velocity profiles can be tested at three different time scales. First, velocity profiles can be at a time interval of half an hour or longer and checked if the results stay the same within the error bar. In this way we can confirm that the velocity profiles describes the steady state of the system. At a time scale of a few seconds the stability can be tested by measuring at a fixed position three times in a row. Each measurement takes about three seconds. The local flow is assumed to be stable when the points overlap within the experimental error of about 5%. The resultant averaged velocities are used in all the profiles presented. Finally, we check the stability at the shortest time scale of less than three seconds by comparing the correlation functions under the different conditions. The minima in the oscillations of the correlation functions display an upturn exactly in the region where the interface width is sharpest. The minimal in the oscillations of the correlation functions become level when moving away from this region. This suggests that in the latter case single frequencies are measured, therefore a single velocity is probed over a time of three seconds. We will show in the next chapter in detail as an example of how the stability of the velocity profiles are checked. In this way, we are convinced that the velocity profiles presented in this thesis are steady state velocity profile and the HDLS technique is sufficient to measure the velocity profiles.

2.3 Analysis of Velocity Profiles

Fig. 2.3 shows typical velocity profiles for the samples studied in this thesis. For an applied velocity V_0, a linear velocity profile(see Fig. 2.3a) and classic shear banded velocity profile(see Fig. 2.3b) would be observed if there is no wall slip. However, in many experiments both from us and other groups, the velocity profiles do not usually show linear or classic banded velocity profiles with sharp interface between the two bands[80, 81]. Rather, profiles will have a shape somewhere in-between, namely a curved velocity profile with a broad interface, as shown in Fig. 2.3c. In addition, sometimes wall slip might occur,

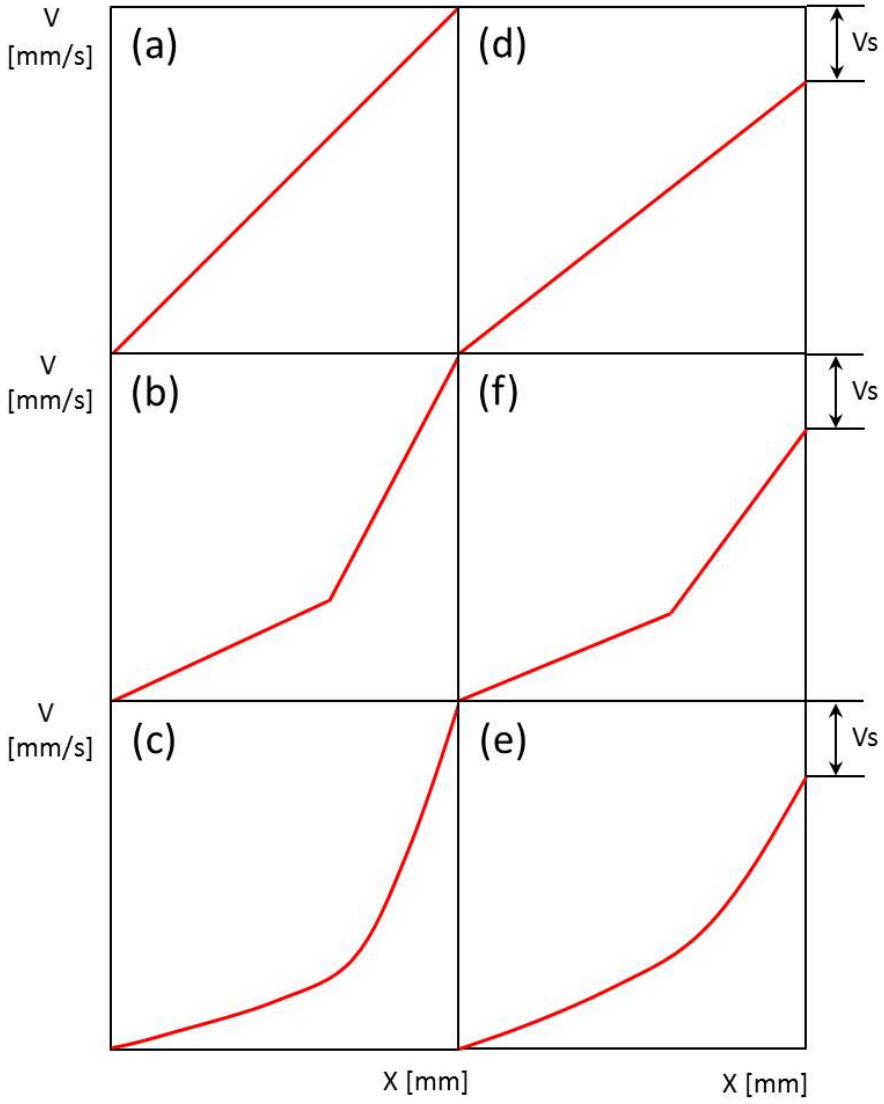

Figure 2.3: (a) linear velocity profiles, (b) shear banded profiles with sharp interface, (c) curved velocity profiles with broad interface, and (d-e) corresponding velocity profiles with wall slip. Vs is slip velocity.

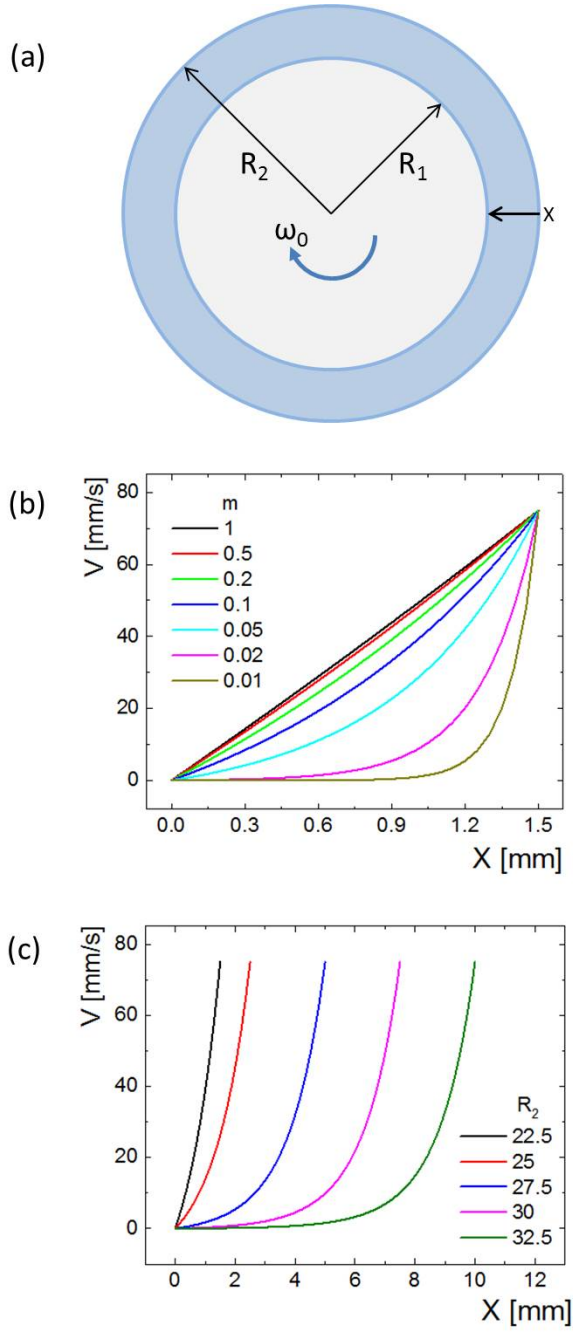

Figure 2.4: (a) Schematics showing the geometry of the shear cell, ω_0 is the applied angular velocity. R_1 and R_2 are the radii of the inner and outer cylinder. (b) Calculated velocity profiles depending on different shear thinning factor m for a shear rate of 50 s^{-1} using eq. 2.8 with fixed Radii of $R_1 = 22.5\ mm$ and $R_2 = 24\ mm$, which is the same as the shear cell we use. (c) Calculated velocity profiles depending on different R_2 for a shear rate of 50 s^{-1} using eq. 2.8 with fixed m of 0.1.

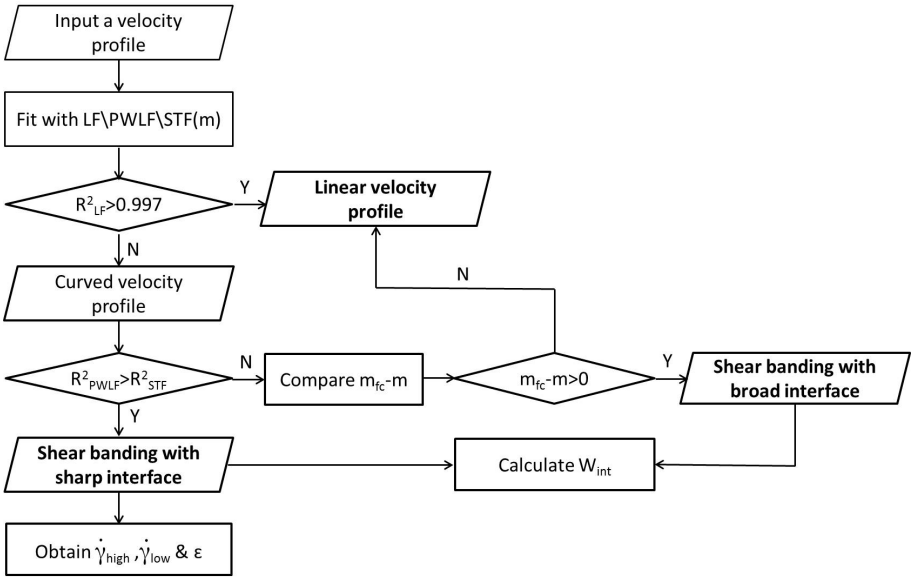

Figure 2.5: Logic flowchart for velocity profile analysis

as shown in Fig 2.3d-e, in which cases the apparent velocity V_1 close to wall of the rotational outer cylinder is lower than the applied velocity V_0. In these cases, the slip velocity can be calculated using:

$$V_s = V_0 - V_1. \tag{2.3}$$

In case of wall slip, the effective velocity V_1 is used to analyze shear banding in order to correct for the effect of wall slip on shear banding.

The situation for a shear thinning fluid that can be described by,

$$\sigma \sim \dot{\gamma}^{m_{fc}}, \tag{2.4}$$

where m_{fc} is the shear thinning factor as obtained from the flow curve. For such a fluid, the velocity profile in the Couette geometry can be calculated. For a geometry like Fig. 2.4a with a bob length of L, the torque at position x in the sample should be the same as near the inner cylinder at $R_2 - R_1$, so we have,

$$T = \sigma_{R_2-R_1} * 2\pi R_1^2 L = \sigma_x * 2\pi (R_2 - x)^2) L. \tag{2.5}$$

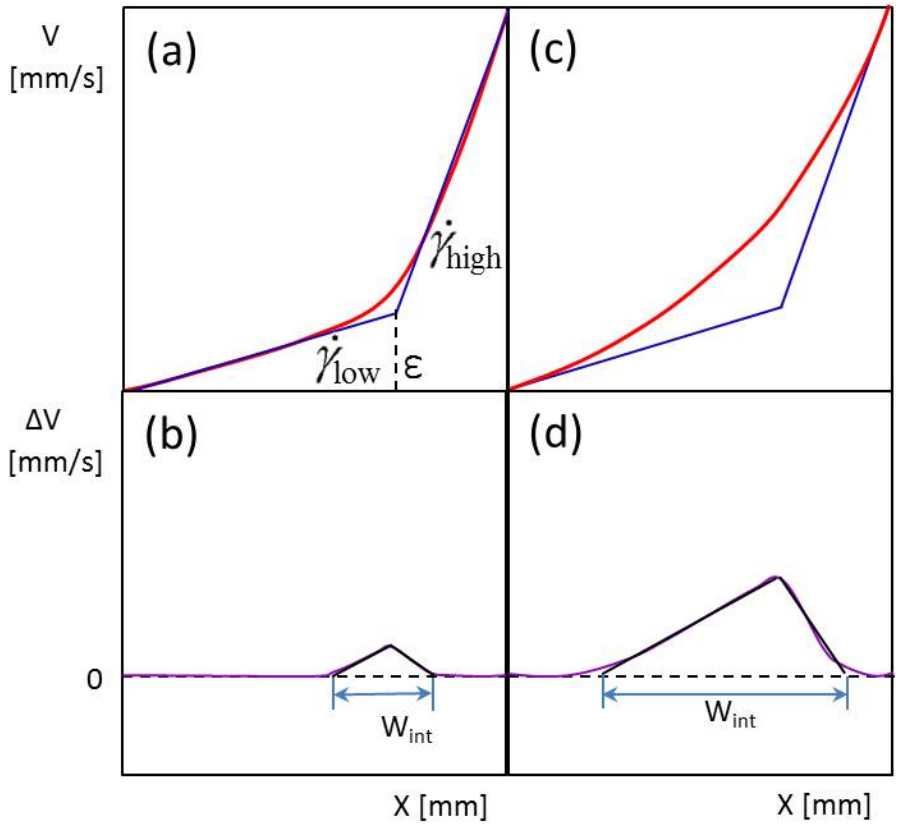

Figure 2.6: Interface width determination of a classic banded velocity profile(a) and a curved velocity profile(c):for a shear banded veloctity profile the slopes of PWLF fit are defined by true high and low shear rate in the bands $\dot{\gamma}_{low}$ and the $\dot{\gamma}_{high}$ while the slops for the PWLF fit of a curved velocity profile are shear rates calculated from the shear thinning function near the wall. The corresponding residues of the PWLF fits from the velocity profile are given in (b) and (d) and the interface width is determined by fitting the residue from the crossover linearly toward the x axis.

Thus, the stress at position x can be calculated by the following equation,

$$\sigma_x = C_1 R_1^2/(R_2 - x)^2 = C_2 \dot{\gamma}_x^m. \tag{2.6}$$

Where, C_1 and C_2 are constants. The shear rate at position x is given by

$$\dot{\gamma}_x = C[R_1/(R_2 - x)]^{2/m}, \tag{2.7}$$

where C is constant. By integrating equation 2.7 with no-slip boundary condition (i.e. $V(0) = 0$ and $V(R_2 - R_1) = \omega_0 R_1$), we obtain the shear thinning function(STF) [19],

$$V(x) \ = \ \omega_0 R_1[(R_2 - x)^{1-2/m} - R_2^{1-2/m}]/[R_1^{1-2/m} - R_2^{1-2/m}]. \tag{2.8}$$

Fig. 2.4b and c show the velocity profiles for $50s^{-1}$ with varying shear thinning parameter m and R_2 calculated by the shear thinning function 2.8. As can be seen in Fig. 2.4b, when the shear thinning factor $m = 1$, the velocity is linear, which is the case for Newtonian fluids. If there is shear thinning in the system, as is the case in the experiments we will show later, the velocity profile will be curved in a Couette shear cell. The more shear thinning the system is, the more curved the velocity profile will be. The curvature of the velocity profile is also related to the ratio of R_1/R_2 for a shear thinning fluids. With the same shear thinning parameter m, the velocity profile becomes increasingly curved as well with increasing R_2, given R_1 is fixed, see Fig.2.4c. However, shear thinning should not be confused with classic shear banding, where sharp interface between the two bands would be expected. The interface is still smooth even when extreme shear thinning occurs, see the smooth interface at $m = 0.01$(Fig. 2.4b) or extremely large gap is used, $R_2 = 32.5\ mm$(Fig. 2.4c) for example. Curved velocity profiles like those in Fig. 2.3c and e can be well fitted with the shear thinning function Eq. 2.8 with varying m, which indicates the curvature of the velocity profile. The difference between this fitting parameter and the shear thinning factor derived from the flow curve, $m_{fc} - m$, is an indication of shear banding in the system: in case there is no shear banding in the system, the velocity profile in a Couette shear cell should be as curved as predicted by the shear thinning factor from rheological measurements, and thus $m_{fc} - m$ should be zero.

To classify the velocity profiles we follow the following procedures shown in Fig. 2.5. First, we fit a given velocity profile with the linear function(LF), shear thinning function(STF) and a piecewise linear function (PWLF), and the resultant R^2s of those fits are compared. R^2 is a a statistical measure of

how close the data are to the fitted regression line. If the R^2 of the LF is the highest, it is taken as a linear velocity profile. Otherwise, the R^2 of the PWLF and STF are compared. If the R^2 of the PWLF is higher than that of the STF, we can unambiguously classify the profile as a shear banding velocity profile, for which the true shear rate in the high and low shear rate band $\dot{\gamma}_h$, $\dot{\gamma}_l$ and the fraction of the high shear rate band ϵ are obtained. If R^2 of the STF is higher that of the PWLF, then the fitting parameter m of the STF is compared the shear thinning factor m_{fc} as obtained from the flow curve. If m equals to m_{fc}, i.e.$m_{fc} - m \approx 0$, the nonlinear velocity profile should still be linear. It appears to be curved due to the stress gradient in the Couette shear cell rather than due to shear banding instability. If m_{fc} is higher than m, the velocity profile should be shear banded velocity profile, however, with broad interface.

To obtain the interface width W_{int} for a shear banded velocity profile with sharp interface, as shown in Fig 2.6a, we fit the data points with a PWLF starting from both walls. These slopes of the linear functions can be assigned as the true high and low shear rate bands, while the fraction ϵ of the high shear rate band which is defined by the following equation is also defined by the crossover of the PWLF fit.

$$\epsilon = \frac{\dot{\gamma}_{app} - \dot{\gamma}_l}{\dot{\gamma}_h - \dot{\gamma}_l} \, . \tag{2.9}$$

The interface width W_{int} is calculated from the residual of the fit, see Fig 2.6b.

For a shear banded velocity profile with broad interface, there are not enough data points for the linear fits from the walls. The slopes of the linear functions are calculated from the shear thinning function directly since it can fit the velocity profile very well, and the the interface width is determined the same ways as for the shear banded velocity profile with sharp interface. As we will show later in chapter 3-5 that the velocity profiles with sharp interface as determined by comparing the R^2 show W_{int} lower than half of gap distance $d/2$.

2.4 Summary

We introduce in this chapter our experimental set-up to measure velocity profiles, as well as our approach to analyzing these profiles. Here we take into account that there will always be curvature in the velocity profile when the sample

is shear thinning, given the curvature of the geometry. Hence we developed an analysis method that can be used to distinguish between nonlinear curved profiles due to shear thinning and actual shear banding. To this end, we introduce new definition of the interface width W_{int}, which we will use in the following chapters.

Chapter 3

Shear-banding in Entangled Xanthan Solutions: Tunable Transition from Sharp to Broad Shear-band Interfaces

3.1 Introduction

As mentioned in Chapter 1, whether shear-banding is a generic phenomenon for the more common case of entangled polymeric systems is still under debate. Moreover, no clear shear-banded velocity profiles are observed in many of the experiments where shear-banding is claimed, but rather highly curved profiles. Such curved velocity profiles can also occur, however, when shear-banding is absent, for example due to the stress gradient in a Couette cell in combination with a strong shear thinning fluid, as discussed in Chapter 2.

The aim of the present chapter is to clarify if entangled polymeric systems can exhibit the classic shear-banding instability that corresponds with strong shear thinning, without necessarily giving rise to a clear shear-banded state but rather to a highly curved velocity profile. For our study we use xanthan, a highly charged poly-saccharide, as a shear-thinning polymer. The beauty of this system is that its rheology is highly tunable [82, 83, 84, 85, 86, 87], especially by changing the ionic strength. For this reason, xanthan is used in abundance as a food additive and rheology modifier in food industry [88],

so that it is also of practical importance to understand the flow behavior of xanthan solutions. The effect of ionic strength on shear-band formation has already been identified for entangled DNA solutions, suggesting that electrostatic repulsion facilitates shear-induced alignment and in this way enhances shear-banding [80]. Such local interactions and molecular features can possibly be related to shear banding via the convective-constraint-release theory[89] as first introduced in Ref.[90]. The theory accounts for both diffusion of polymer chains through a confining tube as well as flow-induced convection of the tube, leading to a non-monotonous constitutive equation [7, 91]. Alternatively, the shear-banding mechanism for entangled polymers has been interpreted as force imbalance between intermolecular griping force and elastic retraction force[92]. We conjecture that the local interactions change dramatically for xanthan as the electrostatic repulsion as well as the stiffness of xanthan changes with ionic strength (the persistence length varies from 417 nm in pure water to 150 nm in $0.1 - 0.5\ M\ KCl$ [79]) .

Indeed, we will unambiguously identify shear-banding at very low ionic strength, at a high concentration and in a range of relatively low applied shear rates, as in this region the observed stationary velocity profiles consist of two spatially extended regions (the "bands"), within which the shear rate is essentially independent of position, and which are separated by a relatively sharp interface. An unexpected increase of the width of the interface, for which we will give a new definition, is observed when moving away from this region in parameter space. We find highly curved velocity profiles when the extent of the interface is comparable or larger than the cell gap width, despite the fact that the system exhibits the classic shear-banding instability (for which $d\sigma_{hom}/d\dot{\gamma} < 0$). To avoid confusion, we shall refer to a stationary velocity profile as a SBI-state (where "SBI" stands for "Shear-Banding Instability"), when the system, for the applied shear rate, exhibits the classic shear-banding instability. A SBI-state can thus be a shear-banded state, in the sense that there are two clear bands within which the shear rate is constant, separated by a sharp interface, or it can be a highly curved profile with broad interfaces comparable or larger than the gap width. The question raised above is thus whether the observed highly curved velocity profiles correspond to SBI-states.

This chapter is organized as follows. Section 3.2 contains details on the materials and methods used in this study. Section 3.3.1 presents the rheology of samples with different xanthan and salt concentrations. The velocity profiles for these samples, the analysis of the velocity profiles and the resulting identification of shear-banding are discussed in section 3.3.2. In section 3.3.3 the results of birefringence measurements are presented. A discussion and summary are given in section 3.4 and section 3.5, respectively.

3.2 Materials and Methods

Xanthan powder was purchased from Sigma and used without further purification. The powder was pre-dissolved in Milli-Q water and mixed for 30 min at room temperature. The resultant solution was then heated to 95 ^oC, kept at that temperature for one hour, and subsequently cooled down to room temperature gradually. The overlap concentration of the xanthan in water is about 0.08wt%, see Fig. 3.1. We prepared aqueous xanthan solutions with concentrations of 0.3($3.75c^*$), 0.5($6.25c^*$), and 0.7 $wt\%$($8.75c^*$). Note that 0.7wt% is the highest concentration that can be reached before turbidity becomes a problem. For the 0.7 $wt\%$ sample we added NaCl to a final ionic strength of 5 mM, 10 mM and 1 M, which tunes the flexibility of the polymer backbone as well as the electro-static repulsion between the polymers. The system is not a perfect model system, in the sense that it is polydisperse and can be branched to an unknown extent due to pair mismatch (the degree of branching might aid shear-band formation, as was shown for star polymers[93, 94]).

Rheological measurements were carried out using an ARES rheometer (Rheometric Scientific Inc., NJ) operating at 20 ^oC and using a cone-plate geometry, with a cone angle of 0.04 rad, diameter of 25 mm and a gap distance of 0.046 mm. To prevent water evaporation during rheological measurements, the meniscus of the aqueous xanthan solution in the cone-plate cell was surrounded by anti-evaporation silicone oil (Ibidi).

Flow velocity profiles were obtained at 20 ^oC with the HDLS setup described in Chapter 2. In order to gain structural information of the sample during shear, we probed the alignment using birefringence measurements. To this end, we directed a separate laser beam along the gradient direction of the Couette cell, which was placed between two crossed polarizers that were rotated 45^o with respect to the flow direction. We monitored the transmitted intensity by means of a diode, thus probing orientation in the flow-vorticity plane. Moreover, images of the sample during steady shear were taken between same crossed sheet polarizers using a white light box in order to probe the birefringent structure, as described in Chapter 2.

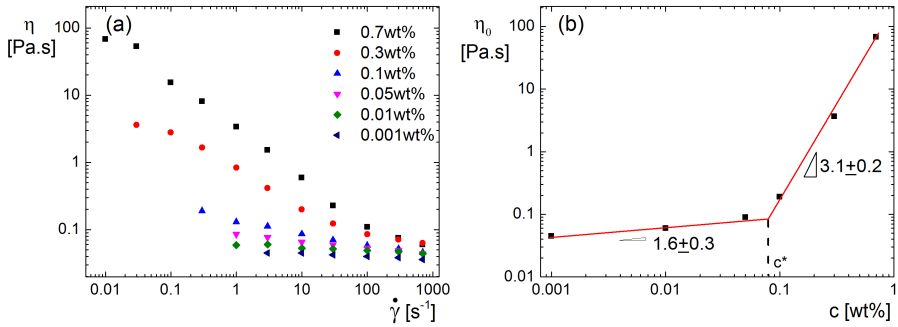

Figure 3.1: The viscosity vs. shear rate (a) and zero shear viscosity vs. concentration (b) for xanthan in water at 20 ^oC. The numbers in (b) show the slopes of zero viscosity dependence on concentration in different concentration regimes.

3.3 Results

3.3.1 Rheology

Determination of the Overlap Concentration c^* of Xanthan

To determine the overlap concentration of the xanthan used in this work, we measured the shear rate dependence of the viscosity for a concentration series of xanthan in water(Fig. 3.1a). The zero viscosity for each concentration is obtained and plotted against concentration (Fig. 3.1b). Two regimes can be observed, namely $c \sim \eta^{1.6}$ at low concentration and $c \sim \eta^{3.1}$ at high concentration. The power law exponents are consistent with what reported for polysaccharide as in Ref. [95]. The c^* is found to be around $0.08wt\%$. Hence, we performed most of our experiments at approximately 10 c^*, which locates in the entangled regime.

Step-rate Tests

We determine the viscosity of each point in the flow curve by performing step rate tests. Fig. 3.2 displays these tests for all used ionic strengths and selected shear rates. The viscosity is always determined from the plateau after the overshoot. Moreover, the heterodyne measurements were always carried out after the system get steady state as indicated here.

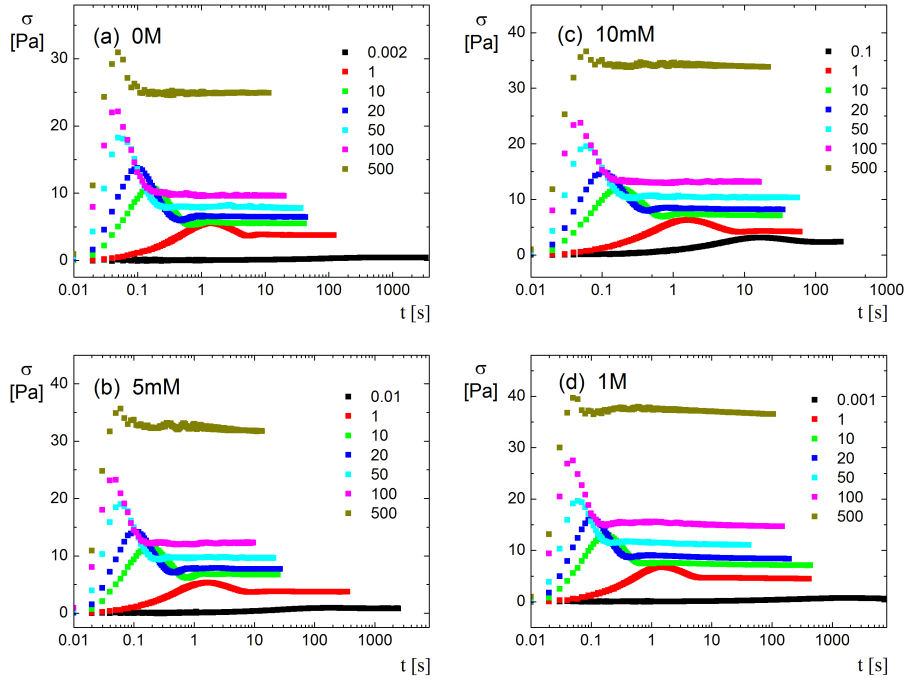

Figure 3.2: The stress development in startup shear flow for 0 M(a), 5 mM(b), 10 mM(c) and 1 M(d) added salt concentration for 0.7 wt% xanthan

Frequency Sweep and Flow Curve

Figure 3.3 shows the storage G' and loss modulus G'' as well as the shear-rate dependence of the stress in the stationary state of xanthan solutions at different concentrations and ionic strengths. For the samples without salt, both the storage G' and loss modulus G'' increase with concentration, while the crossover frequency decreases dramatically, as can be seen in Fig. 3.3a. The corresponding much slower chain dynamics at higher concentrations is attributed to an increasing degree of entanglement. The flow curve (the stress as a function of the applied shear rate) is similarly sensitive to the xanthan concentration, going from a weak shear-thinning flow curve at 0.3 $wt\%$ xanthan to a strongly shear-thinning flow curve with a sloped stress plateau at 0.7 $wt\%$ xanthan, as seen in Fig. 3.3b.

The rheological properties are much less sensitive to the ionic strength, as can be seen from Figs. 3.3c,d, for the 0.7 $wt\%$ sample. There is a slight shift of the

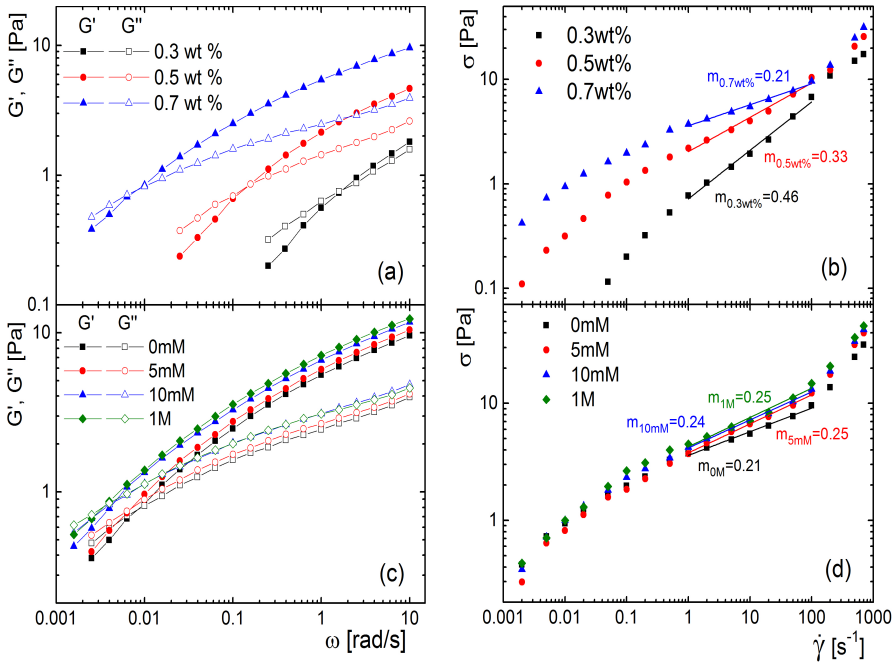

Figure 3.3: (a) The storage G' and loss modulus G'' and (b) the stress σ in the stationary state as a function of the shear rate $\dot{\gamma}$, for various xanthan concentrations without added salt. (c) is the same as in (a), and (d) the same as in (b), but now for various salt concentrations at a fixed xanthan concentration of $0.7\,wt\%$. The lines in (b) and (d) are linear fits to the experimental data, which indicate the sloped stress plateaus, with an indication of the shear-thinning exponent m_{fc} , which is defined as $\sigma \sim \dot{\gamma}^{m_{fc}}$. Note that the fitting range is from 1 to $100 s^{-1}$.

crossover frequency to smaller frequencies with increasing salt concentration. This is attributed to an increasing xanthan-chain flexibility as the Debye length decreases, leading to a slight increased degree of entanglement. The flow curves shown in Fig. 3.3d are equally similar for each of the salt concentrations. There is a sloped plateau for all salt concentrations within the shear-rate range of about $1 - 100\,s^{-1}$, where the stress σ varies with the shear rate $\dot{\gamma}$ as $\sigma \sim \dot{\gamma}^{m_{fc}}$, with the exponent $m_{fc} \approx 0.2$ (the index "fc" stands for "flow curve"), indicative for strong shear-thinning.

As can be seen from Fig. 3.4, we obtain a master curve for G' and G'' by rescaling the frequency. This implies that the dynamics of the various xanthan solutions underlie the same mechanisms, independent of the xanthan concentration and

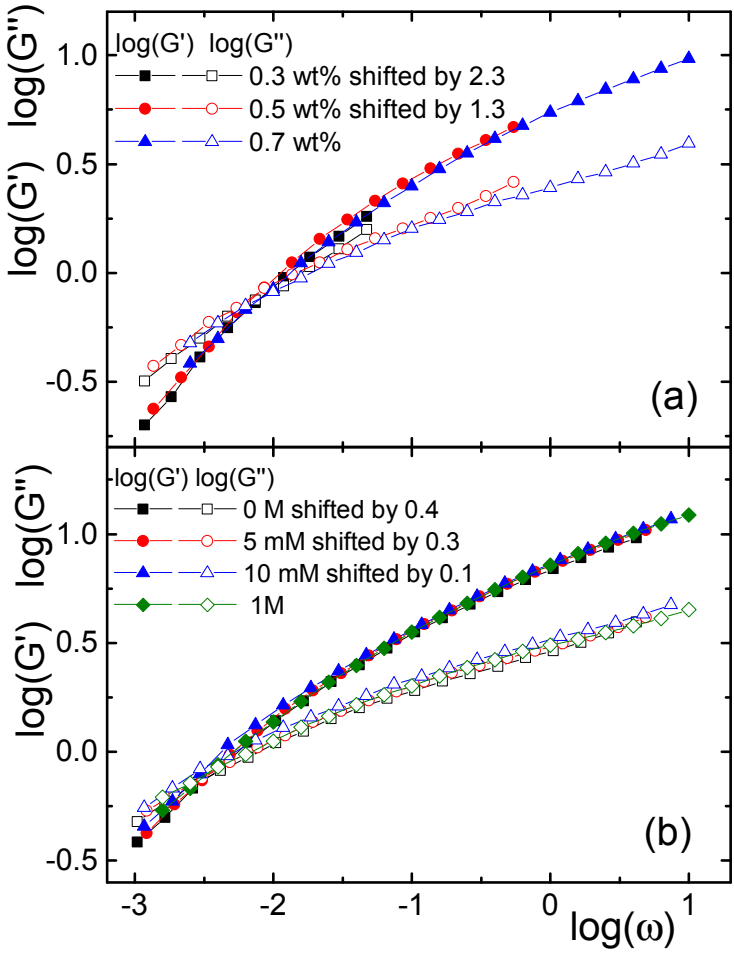

Figure 3.4: Master curves for the storage G' and loss modulus G'' by (a) time-concentration and (b) time-ionic strength superposition. The shifts of the logarithmic frequency scale are indicated in the figures.

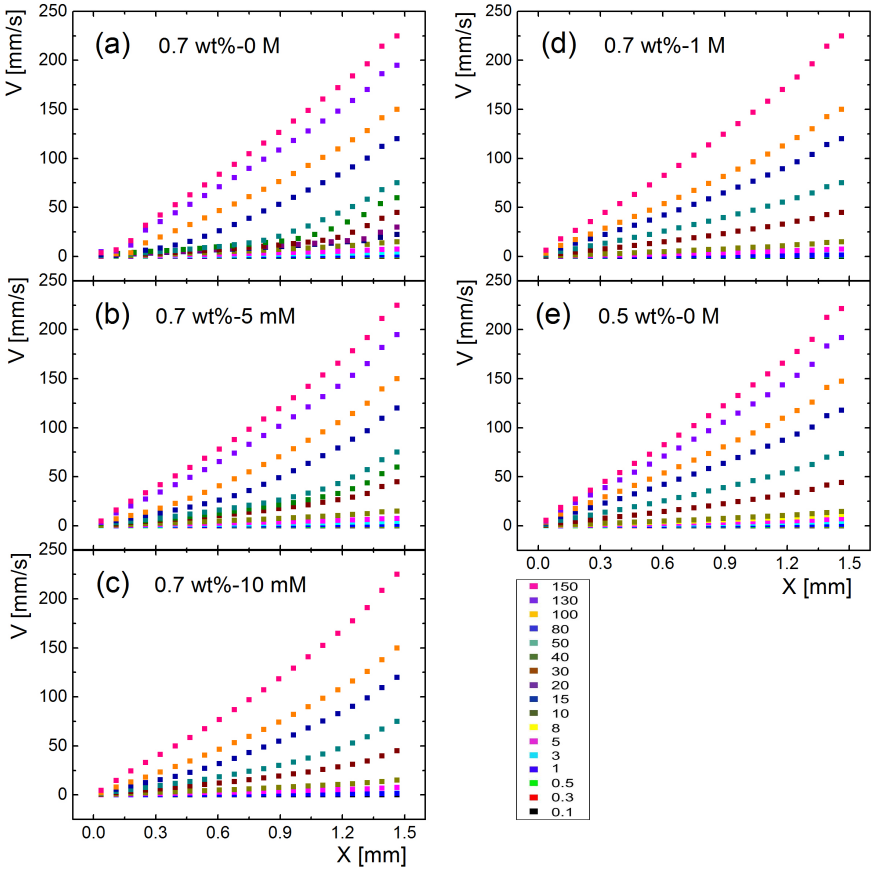

Figure 3.5: Velocity profiles at different shear rates at various xanthan concentrations and added salt concentrations, as indicated. The color bar indicates the applied shear rate in s^{-1}.

the salt concentration. There is no change in the principle processes that set the dynamics of these systems on changing either the xanthan or the salt concentration. The degree of entanglement changes with xanthan and salt concentration, but the entanglement-relaxation mechanisms remain the same. It also indicates that xanthan is not prone to gel due to specific attractive interactions that would frustrate such a scaling. Thus, the effects that we will observe by tuning the ionic strength will be either caused by the effect of flexibility or repulsion.

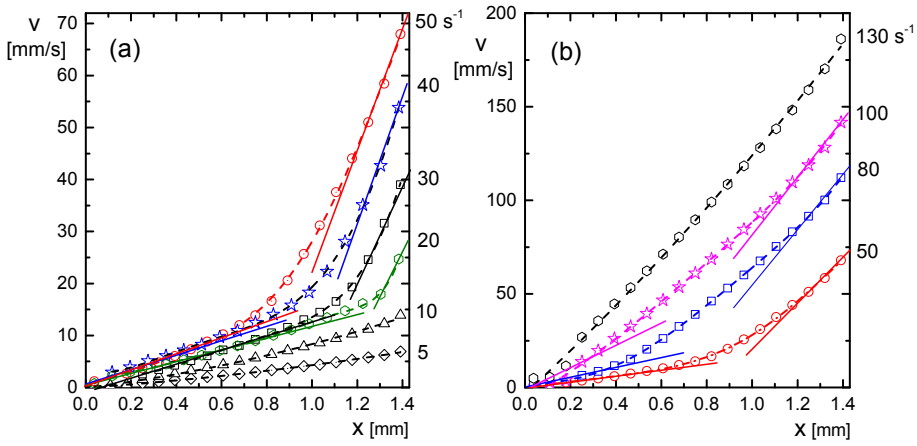

Figure 3.6: The suspension velocity as a function of the position in the gap of the Couette cell, for the $0.7\,wt\%$ sample with no added salt. (a) Velocity profiles for applied shear rates up to $50\,s^{-1}$, and (b) from 50 up to $130\,s^{-1}$. The numbers on the right axis indicate the applied shear rate. The dashed curves through the data points are guides-to-the-eye, while the straight lines correspond to the linear profiles near the walls of the shear cell.

3.3.2 Velocity Profiles

Velocity Profiles: Data

The sloped stress plateaus observed in the flow curves in Fig. 3.3d for the $0.7\,wt\%$ samples hints to the possibility of shear-banding resulting from strong shear-thinning. This is indeed observed in the velocity profiles shown in Fig. 3.5. The velocity profiles for $0.7wt\%$ xanthan with $0M$ added salt indeed display two distinct slopes with a sharp interface in a shear rate region between 15-50 s^{-1}, see Fig. 3.5a. These features become less pronounced at higher added salt concentrations (Fig. 3.5b-d) or at lower xanthan concentrations (Fig. 3.5e). Selected velocity profiles for 0.7wt% xanthan with 0 M added salt are shown in Fig 3.6. Zooming into the region of applied shear rates of 5-50 s^{-1}, we see that velocity profiles are linear below $10s^{-1}$, become sharply banded above $15\,s^{-1}$, and turn linear again above $100s^{-1}$, see Fig. 3.6a and b. Note that there is no sign of wall slip for all the samples investigated, since the velocity near the inner moving wall reaches the applied velocity and zero near the outer standing wall.

The shear rates of 15-50 s^{-1} are located approximately in the shear rate region

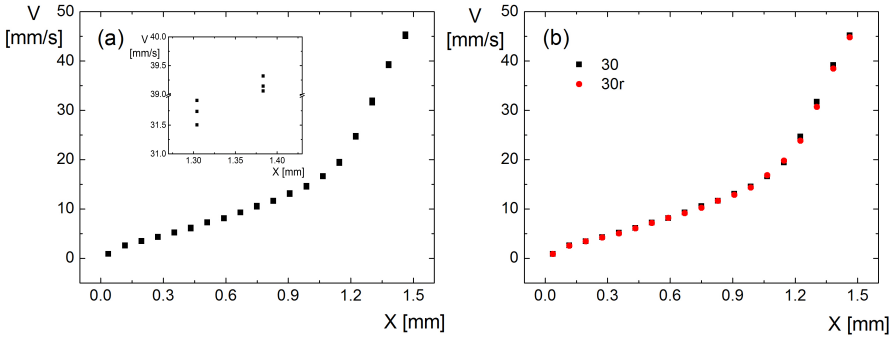

Figure 3.7: Reproducibility of velocity profiles: (a) 3 data points are taken at each position with an interval of 3 seconds per point. The insert shows the magnification of the 3 data points. (b) a comparison between two repeated measurements taken at an interval of 30 minutes. Velocity profile were taken at $30s^{-1}$ for $0.7wt\%$ xanthan with no added salt.

where the slope in the flow curve is lowest, see Fig. 3.3d. This is an indication that the banded velocity profiles in Fig. 3.6 are related to the classic shear-banding instability, being due to strong shear-thinning. However, most velocity profiles are not the same as in classic shear banding where sharp interface would be expected. Instead, round interfaces with considerable widths between the two bands are observed. We will show later how we quantify this transition from shear banding with sharp interfaces to smooth curved interfaces, by defining the width of the interface W_{int}.

Velocity Profiles: Stability

As discussed in the Chapter 2, there are three timescales at which the stability of the flow can be probed. As one can see in Fig. 3.7a, the three data points overlap nicely and we find that the error bar of the velocity is within 5%. The whole velocity profile is stable in a larger timescale as well, as is shown in Fig. 3.7b. In order to test the stability of the velocity profiles on a smaller timescale. The correlation functions of typical velocity profiles at different shear rates and salt concentrations at three different positions in the gap are presented in Fig. 3.8 and Fig. 3.9. The general trend can be observed is that the minima in the correlation functions display an upturn exactly in the region where the interface width is sharpest. The minimum in the oscillations of the correlation functions become level when moving away from this region. This suggests that in the latter case single frequencies are measured, so that therefore a single velocity

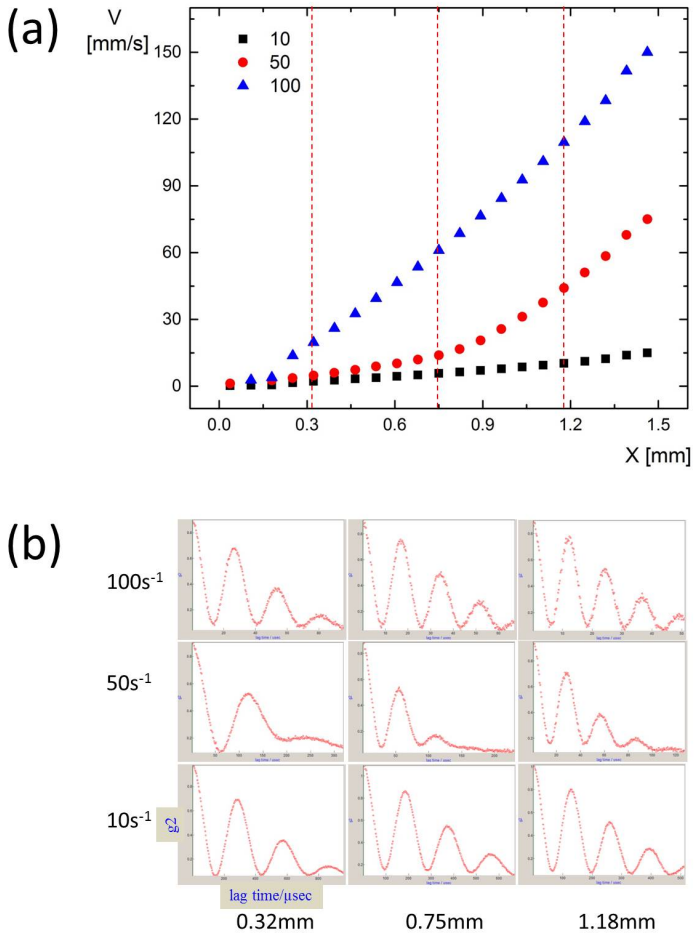

Figure 3.8: (a) Typical velocity profiles for the $0.7wt\%$ xanthan with no added salt. The numbers indicates the applied shear rate in s^{-1}. The vertical dash lines indicated the position where the correlation functions are shown. (b) Correlation functions at varying positions from the stationary outer cylinder shown on the bottom for different shear rates which are indicated on the left.

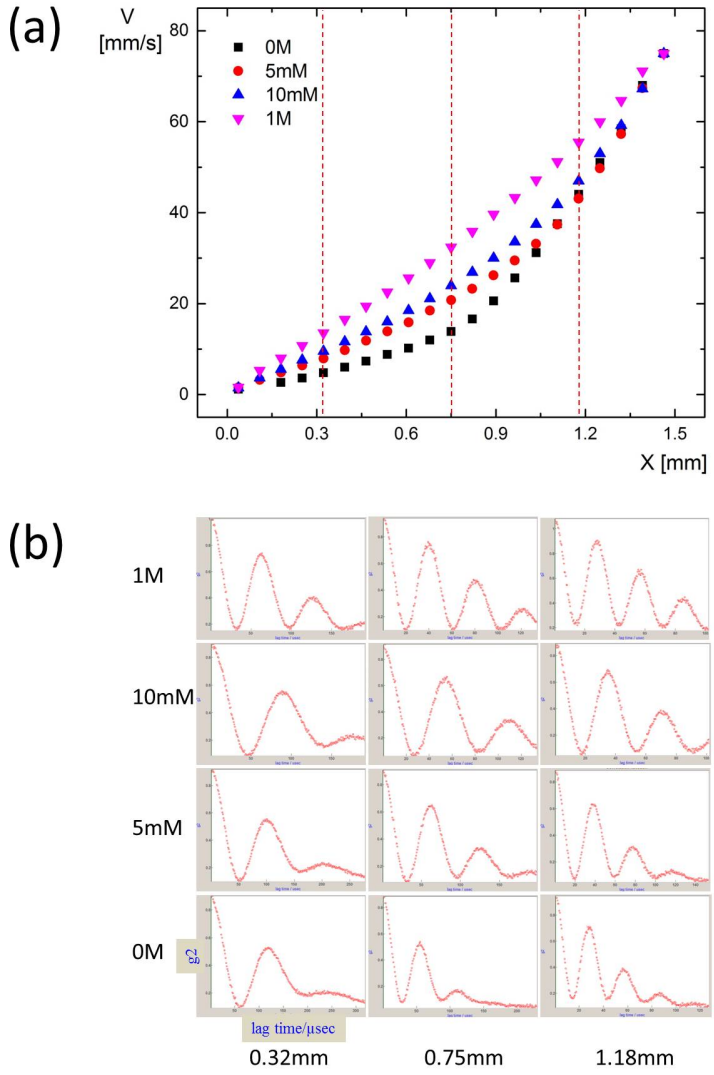

Figure 3.9: (a) Typical velocity profiles at $50s^{-1}$ for varying added salt concentration for $0.7wt\%$ xanthan. The vertical dash lines indicated the position where the correlation functions are shown. (b) Correlation functions at varying positions from the stationary outer cylinder shown on the bottom for different salt concentrations which are indicated on the left.

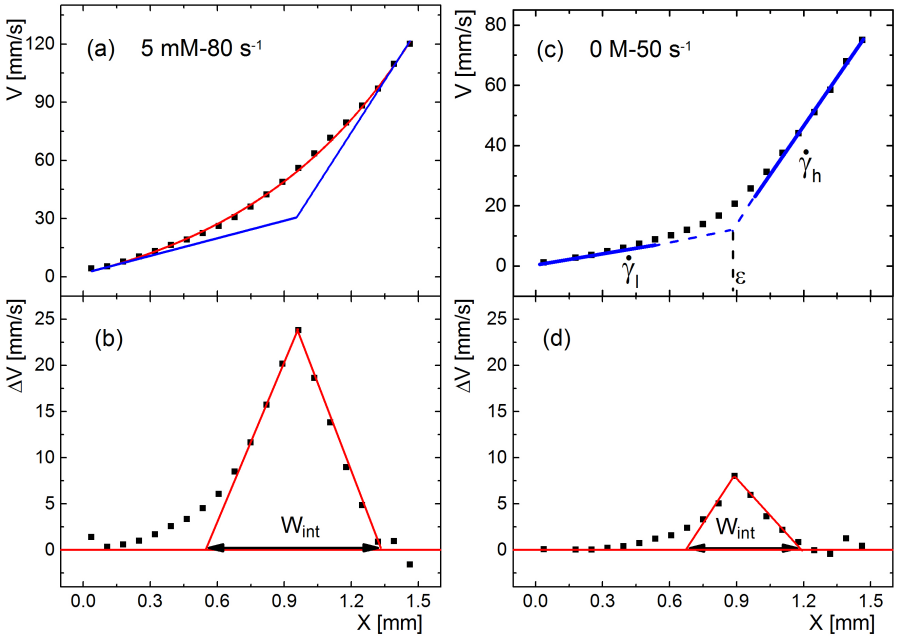

Figure 3.10: The determination of interface width W_{int} for the $0.7\,wt\%$ xanthan concentration, for two velocity profiles. (a) A broad interface with the shear-thinning function fit given by the red curve. The blue lines are linear curves with a slope equal to that of the slope of the shear-thinning function at the walls of the shear cell. Panel (b) illustrates the determination of the width W_{int} of the interface from the residual ΔV. (c) For a relatively sharp interface, the corresponding linear curves in blue are determined directly from the data points near the wall of the cell. The slopes of the linear curves are taken as the high shear rate $\dot{\gamma}_h$ and low shear rate $\dot{\gamma}_l$, respectively. The fraction of high shear rate band ϵ is thus defined by the crossover of the two linear curves. The same procedure is used to determine the interface width, as plotted in (d).

is probed over a time of three seconds. In the presence of sharp shear bands there is mixing of other frequencies, resulting in the upturn of the minimum. This means that the widening of the interface is not due to fluctuations in the velocity, as these are mostly present exactly when there are sharp shear bands. The upturn of the minimum is more pronounced closer to the walls, which suggests that the fluctuations might be related to a competition between wall slip and shear banding, see for example Ref. [67, 96].

Velocity Profiles: Analysis

In order to quantify these observations, we apply three functions to fit the velocity profiles. For Newtonian fluids a linear function suffices to fit (L fit). If there is no slip then the function is uniquely defined by the slope, which is then equal to the applied shear rate $\dot{\gamma}_{app}$.

Curved flow profiles due to shear thinning fluids are fitted by the shear-thinning function (ST fit)[19],

$$V(x) \;=\; \omega_0 R_1[(R_2 - x)^{1-2/m} - R_2^{1-2/m}]/[R_1^{1-2/m} - R_2^{1-2/m}], \qquad (3.1)$$

where the shear thinning factor m is defined as $\sigma \sim \dot{\gamma}^m$, and x is the distance from the stationary outer cylinder with angular velocity ω_0, and R_1 and R_2 are the radii of the inner and outer cylinder, respectively. As shown in Ref.[19], Eq. 3.1 describes the exact flow profile in a Couette Geometry when the stress scales like $\sigma \sim \dot{\gamma}^m$ for all shear rates attained for the profile at hand. Compared to the linear fit, this function has m as an extra fit parameter which can be as well obtained from the flow curve, see Fig. 3.3. In case of relatively sharp interfaces (like those in Fig. 3.6a), Eq. 3.1 cannot describe the flow profile.

In such cases the fluid display classic shear banding, the profile is best fitted by two straight lines with slopes $\dot{\gamma}_h$ and $\dot{\gamma}_l$, which are the shear rates in the low and high shear-rate band respectively. This is the piecewise linear function (PWL fit). Compared to the linear profile there is again one extra fit parameter when the lever rule should hold. The lever rule predicts that the extent of the high shear-rate band varies linearly with the applied shear rate, in case the shear rates within the bands are insensitive to the applied shear rate. In the absence of slip, the velocity of the rotating inner cylinder is on the one hand equal to $\dot{\gamma}_{app}\, L$, with $\dot{\gamma}_{app}$ the applied shear rate and L the gap width, and is on the other hand equal to $\dot{\gamma}_l L_l + \dot{\gamma}_h L_h$, with L_h and L_l the extent of these bands. Since $L = L_h + L_l$, it follows that the fraction of the gap that is occupied with the high shear-rate band is equal to,

$$\epsilon \;\equiv\; \frac{L_h}{L} \;=\; \frac{\dot{\gamma}_{app} - \dot{\gamma}_l}{\dot{\gamma}_h - \dot{\gamma}_l}\,. \qquad (3.2)$$

The extent of the high shear-rate band vanishes at the lower boundary of the shear-rate region where banding occurs (where $\dot{\gamma}_{app} = \dot{\gamma}_l$), and is equal to the full gap width L at the upper boundary (where $\dot{\gamma}_{app} = \dot{\gamma}_h$).

We now determine which of these functions is best suited to fit the velocity profiles shown in Fig. 3.5. In most cases the ST fit fits the velocity profile best, although the value of m can strongly deviate from the value obtained from the

flow curve, m_{fc}. The PWLF fit is better in the region 15-50 s^{-1} for the 0 mM sample. Figs. 3.10a and c show examples where the profiles are best fitted with the ST fit and the PWLF fit, respectively.

The next step is to determine the interface width W_{int} and, if possible, the shear rate in both bands, $\dot{\gamma}_l$ and $\dot{\gamma}_h$ and the fraction of high shear rate band ϵ. When the ST fit gives the best fit, then we calculate the residual ΔV, taking the difference between the ST fit and a shear banding profile that we construct from the slopes of the ST fit at both walls, giving $\dot{\gamma}_l$ and $\dot{\gamma}_h$, which we extrapolate to ϵ, see Fig. 3.10a. When the PWL fit gives the best fit, we construct a shear banding profile from the slopes of the data near both walls, giving $\dot{\gamma}_l$ and $\dot{\gamma}_h$, extrapolating these lines till they cross, from which we obtain ϵ, see Fig. 3.10c. Then we calculate the residual taking the difference between the data points and this shear banding profile, which is more accurate than using the PWL fit, as a broader interface does not affect the values of $\dot{\gamma}_l$ and $\dot{\gamma}_h$ in this case. In both cases, W_{int} is defined as the distance between the two points obtained from the cross-over of linear fits of the residual, starting at ϵ and fitting data towards lower and higher gap positions, and the x-axis, see Fig. 3.10b and d.

Velocity Profiles: Results

The velocity profiles suggest a smooth transition from a SBI-state, as defined at the end of the introduction, to a Newtonian response when moving away from the region where sharp shear bands are observed, as the interface between the bands widens until it fulls the full gap. Indeed, with our definition of the interface width W_{int} we observe this trend, plotting W_{int} as a function of the applied shear rate, see Fig. 3.11. The smallest interface widths are found for the sample without added salt and at intermediate applied shear rates, which still span about 1/3 of the shear-cell gap. W_{int} widens with added salt or by moving away from this shear rate region.

The sloped stress plateaus found in Fig. 3.3d and the sharp interface identified above indicate that the non-linear flow profiles are due to strong shear thinning (the classic gradient-banding instability). This is further evidenced by construction of the lever rule. To this end, we first select the velocity profiles that we want to test. Noting that the slopes at the wall are at most equal to $\dot{\gamma}_h$ and $\dot{\gamma}_l$ and W_{int} is underestimated when the interface is too wide, we select those profiles for which the interface width is about half of the gap size($0.75\ mm$),or less, see the horizontal dashed line in Fig. 3.11. When the selected velocity profiles indeed correspond to classic SBI-states, they should obey the lever rule, as discussed above. We plot the fraction ϵ for the sample $0.7\,wt\%$ at zero added salt in the shear rate range of $15 - 50s^{-1}$, see Fig. 3.12.

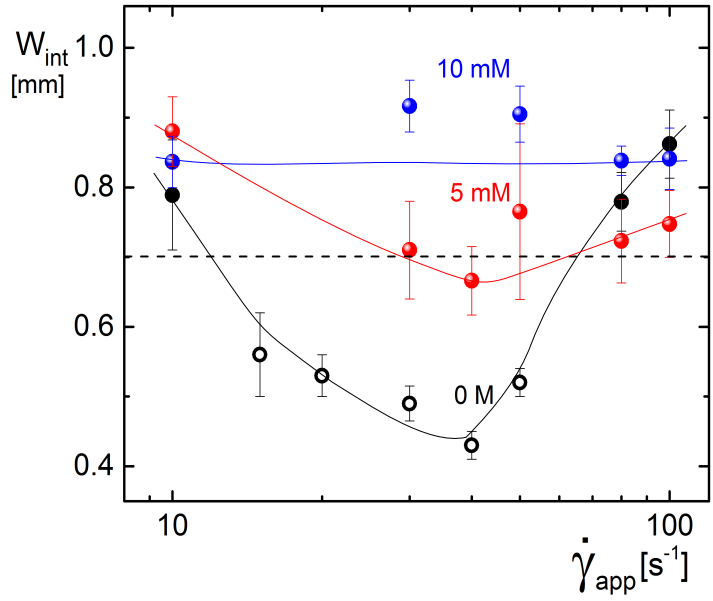

Figure 3.11: The width of the shear-band interface as a function of the applied shear rate, for the samples of 0.7 $wt\%$ xanthan without added salt and with 5 and 10 mM added salt. The open points are for sharp interfaces, the filled symbols for broad interfaces. The solid lines are guides-to-the-eye. Note that the gap width is 1.5 mm.

As can be seen from this figure, we recover the predicted linear dependence of ϵ on the applied shear rate, despite the slight shear rate dependence of $\dot{\gamma}_{l,h}$, see the inset in Fig. 3.12. Moreover, the shear-rate range where banding occurs on the basis of the lever-rule, is found to be $6 - 113\,s^{-1}$, as indicated by the vertical dashed lines in Fig. 3.12. This range corresponds quite well with the values found for $\dot{\gamma}_l$ and $\dot{\gamma}_h$ and is consistent with the shear-rate range where the sloped plateau in the flow curve in Fig. 3.3d is found. Interestingly, the ϵ values of two points at 5 mM salt that just have sharp enough interface to be included in the selection fall on top of the lever rule curve.

Since the lever rule cannot cease to be valid at shear rates only half-way the shear-banding region, we infer that the highly curved velocity profiles in Fig. 3.5 that dropped out of the selection still correspond to SBI-states, as defined at the end of the introduction, but with a very broad interface width. This includes 5 mM profiles, and potentially also 10 mM profiles.

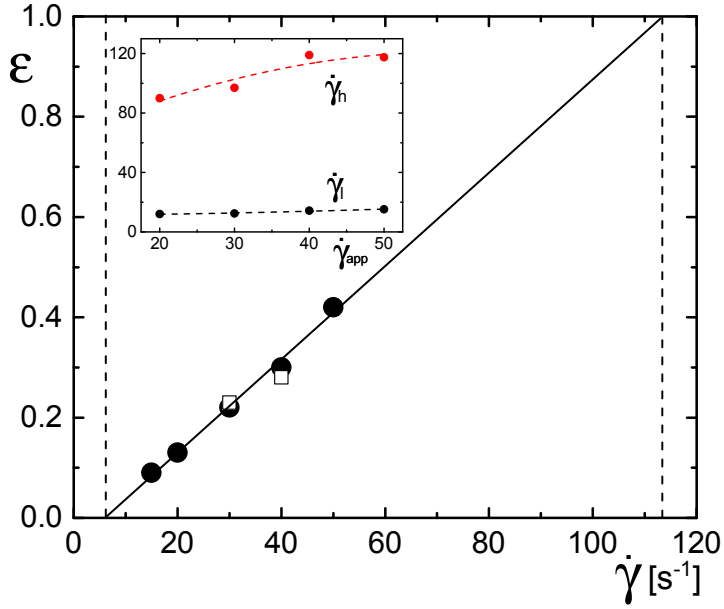

Figure 3.12: The lever-rule plot for $0.7\,wt\%$ xanthan without added salt (solid circles), and for the $5\,mM$ salt (open squares), where the fraction ϵ of the volume occupied by the high shear-rate band is plotted against the applied shear rate. The data points are based on the determination of ϵ from the velocity profiles with a sharp interface. The vertical dashed lines indicate the resulting range $6 - 113\,s^{-1}$ of applied shear rates where shear-banding occurs. The inset shows the shear rates in the high and low shear-rate bands as a function of the applied shear rates (in s^{-1}) for the system without added salt.

The more detailed analysis of the shear thinning parameter m given below confirms this conjecture. From the velocity profile depicted in Fig. 3.3d we see that the stress scales like $\sigma \sim \dot{\gamma}^{m_{fc}}$ with an exponent $m_{fc} \approx 0.20$ within the shear-rate range of about $1 - 100\,s^{-1}$. This value m_{fc} can be compared with the value of m obtained from fits of highly curved velocity profiles using the shear-thinning function (Eq. 3.1). When there is no shear-banding instability, m should be equal to m_{fc}. Thus, the difference $m_{fc} - m$, as plotted in Fig. 3.13, is indicative of the occurrence of a SBI-state (but only for applied shear rates where the scaling $\sigma \sim \dot{\gamma}^{m_{fc}}$ holds). This comparison is of course only possible when the velocity profile can be accurately fitted to the shear-thinning function, which turns out to be case, except for the profiles with a sharp interface for which the SBI-state is evident.

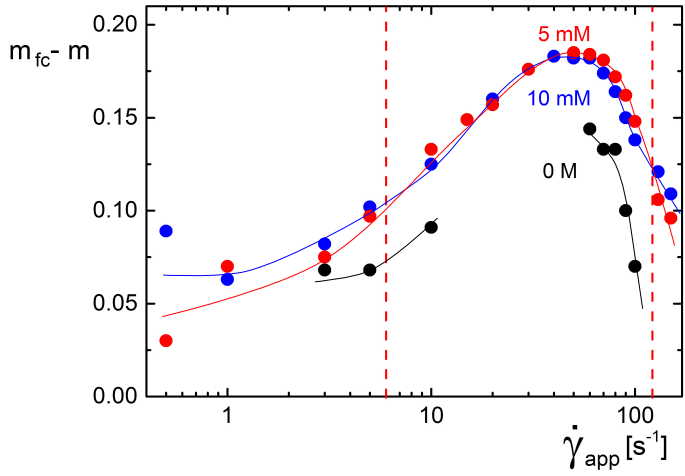

Figure 3.13: The difference of the exponents m_{fc} as determined from the flow curve and m as determined from the shear-thinning-function fit for $0.7\,wt\%$ xanthan, with $0\,M$, $5\,mM$ and $10\,mM$ added salt. The solid lines are guides-to-the-eye. The vertical dashed lines indicate the shear-banding region as obtained from the lever-rule plot. The gap in the data for the sample without salt is due to the fact that the interface is too sharp to be able to be well fitted with the shear-thinning function. Typical errors in the data points are ± 0.05.

The vertical dashed lines indicate the shear-banding region corresponding to SBI-states complying with the lever rule. As can be seen from this plot, there are significant differences between the two shear thinning factors within the shear-banding region. The difference $m_{fc} - m$ remains large beyond the shear-banding region at large applied shear rates, since for those shear rates the scaling $\sigma \sim \dot{\gamma}^{m_{fc}}$ does not hold, so that m is generally not equal to m_{fc} (the sloped plateau in the flow curve in Fig. 3.3d ends at about $100\,s^{-1}$). The above analysis strongly suggest that the $0.7\,wt\%$ xanthan solutions without salt and with 5 and 10 mM added salt exhibit the classic shear-banding instability, with very broad interfaces between the shear-bands at higher salt concentration. For the velocity profiles for the $0.7wt\%$ sample with 1 M added salt and $0.5wt\%$ with 0 M added salt sample, the difference between m_{fc} and m is of the order of the experimental error, suggesting that these are not SBI-states.

A diagram-of-states can be constructed, using the results presented in the current section. Three kinds of velocity profiles can be distinguished: (i) profiles for which $m \geq m_{fc}$, (ii) for which $m < m_{fc}$, and (iii) profiles with sufficiently sharp interfaces, for which $\dot{\gamma}_l$, $\dot{\gamma}_h$, and ϵ can be reliably determined. The

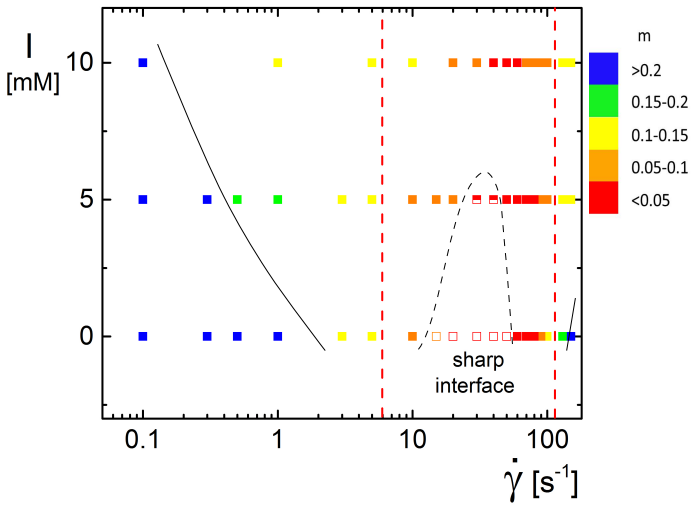

Figure 3.14: The diagram-of-states in the added-salt-concentration I versus the shear-rate plane, where velocity profiles are distinguished depending on the shear-thinning parameter m. The open points refer to banded profiles with a sharp interface. The black solid curves indicate m higher or lower than m_{fc}, which is about 0.2. The vertical dashed lines indicate the shear-banding region as obtained from the lever rule.

profiles (ii) include banded flows with broad interfaces. The state-diagram in Fig. 3.14 shows where these velocity profiles are found, depending on the salt concentration and the applied shear rate for the $0.7\,wt\%$ xanthan sample. The vertical red-dashed lines indicate the shear-banding region as obtained from the lever-rule experiments. The solid black lines indicate where the exponent m as obtained from the velocity profile becomes smaller than the shear thinning exponent m_{fc} as obtained from the flow curve. The minimum value of m occurs well within the banding region, and continuously increases away from the banding region. The dashed curve indicates the region where sharp interfaces are observed.

3.3.3 Birefringence Measurements

Birefringence experiments were employed to monitor whether shear-induced alignment and structural changes occur. Birefringence was measured between

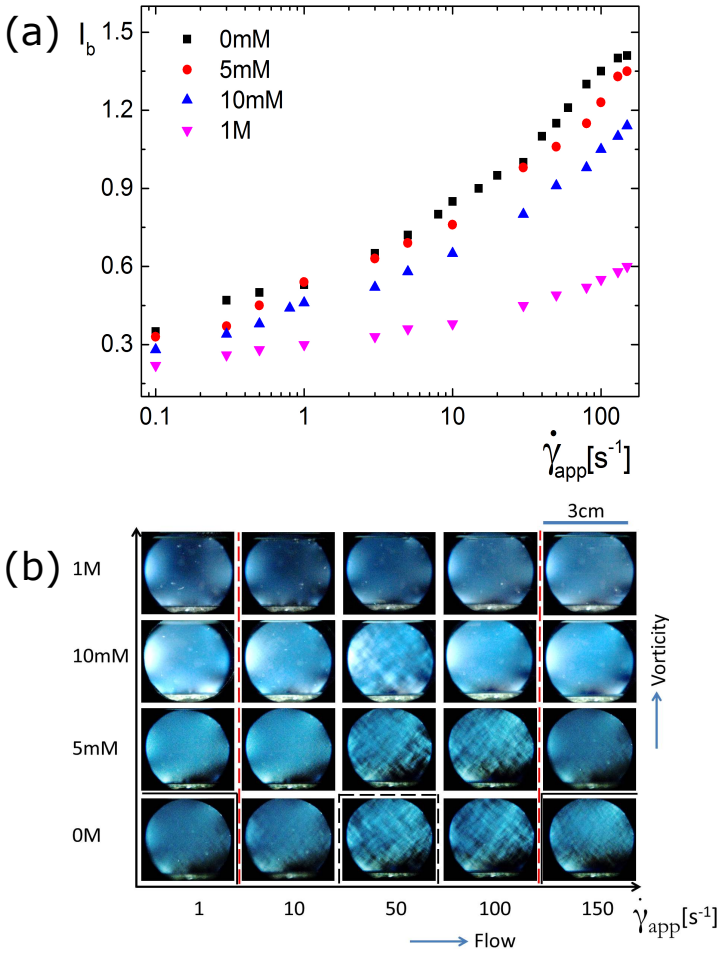

Figure 3.15: (a)The transmitted intensity I_b and (b) images taken between crossed polarizers at varying applied shear rate for 0.7 $wt\%$ xanthan solutions at different salt concentrations.The lines indicate the boundaries shown in Fig. 9. The flow and vorticity direction are indicated by the arrows and the scale bar is $3cm$.

crossed polarizers as a function of shear rate for the $0.7wt\%$ xanthan samples, probing orientation in the flow-vorticity plane. The observed birefringence increases with shear rate for each ionic strength, as can be seen from Fig. 3.15a. The birefringence for the shear-banding samples is significantly larger than for the non-banding system (with $1\,M$ added salt), indicating that significant structural changes occur for the systems that exhibit shear-banding. The larger birefringence intensity for the SBI systems is consistent with the crossed birefringent patterns shown in Fig. 3.15b, which are similar to what we observed in supramolecular polymer solution[42]. Exploring the nature of the structural changes requires a separate scattering/microscopy study, which is beyond the scope of present work.

3.4 Discussion

The question addressed in this work is whether entangled polymeric systems can exhibit the classic shear-banding instability that is connected to strong shear thinning, without necessarily giving rise to a clear shear-banded state but rather to a highly curved velocity profile. The common situation in other types of systems, such as surfactant wormlike micelles, is that the velocity profiles resulting from the classic shear-banding instability consist of two extended regions (the "bands") within which the shear rate is constant, separated by a sharp interface. We argue on the basis of experiments on xanthan solutions, that polymeric systems can exhibit the classic shear-banding instability, but the interface can be unusually broad, of the order of the gap width of the shear cell. The occurrence of very broad interfaces possibly justifies the claims in earlier work, where highly curved velocity profiles in various types of polymeric systems were interpreted as systems that exhibit the classic shear-banding instability[57, 59, 80].

We can make this claim because we observe a smooth transition between such stationary velocity profiles with sharp bands and curved profiles for concentrated xanthan solutions. The sharply banded flow is found for $0.7\,wt\%$ xanthan solutions at zero added salt in a range of relatively low applied shear rates, while the width of the interface increases when moving away from this region in parameter space until the extent of the interface is comparable or larger than the cell gap width and finally becomes linear. This effect has been reported earlier as a function of the ionic strength for wormlike micelles[97] and DNA [80], but it had not been quantified in terms of the widening of the interface. The claim that curved profiles can still be considered as shear-banded states, in the sense that they are the result of the classic shear-banding instability, is supported by two main observations. First, the lever-rule plot, as constructed from the

profiles with a sharp interface for the lowest ionic strength, is linear as it should. The extrapolation to determine the shear-rate range where banding occurs coincides with the extent of the sloped stress plateau in the flow curve for the sample without added salt, and it is also true the limited data for 5 mM added salt. Since the lever rule cannot cease to be valid at shear rates only half-way the shear-banding region, we conclude that the highly curved velocity profiles in Fig. 3.6b correspond to SBI-states with a broad interface, including the profiles at higher ionic strength. Second, we compared the shear thinning factors m and m_{fc}: the former describes the velocity profile in a Couette geometry, see Eq. 3.1, for a stable fluid for which the stress scales like $\sigma \sim \dot{\gamma}^m$, while the latter characterizes the power-law behavior of the sloped stress plateau in the flow curve $\sigma \sim \dot{\gamma}^{m_{fc}}$. The two factors must be equal when the system is stable. The two factors are generally different in case the power-law dependence in the flow curve is the result of the shear-banding instability. We find that the two factors are indeed different for the 0, 5, 10 mM salt concentrations roughly over the same shear rate range as found from the lever rule, indicating that the curved velocity profiles originate from the shear-banding instability. The sample with the very high salt concentration of 1 M can not be analyzed in this way, since the difference between the two factors is within experimental error. A stability diagram is constructed, which summarizes the several velocity profiles that occur in the added-salt-concentration versus shear-rate plane.

There are two generally excepted mechanisms for the widening of the interface. First, the widening can be observed when the interface between the bands becomes unstable[96, 98, 99, 100, 101]. However, this is unlikely to be the case. We showed that velocity profiles are stable on a time scale of several seconds to an hour, see Fig 3.7. Moreover, the correlation functions, which are very sensitive to sub-second fluctuations, show lower contrast when the systems displays sharp shear bands, but the contrast increases when moving away from this region, precisely when the interface widens. Second, broad interfaces may be due to shear-gradient induced mass transport, leading to variation of the concentration and thus to the variation of the local viscosity [9, 102]. Such mass transport most probably leads to a very slow establishment of the stationary velocity profiles, which is not observed in the present work.

The fact that samples with very similar flow curves and relaxation dynamics, as witnessed by the scaling behavior of the rheology, produce velocity profiles ranging from sharply banded to curved, suggests that molecular interactions (flexibility, repulsive interaction as well as friction between sliding chains) play an important role in shear-band formation and potentially in the widening of the interface. The Rolie-poly model for dynamics of polymer melts is the only model that takes friction between sliding polymer chains into account[7], but also the Rouse time and reptation time of the polymer. All of these parameters

are affected by the ionic strength as the interaction between the polymers as well as the stiffness of the polymers strongly depend on the ionic strength. A model similar to this Rolie-poly might therefore be applicable to our xanthan solutions, taking this into account.

The direct relation between birefringence and shear-band formation, as observed earlier for many other systems, see Fig. 3.15, suggests that stiffness is the most important prerequisite for shear-banding. However, similar experiments on DNA suggest that electro-static repulsion facilitates the shear induced alignment [80]. In order to understand the link between molecular interactions and shear-band formation one possibility is to connect the rate at which entanglements are swept out to the ease with which a sharp interface is formed, which is given by the shear curvature viscosity [5] or, equivalently, the stress diffusion coefficient[6]. Better controlled and tunable systems are required to make such a link.

Finally, we want to evoke awareness with this work of the possibility of shear-band formation in xanthan solutions, which are rather polydisperse and not well-characterized, but nevertheless heavily studied before. Previously wall slip [103] and hints of shear-banding[104] in xanthan solutions have been reported, but this is the first systematic study that identifies a region of shear-banding. This is crucial for the correct interpretation of conventional rheological results, and therefore of industrial importance[85]. These results also extrapolate to many other products that are used as rheology modifiers.

3.5 Summary

In this chapter, we presented the velocity profiles of entangled xanthan at different concentrations and ionic strengths. We showed that shear banding can be found when the concentration is sufficiently high, which is connected with the formation of a stress plateau at the high concentration. At this high concentration shear banding with sharp interfaces was observed only at low ionic strength, while it is suppressed at higher ionic strength. This is a surprising finding as the shear thinning factor is not affected by ionic strength.

We showed that the suppression of the shear banding occurs via a broadening of the interface. We employed a new analysis methods, which allows to differentiate between the effect that the inhomogeneous stress distribution throughout the co-cylinder shear cell has on the velocity profile for shear thinning fluids, and the broadening of the interface itself. These two effects have led to confusion in the past concerning the issue of shear banding of polymeric systems.

There is a direct relation between flow alignment and the formation of shear

bands with a sharp interface, as the broadening of the interface is connected with a strong decrease of flow birefringence. Interpreting the interplay between alignment and shear banding, one should consider that the stiffness and the interaction potential of xanthan both strongly depend on the ionic strength At high ionic strength, when xanthan is flexible and neutral, this results in a very polymer-like system. Thus the behavior of xanthan may aid to resolve the ongoing dispute concerning shear-banding of highly entangled polymeric systems. However, for a full understanding we need to compare the flow behavior of xanthan with the flow behavior of other systems which are better controlled and with intrinsic stiffness, such that both the effects of stiffness and interaction have on shear band formation can be isolated. To this end we choose DNA, and the effect of the ionic strength on shear band formation in DNA solutions is discussed in the next chapter.

Chapter 4

Tuning Shear Banding and Wall Slip in Entangled DNA by Ionic Strength

4.1 Introduction

There has been a considerable debate whether shear banding occurs or not in entangled polymer systems, let alone to understand the mechanism of shear banding in entangled polymer solution. Entangled polymer systems that have been reported to show shear banding up to now are wormlike micelles[35, 17], poly(acrylamide)[72, 68], polybutadiene[54, 55, 56, 57], and DNA[58, 59, 60, 61]. While the occurrence of shear banding in polybutadiene and also polystyrene is still under debate[62, 63, 64, 65], all well-established shear banding observed in entangled polymers are related to some specific property of the constituting particles albeit patchy interactions[44, 68], the stiffness and living character[38, 42, 80]. For example, the proximity of the Isotropic-Nematic (I-N) phase transition and chain breakage both play a role in the existence of shear banding in worm-like micelles[17, 18, 35, 36, 37, 38]. In associative polymers like polyacrylamide, there is hydrogen bond breakage above a critical shear rate which can be the possible mechanism for the shear banding[68].

DNA can be thought of a particle that links the behavior of polymers to the behavior of wormlike micelles, which are the most used category of systems used for the study of shear banding. DNA is a poly-electrolyte that can be described

as worm-like polymer with a high persistence length of about $30 - 55$ nm and effective thickness of $2 - 8$ nm, depending on the ionic strength, which are numbers similar as one can find for worm-like micelles. However, DNA is a covalently bound chain, and therefore does not have breakage as stress relaxation mechanism, contrary to worm-like micelles.

The beauty of DNA is that its flexibility and electrostatic repulsion between the sliding chains can be easily tuned by ionic strength. It can be more like a neutral polymer-like at high salt concentration and more like semi-flexible rods at low salt concentration. Hu et al. found that shear banding is suppressed when DNA becomes more entangled or polymer like with higher ionic strength[80]. They speculated that the mechanism of shear banding in DNA might be the I-N phase transition. Nevertheless, wall slip was not taken into account and they did not perform a careful analysis of the velocity profile data. Moreover, there is a threshold molecular weight of 10^6 base pairs(bp) , below which simulations show that DNA cannot be considered as an ideal polymer model[105], whereas the DNA used for shear banding studies is usually lower than 10^6 base pairs.

The nature of wall slip in entangled polymer solutions is due to the failure between the wall and the polymers network. Wall slip can be tunned by modifying the physical or chemical properties of the shear cell or using high viscosity solvents [60]. In wormlike micelles, Lettinga et al. enforced "stick" boundary condition by using a rough sandblasted Plexiglas Couette cell and partial "slip" boundary condition by using a smooth Plexiglas cell and found that wall slip competes with shear banding in stress release in wormlike micelles[67]. In entangled DNA, Hemminger et al. observed a parabolic flow in channel flow for an APTES-treated glass (with strong interaction with DNA) in the absence of slip, while a significant amount of slip has been observed for a regular glass (with a weak interaction with DNA)[106]. If the interaction between the moving wall and polymer network is strong, disentanglement of chains in the slipping layer occurs[107]. In this work, we use silicate glass material for the shear cell without any surface modification, and observe wall slip in entangled DNA. Whether the competition between shear banding and wall slip still holds for DNA, which are covalently bonded and cannot release stress by chain disassociating, is still unclear.

Therefore, we study in this chapter the effect of ionic strength on the interplay between wall slip and shear banding in DNA in order to shed light on the mechanism of wall slip and shear banding in polymers and help to solve the discrepancy in literature on shear banding in entangled polymers.

4.2 Material and Methods

Calf Thymus DNA (ds DNA) was purchased from USB co. The CT DNA fiber was first dissolved in aqueous buffer with 10 mM NaCl, 0.2 mM EDTA and 10 mM Tris-HCl (PH=7.9) at a concentration of about 0.5 mg/ml. Any un-dissolved impurity was spun down with a speed of 3500 rpm on a centrifuge for 1 h at 4 ^oC. The supernatant was further purified by filtering against an excess of the same buffer with $50k$ cutoff Semico filter(Sigma) in order to remove any salt or other soluble impurity from the sample and concentrated to about 6 mg/ml as measured by UV-Vis (Nanodrop). The sample then was homogenized on a vortex for more than 1 day at 6 ^oC. The final concentration was measured on Nanodrop and adjusted to 6 mg/ml. Samples with higher salt concentrations of 0.1 M and 1 M were prepared by dissolving different amount of $NaCl$ in the same matrix sample.

Gel electrophoresis was carried out on a 0.5% agarose gel under 130 V in TE buffer for 3 hours at room temperature. The image is taken by a Gel Doc. EZ imiger (Bio-Rad). In each lane, 200 ng DNA with a concentration of 0.0333 ug/ul in terms of DNA base pairs was loaded. Lane 1, 2 and 4 contain DNA with molecular weight(Mw) of $10kb$, $20kb$, and $30kb$. Lane 3 is the Calf Thymus we used in the work, and Lane 6 is λ DNA, which has a Mw of $48.5kb$.

Rheological measurements were carried out using a ARES rheometer (Rheometric Scientific Inc., NJ) equipped with a cone-plate shear cell with a cone angle 0.04 rad, diameter of 25 mm and a gap distance of 0.046 mm at 20 ^oC. To prevent water evaporation during rheological measurements, the meniscus of the aqueous DNA solution in the cone-plate cell was surrounded by anti-evaporation silicone oil (Ibidi).

Flow velocity profiles were obtained at 20 ^oC with the HDLS setup described in Chapter 2. In order to gain structural information of the sample during shear, we probed the alignment using birefringence measurements. To this end, we directed a separate laser beam along the gradient direction of the Couette cell, which was placed between two crossed polarizers that were rotated 45^o with respect to the flow direction. We monitored the transmitted intensity by means of a diode, thus probing orientation in the flow-vorticity plane. Moreover, images of the sample during steady shear were taken between same crossed sheet polarizers using a white light box in order to probe the birefringent structure.

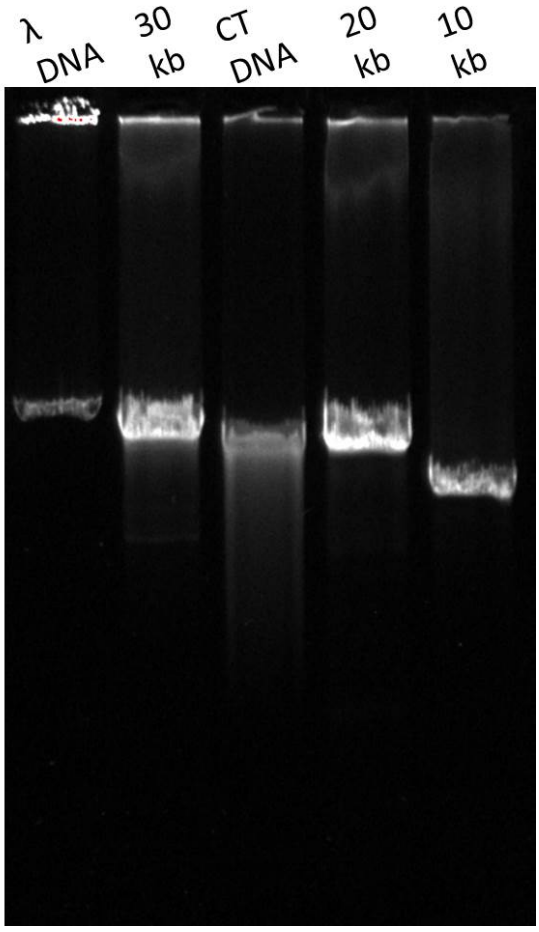

Figure 4.1: Gel electrophoresis of the samples on 0.5% agrose gel under 130 V for 3 hours at room temperature. Lane 1-5 are 10kb DNA, 20kb DNA, Calf thymus DNA, 30kb DNA and Lambda DNA which has a Mw of 48.5kb, respectively.

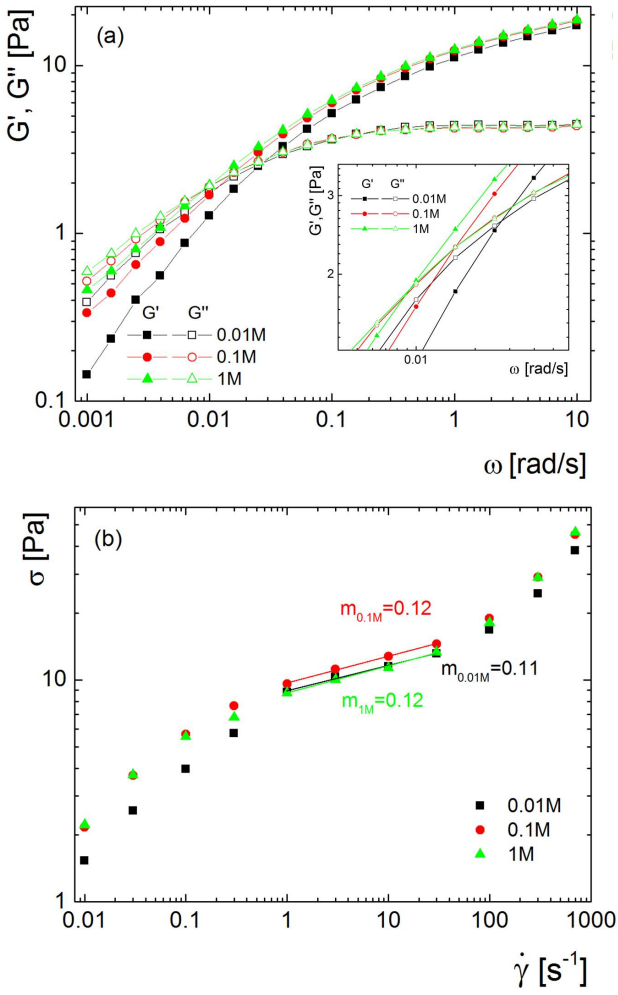

Figure 4.2: (a) The storage G' and loss modulus G'' and (b) the stress σ in the stationary state as a function of the shear rate $\dot{\gamma}$, for 6 mg/ml Calf Thymus DNA with 0.01 M, 0.1 M and 1 M salt at 20 ^oC. The inset in (a) shows the magnification of the crossover frequency. The lines in (b) are linear fits to the experimental data, which indicate over what range the shear-thinning exponent m_{fc} , as defined by $\sigma \sim \dot{\gamma}^{m_{fc}}$, was determined.

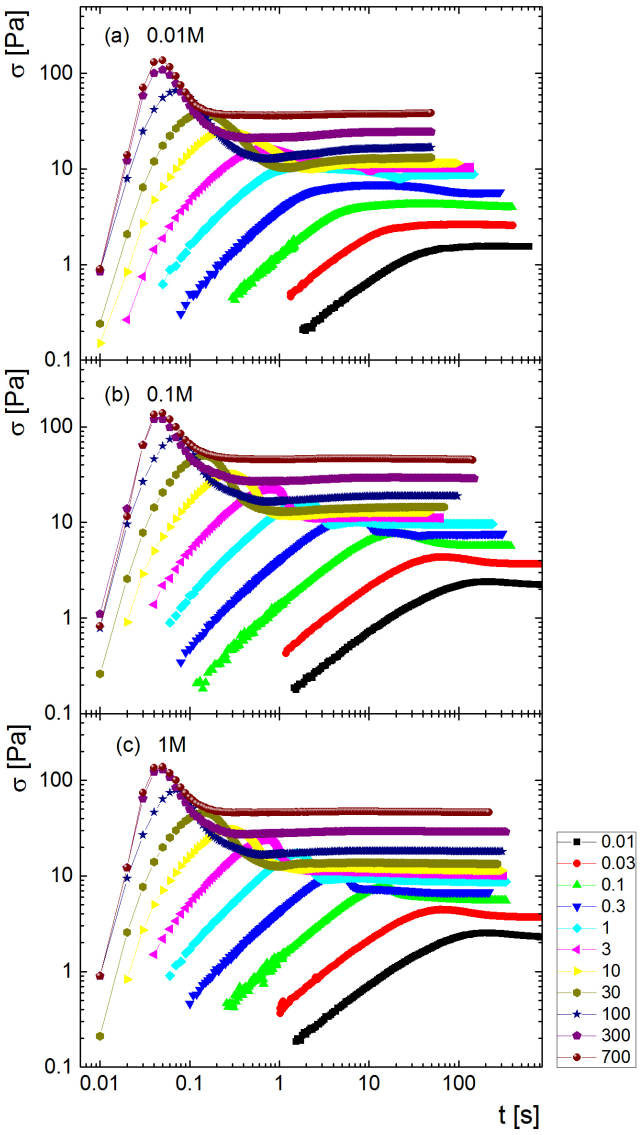

Figure 4.3: Stress development in startup shear at various shear rates, as indicated in the legend in s^{-1}, for 6 mg/ml Calf Thymus DNA with 0.01 M (a), 0.1 M (b) and 1 M (c) added salt at 20^oC.

4.3 Results

4.3.1 Gel Electrophoresis

As can be seen in Fig. 4.1, DNA with Mw=10kb migrated fastest in the gel. Calf Thymus DNA migrated with the same speed compared to the DNA with Mw=20kb, and DNA with higher Mw migrated slower on the gel. Therefore, the Mw of the DNA is about 20 kb, meaning the contour length L of the DNA is about 6.8 μm. The overlap concentration c* is about 0.07 mg/ml[59], indicating the 6mg/ml DNA we used are well-entangled.

4.3.2 Rheology

Fig. 4.2 shows the linear and nonlinear rheology of all the samples. As can be seen in Fig. 4.2a, both the loss and storage modulus increase while their crossover frequency decreases with added salt. The relaxation time of the system, which is defined as one over the crossover frequency, increases from 226 s for 0.01 M salt to 671 s for 1 M salt. This slower chain dynamics and higher modulus at higher salt concentrations could be attributed to: a), the increasing flexibility of DNA at higher salt concentration which would lead to an increased entanglement number; b) screening of the charge on DNA which would decrease the local repulsion at local entanglement, i.e. increasing friction between the sliding chains. This could also account for the higher stress on the flow curves (the stress as a function of the applied shear rate) at high ionic strength, see Fig. 4.2b. However, the flow curves are quite similar, all showing a plateau from about 1 to 100 s^{-1}, with a shear thinning parameter of about $m_{fc} = 0.12$, see Eq. 2.4. This strong shear thinning implies that shear banding might occur in the system.

The flow curves are constructed from the steady state viscosity, which is reached after a startup shear protocol, as shown in Fig. 4.3. The three samples show a similar trend: at shear rates lower than $Wi = \tau\dot{\gamma} = 1$, the stress increases monotonically with time, while at higher shear rates a stress overshoot is seen, which means that the response is relatively slow compared to the shear rate. All flow curves reach steady state after a certain amount of time. The stress overshoot for 0.01 M, see Fig. 4.3a, appears at higher shear rates compared to that of higher salt concentration, which reflects the shorter relaxation time, see Fig. 4.3b-c. In the heterodyne measurements, velocity profiles were measured after the steady state was reached, using the measurements presented in Fig. 4.3 as a reference.

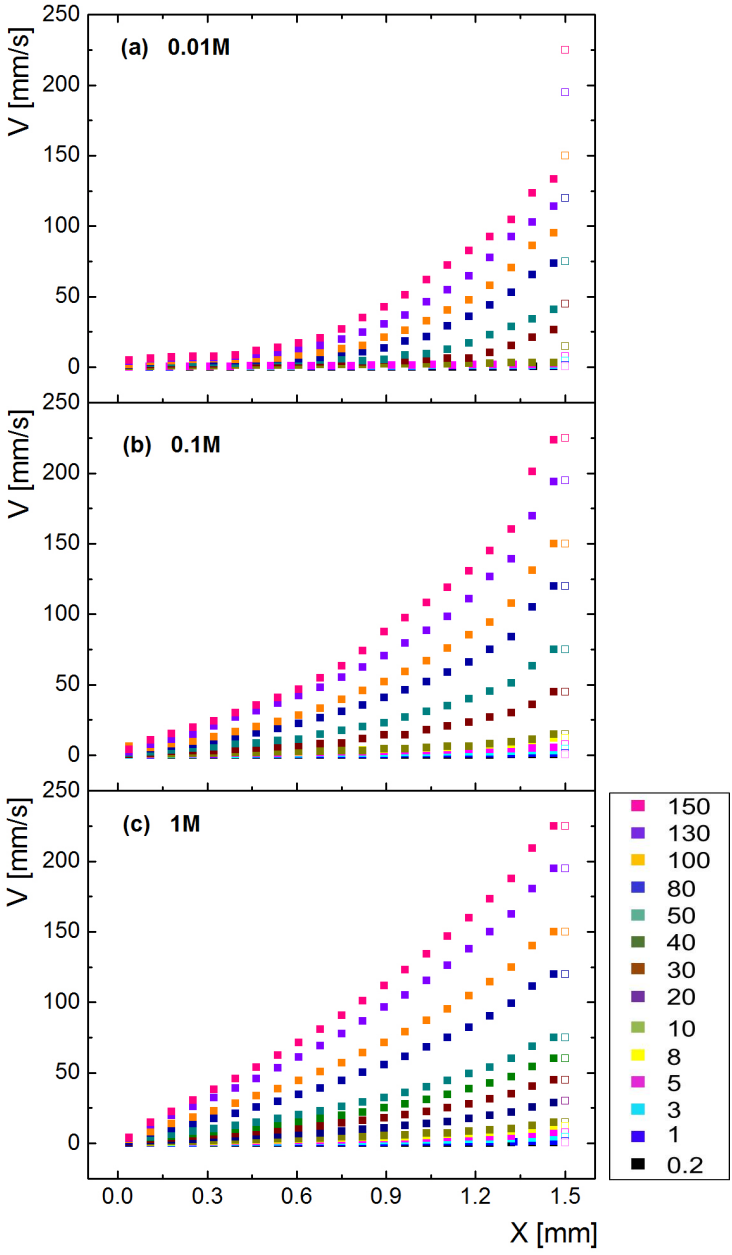

Figure 4.4: Steady state velocity profiles at different shear rates which are indicated in the color bar in s^{-1} for 6 mg/ml Calf Thymus with 0.01 M (a), 0.1 M (b) and 1 M (c) added salt at 20 ^oC. The open points indicate the applied velocity for each shear rate.

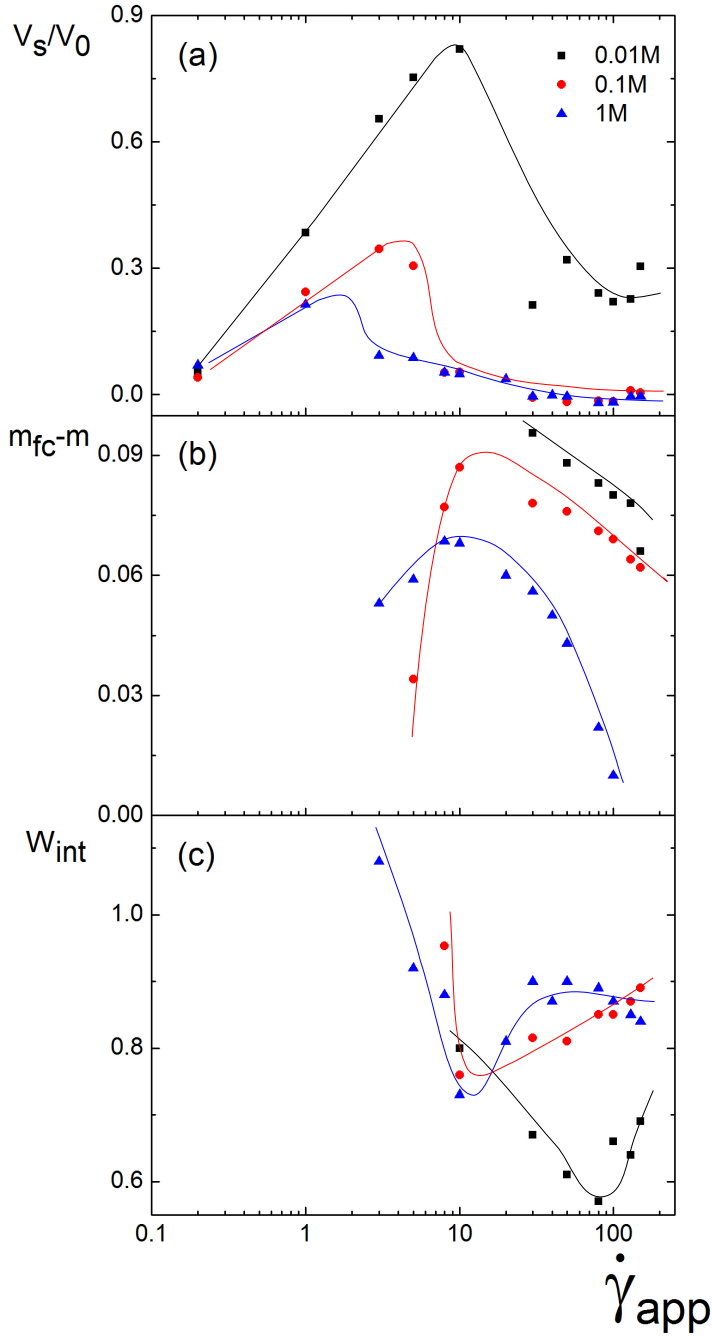

Figure 4.5: (a) Relative slip velocity V_s/V_0; (b) the difference of the exponents m_{fc} as determined from the flow curve and m as determined from the shear-thinning-function fit; (c) the width of the shear-band interface versus applied shear rate for 6 mg/ml Calf Thymus DNA at different ionic strengths as indicated in the figure. The solid lines are guides-to-the-eye. Note that the gap width is 1.5 mm.

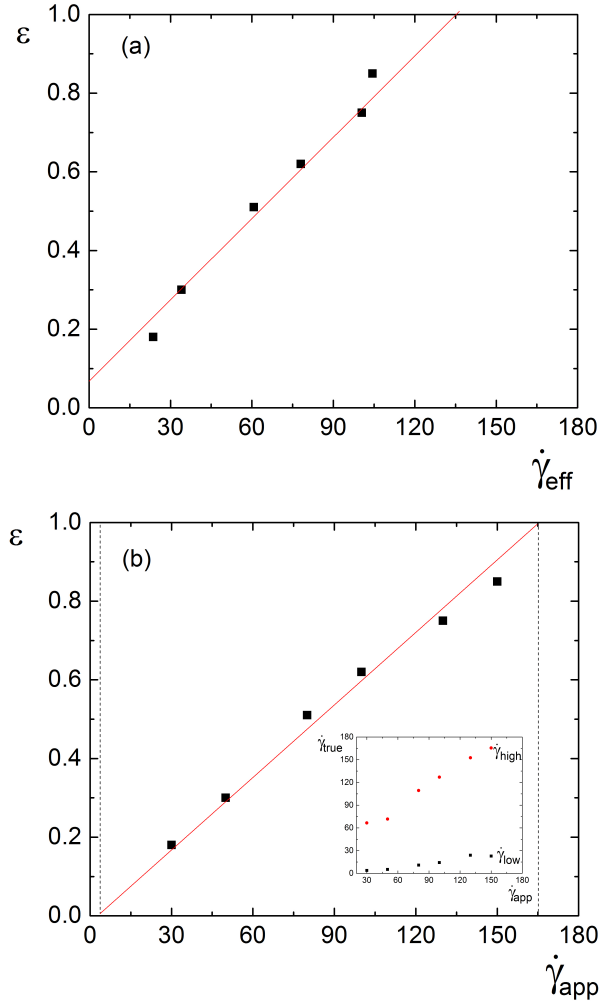

Figure 4.6: The lever-rule plots for 6 mg/ml with 0.01 M added salt, where the fraction ϵ of the volume occupied by the high shear-rate band is plotted against the effective shear rate(a) and applied shear rate(b). The data points are based on the determination of ϵ from the velocity profiles with a sharp interface. The inset in (b) shows the shear rates in the high and low shear-rate bands as a function of the applied shear rates (in s^{-1}) for the system with 0.01 M added salt.

4.3.3 Velocity Profiles and Analysis

The velocity profiles of the entangled DNA for varying salt concentrations are presented in Fig. 4.4. The velocity profiles are linear at low shear rates and become curved at higher shear rates for all samples. The velocity profiles of the sample with 0.01 M salt display substantial wall slip and are very curved, see Fig. 4.4a. Velocity profiles at higher salt concentrations display less wall slip and become more linear. Thus, it seems that wall slip and shear banding are both suppressed by increasing ionic strength.

Wall slip of the velocity profiles are quantified in terms of V_s/V_0 and plotted in Fig. 4.5. For all three samples, the relative wall slip velocity increases linearly with shear rate at low shear rates and then decrease at higher shear rates. The 0.01 M sample shows the largest wall slip velocity and less wall slip is observed for the samples with higher ionic strength. Furthermore, the maximum wall slip is found in the lower shear rate region for samples with higher ionic strength.

The drop in V_s/V_0 at higher shear rates might be related to the occurrence of shear banding in this shear rate region. By comparing the R^2 of the shear thinning function(STF) and the piece wise linear function (PWLF)(see Chapter 2), we find that the velocity profiles at shear rates higher than 30 s^{-1} are classic shear banded velocity profiles with a sharp interface for the 0.01 M sample, while the 0.1 and 1 M samples only shows classic shear banded velocity profiles at shear rates between 5 and 10 s^{-1}. As can be seen in Fig. 4.6a, the high shear rate fraction ϵ of the 0.01 M sample plotted against effective shear rate lies on a straight line for all samples, meaning that the Lever rule still holds. The data points lie on a straight line even if it is plotted against applied shear rate, see Fig. 4.6b. The reason is that the relative wall slip is always close to 0.25 for the shear rates where classic shear banding occurs. However, the extrapolation of the line goes to negative shear rate in Fig.4.6a, while the extrapolation of the straight line is positive when ϵ is plotted against the applied shear rate. Moreover, the values of low and high shear rate given by Fig.4.6a are 5 s^{-1} and 165 s^{-1}, which is consistent with the plateau region on the flow curves. Furthermore, the difference between the shear thinning factor derived from the flow curve and the velocity profile, $m_{fc} - m$, remains high for a large range of shear rates. This means that the measured velocity profile is more curved than could be expected from only the shear thinning, indicating that shear banding states(SBI) still exists in these velocity profiles. Moreover, $m_{fc} - m$ for the 0.01 M sample remains higher than that of the samples with higher ionic strength, indicating that the sample is more shear banded at low ionic strength, as seen in Fig. 4.5b. The interface width W_{int}, calculated following the protocol proposed in Chapter 2, confirms this, see Fig. 4.5c. The interface width is smallest for 0.01 M added salt and increases with ionic strength.

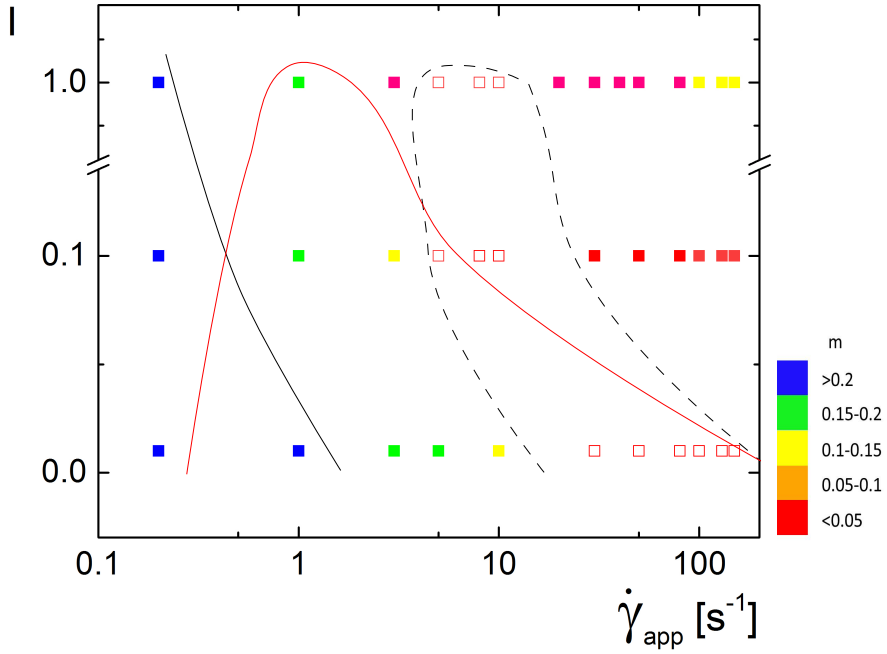

Figure 4.7: The diagram-of-states in the ionic strength I versus the applied shear-rate plane, where velocity profiles are distinguished depending on the shear-thinning parameter m. The open points indicated by the black dash line refer to banded profiles with a sharp interface(when R^2 of the PWLF fit overtakes the R^2 of the ST fit). The black solid curves indicate m higher or lower than m_{fc}, which is about 0.2. The region below the red solid line displays substantial wall slip($> 20\%$).

4.3.4 Diagram of States and Birefringence

From the above analysis, we infer that the competition between wall slip and shear banding also takes place for DNA like as it does for wormlike micelles[67], as wall slip is suppressed when shear banding sets in for all three samples, see Fig. 4.5. The competition between wall slip and shear banding can be more explicitly described in the diagram of states, see Fig.4.7. The shear rate region where wall slip occurs drastically shrinks by ionic strength, as indicated by the red curve. Shear banding regime where sharp interfaces are observed is pushed to lower shear rates due to decreased wall slip at higher ionic strength, see the dashed curved in Fig 4.7. However, the overall curvature of the velocity profiles when shear banding occurs is smaller at higher ionic strength as indicated by

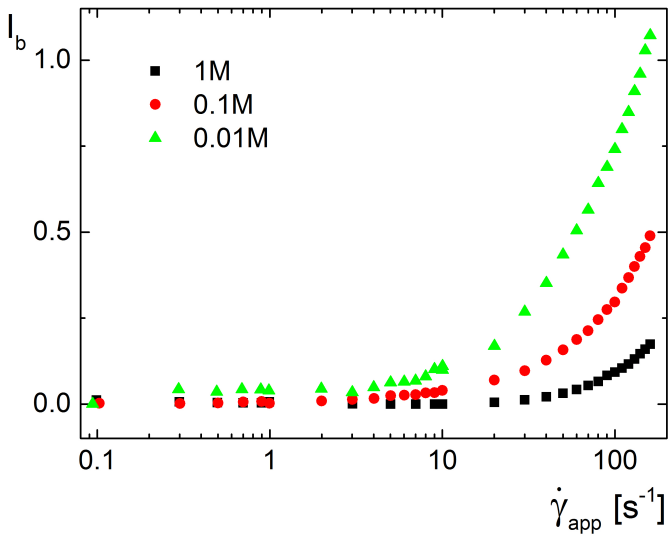

Figure 4.8: The transmitted intensity I_b at varying applied shear rate for 6 mg/ml DNA solutions at different salt concentrations.

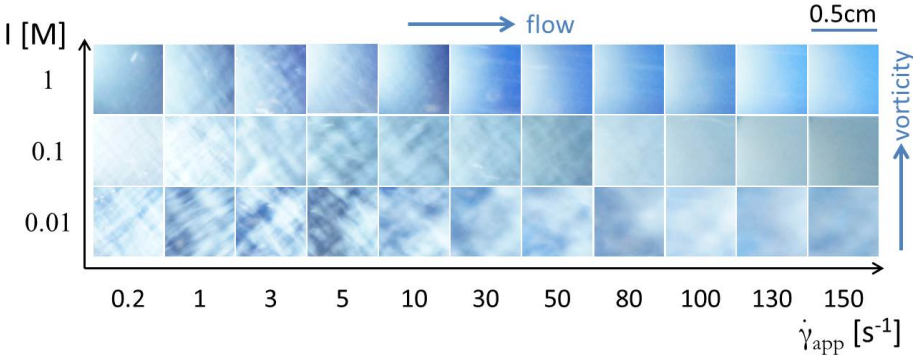

Figure 4.9: Images taken between crossed polarizers at varying applied shear rate for 6 mg/ml DNA solutions at different salt concentrations.The flow and vorticity direction are indicated by the arrows and the scale bar is 0.5 cm.

the color of the data points. Thus, the addition of salt suppresses both wall slip and shear banding.

In order to elucidate the mechanism behind these observations, the birefringence

intensity and patterns of the sample during steady shear are measured. As can be seen in Fig. 4.8, the transmitted light intensity(I_b) between crossed polarizer increases with shear rate for all three samples due to disentanglement-induced-chain alignment. However, I_b decreases with increasing ionic strength at a fixed shear rate, indicating that less chain alignment occurs at higher ionic strength. This is confirmed by the birefringence patterns shown in Fig. 4.9. The 0.01 M sample shows crossed birefringence patterns at low shear rates while cloud-like patterns are observed at higher shear rate. These pattern are similar to the birefringent patterns observed in other supra-molecular polymer solutions[42, 108]. For higher ionic strengths, birefringence patterns are only observed at low shear rates. The shear rate region where crossed birefringent pattern occurs overlaps with the wall slip region in the diagram of states shown in Fig. 4.7. Therefore, the crossed birefringent pattern should be attributed to the disentanglement of the chains near the moving wall due to wall slip. The cloud-like pattern might be attributed to shear banding since the high shear rate fraction increases with shear rate which would blur the birefringent pattern.

4.4 Discussion

The effect of ionic strength on wall slip and shear banding of entangled DNA is systematically studied by rheology, velocity profiling and birefringence measurements. It is found that wall slip and shear banding compete with each other and are both suppressed with increasing ionic strength and are associated with birefringence. When the salt concentration is as low as 0.01 M, there is well defined shear banding with large wall slip accompanied by high flow-induced-birefringence intensity. When the salt concentration is 1 M, where the system is the most entangled or polymer-like, almost no shear banding exists along with the least wall slip, accompanied by low birefringence intensity and the disappearance of the flow induced birefringent pattern. Thus, similar to xanthan the mechanism for suppression of shear banding is gradually taking place via the widening of the interface. This means that for sheared polymers that do display a pronounced curvature, where $m_{fc} - m > 0$, can be considered as shear banding, even though no sharp bands can be identified. Having confirmed this effect for a better defined system we can discuss the mechanism in more detail. First, however, we discuss the competition between shear banding and wall slip.

The flow curves for different ionic strengths suggest that flow instabilities set in at more or less at the same shear rate between $\dot{\gamma}_{app.} = 0.1$ and 1 s^{-1}. At low ionic strength we observe that at low shear rates flow instability manifests itself in the form of wall slip reaching almost complete slip at a relative high shear rate of $\dot{\gamma}_{app.} = 10\ s^{-1}$, after which the slip velocity drops and shear banding

takes over, see Fig.4.5a. With increasing ionic strength shear banding sets in at lower shear rates at lower slip velocities. The competition between wall slip and shear banding is similar to that in worm-like micelles[67], but differs as there the slip velocity stays constant at high shear rates. As can be seen in Fig. 4.6, wall slip has an effect on ϵ where the extrapolation of the lever rule plot goes to negative, suggesting that the transition between wall slip and shear banding is continuous. The nature of wall slip in entangled polymer solutions is due to failure between the wall and the polymer network. In this case the a silica glass wall and aqueous DNA solutions needs to be considered. Silica and silicate glass surfaces immersed in water are known to acquire a negative surface charge density, primarily through the dissociation of terminal silanol groups[109]. This results in a strong repulsion between the negatively charged DNA chains and glass wall at low salt concentrations, leading to weak wall-sample interfacial strength. When the salt concentration increases, the negative charges along the DNA chains and the surface of the shear cell are both largely screened, resulting in a stronger wall-sample interfacial strength. This could be the reason why wall slip is suppressed at higher ionic strength. It could also be that the underlying constitutive relation for sheared DNA at high ionic strength does not display strong stress overshoots, so that the tendency for wall slip as well as shear banding is reduced. However, the stress overshoot is very similar for all samples, as we see in Fig. 4.3.

The fact that shear banding can be tuned by the ionic strength can be attributed to three effects: changes in the degree of entanglement, changes in the friction between the polymers and changes in the proximity of a thermodynamic isotropic-to-nematic (I-N) phase transition. Concerning the entanglement Tree et al.[105] state that the required molecular weight of ds DNA to be ideal polymer model is about 10^6 base pairs. The molecular weight of the CT DNA used in this work is about 20kb, see Fig. 4.1, indicating that the DNA behaves somewhat rod-like or wormlike, especially at low ionic strength of 0.01 M. Indeed, the effect of ionic strength on entanglement does not seem to be pronounced as all three samples display very similar stress overshoots, which is a prerequisite for shear banding according to Wang et al.[92, 110], see Fig. 4.3. Moreover, Fig. 4.2a suggests that at high ionic strength the system is more entangled as the relaxation time shifts to lower frequencies with increasing ionic strength. This means that for higher ionic strength, the same shear rate would yield a higher $Wi = \tau\dot{\gamma}$ and thus would be more likely to show shear banding. However, the results show the opposite: there is no shear banding when the system is more entangled. Thus, entanglement is not enough for shear banding, as was also suggested by Hu et al.[80].

Shear banding is often described as a shear induced transition from the isotropic to nematic phase transition, where the low shear high viscosity band is the

entangled isotropic phase and the high shear rate low viscosity band is the disentangled and aligned nematic phase [102]. This idea originally came from measurements on wormlike micelles [35, 111], but it is also reflected in the flow-induced-birefringent pattern for the 0.01 M sample where shear banding occurs, while it disappears at higher salt concentrations where shear banding is largely suppressed (Fig. 4.4 and 4.8). Indeed, the I-N transition for the long DNA used in this thesis is at a concentration that is about a factor two higher than the concentration used[112]. However, in Ref. [112] the ionic strength was 0.1 M. At the lowest ionic strength used the stiffness of DNA increases slightly[113], but, more importantly, the D_{eff} of DNA changes from 8 to 3 nm going from 0.01 M to 1 M. As the effective volume thus strongly increases, the low salt sample will be close to the I-N transition, even though the flow induced birefringence will disappear within seconds after cessation of flow which means that in equilibrium the sample is in the isotropic phase. Hence it is easier to form a shear induced nematic phase in the high shear rate band in the low salt case. Hu et al.[80] also proposed a shear-induced nematic phase transition mechanism for shear banding in DNA judging from the low viscosity of the high shear band, while it has been shown for several systems that the direct proximity of the equilibrium I-N is connected with the hydrodynamic shear banding instability [48, 114]. Note that the PB-PEO block-copolymer wormlike micelle system charge is not charged but just relatively stiff.

Since shear banding in polymers is always related to disentanglement, also the friction between the sliding chains could affect shear band formation in DNA solutions. At low salt concentrations, the negative charge on DNA keeps the chains far away from each other, making the local friction at each entanglement low. Under stress, this low local friction assures that the system can easily disentangle and form an interface. At higher salt concentrations, the chains are closer to each other so the entanglement points are more tight. This might lead to very local fractionation, resulting in homogeneous flow with little alignment.

To conclude, the ionic strength dependence of the shear band formation of DNA, but also of xanthan, suggests that the proximity of the I-N transition facilitates shear band formation. This can either be tuned by stiffness as well as the effective volume fraction. However, moving away from I-N transition we observed no difference in the rheology, which means that stress can be released not just by alignment, but also purely by disentanglement, which might be influenced by friction. The fact that disappearance of birefringence comes along with the broadening of the interface with increasing ionic strength, suggests that alignment facilitates the formation of a sharp interface. It is conceivable that there are other mechanisms to sustain alignment after disentanglement as shear banding can also occur when the concentration is far from the equilibrium isotropic to nematic phase transition in the case of

surfactant worm-like micelles[17, 36]. Generally, it is not a requirement to be close to the I-N as long as 'clusters' in one band are in an aligned state, thus reducing stress[108].

This hypothesis could be tested when preparing a system that will shear band, such as DNA at sufficient low ionic strength, and the alignment of the system can be tunned by inducing a intra-molecular force that drives a collapse of the system. This is the objective of the next chapter, where we will use PNIPAM-grafted DNA, using temperature to induce the collapse due to the thermal responsive polymer brush.

4.5 Summary

In this chapter, the effect of ionic strength on wall slip and shear banding of entangled DNA was systematically studied along with birefringence measurements. When the salt concentration is as low as 0.01 M, there is well defined shear banding along with considerable wall slip , accompanied by high flow-induced birefringence intensity and birefringent patterns. When the salt concentration is 1 M, where the system is the most entangled or polymer-like, almost no shear banding and little wall slip occurs, accompanied by disappearance of birefringent patterns. These findings suggest that in principle stress can be released purely by disentanglement, but that disentanglement combined with sustained orientational ordering is required to form sharp interfaces. In the proximity of a thermodynamic isotropic-nematic phase transition a para-nematic phase is readily formed, thus also the interface between bands. Therefore, shear banding is not a general property for strongly shear thinning polymeric systems, but subtly depends on the molecular properties of the system. It can completely disappear via the widening of the interface, when there is no induced orientational order in the system. This we will try to tune in the next chapter, by inducing a mechanism that can cause a collapse of the disentangled polymer.

Chapter 5

Tuning Wall Slip and Shear Banding in Entangled DNA-PNIPAm Brush-like Polymer

5.1 Introduction

In the previous chapters we have demonstrated that for semi-flexible polyelectrolytes like DNA and xanthan shear banding can be suppressed by adding salt. We speculate that the mechanism of shear banding in these systems at low ionic strength is related to the low friction between the sliding chains. The local friction might be important since it determines whether the system can be easily disentangled and aligned in the high shear rate bands while the low shear rate band stays entangled and coiled, thus creating the interface. An alternative explanation we posed was, however, that the proximity of the isotropic-nematic (I-N) transition depends on ionic strength, as clearly an aligned state is induced during shear banding.

In order to discriminate between the two effects one would ideally tune the friction without changing the location of the I-N transition. Our approach in this chapter is to introduce short PNIPAm chains onto the DNA backbone. PNIPAm is a well-known thermo responsive polymer that undergoes a coil to globule transition above its low critical solution temperature (LCST) of

about 32 ^oC. The collapsed PNIPAm chain becomes hydrophobic and can act as attractive sites on DNA backbone, as was shown for PNIPAm-grafted rod-like viruses[115, 116]. Thus, we can tune friction in the opposite direction as described in the previous chapters, namely by increasing attraction, instead of reducing repulsion. As we will keep the ionic strength low and we will used relatively short polymers, the chains will always be smaller than the Debye double layer, which should leave the I-N transition unaffected, even though the thickness of PNIPAm-DNA will depend on the temperature. However, Iwataki et al.[117] have shown that isolated DNA grafted with PNIPAm exhibits a sharp but continuous transition at around 34^oC, from an elongated coil to a collapsed compact state, which might affect shear band formation.

Moreover, we have learned from the previous chapter that wall slip and shear band formation can be two competing process. A wall constitutes a natural interface, while for shear banding the interface between the bands need to be formed within the sample[67]. In the case of charged DNA suspensions slip might be enhanced as both the glass wall and the DNA are negatively charged. It is conceivable, however, that above LCST the attraction between the wall and the PNIPAm-functionalized DNA is enhanced and that it has different temperature dependence as the interaction between the grafted polymers themselves. Hence, it is to be expected that the PNIPAm-functionalized DNA will drastically affect shear band formation, depending on the temperature. Indeed, we will demonstrate in this chapter that the diagram-of-states in the parameter space of temperature and shear rate, is very rich.

5.2 Material and Methods

5.2.1 Materials

Calf Thymus DNA (ds DNA) was purchased from USB co. The molecular weight of the DNA is about 20 kb, confirmed by electrophoresis, and it is highly polydisperse. The DNA fiber was first dissolved in aqueous buffer with 10 mM NaCl, 0.2 mM EDTA and 10 mM Tris-HCl (pH=7.9) at a concentration of about 0.5 mg/ml. Any un-dissolved impurity was spun down with a speed of 3500 rpm in a tabletop centrifuge for 1 h at 4 ^oC. The supernatant was further purified by filtering against excess amount of the same buffer with $50k$ cutoff Semico filter (Sigma) in order to get rid of any salt or other soluble impurities in the sample and concentrated to about 6 mg/ml. The sample was then mixed on a vortex for more than 1 day at 6 ^oC, rendering a homogeneous sample. The concentration was measured on Nanodrop and adjusted to 6mg/ml. NH_2 terminated Psoralen was purchased from Berry & Associates and NHS

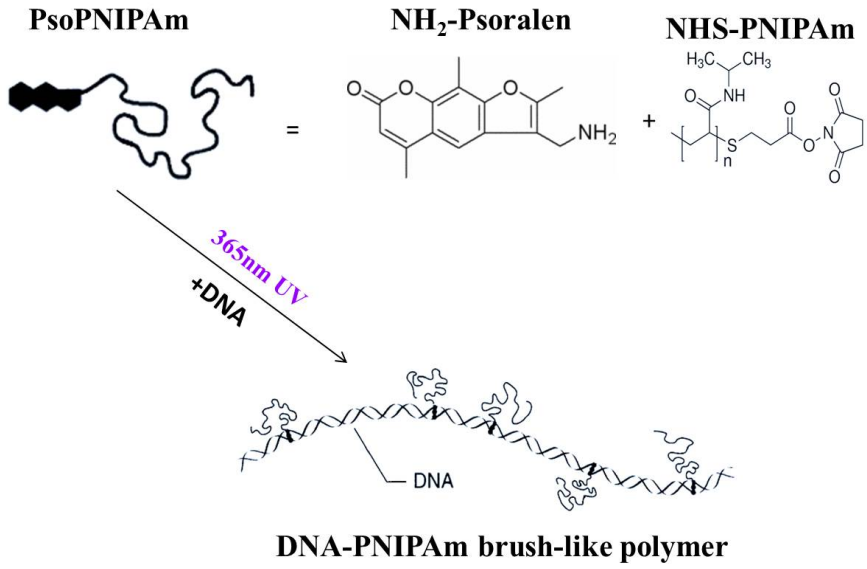

Figure 5.1: Structure of the DNA-PNIPAm brushlike polymer synthesized by a photoreaction between DNA and PsoPNIPAm

ester terminated PNIPAm($Mn = 2k$, $Mw/Mn = 1.7$) was purchased from Sigma-Aldrich.

5.2.2 Synthesis of DNA-PNIPAm Brushlike Polymer

NH_2-Psoralen and $NHS-$PNIPAm are first dissolved in DMF respectively and then well mixed with each other at a molar ratio of 4:1 to make sure that all the PNIPAm chains are functionalized. The resultant solution was kept in the dark overnight. The solution was dialyzed against Milli-Q water, using a dialysis tubing (Sigma-Aldrich) with cutoff of 2000, to remove the DMF and the unreacted Psoralen. The aqueous solution of Pso-PNIPAm was lyophilized and stored at $-20\ ^oC$ for further usage. A solution of 150 mM Calf thymus DNA was mixed in a buffer solution (10 mM NaCl, 0.2 mM EDTA and 10 mM Tris-HCl (PH=7.9)) with Pso-PNIPAm(75mM for the low grafting density and 150mM for the high grafting density) over night. Each 30 ml of the solution was then irradiated for $30min$ on an ice bath with a $6W$ UV lamp equipped with a high-pass filter with wavelength $\lambda = 365\ nm$ (VL-6.L from Vilber Lourmat). Photo reaction between DNA and the Psoralen terminus of the PNIPAm chains

resulted in the grafting of PNIPAm to DNA, giving a DNA-PNIPAm conjugate (Figure 5.1). To remove unreacted PsorPNIPAm the resultant solution was purified with a $100k$ cutoff pore size filter at 3000 rpm on a centrifuge. The sample was then homogenized on a vortex for more than 1 day at 6 ^oC. The concentration was measured by UV-Vis absorption (Nanodrop) and adjusted to 6 mg/ml in terms of DNA base pairs, based on the assumption that the grafting would not change the extinction coefficient of DNA. Note that the Debye length is 3 nm at room temperature, which is larger than the radius of gyration (Rg) of the short PNIPAm that is about $2nm$[118], meaning the PNIPAm layer lies within the Debye double layer of the DNA.

5.2.3 Gel Electrophoresis

In order to test if the grafting is successful, gel electrophoresis was carried out on a 4% agarose gel under 130 V in TE buffer at 6^oC for 3 hours. The image is taken by a Gel Doc. EZ imiger (Bio-Rad). In each lane, 200 ng DNA with a concentration of 0.0333 ug/ul in terms of DNA base pairs was loaded. Lane 1 to Lane 3 contain DNA, DNA-PNIPAm with low grafting density and DNA-PNIPAm with high grafting density, respectively. Lane 4 to Lane 6 are their denatured counterparts which are prepared by heating up to 95 ^oC for 15 min and quenched in ice.

5.2.4 Rheology

Rheological measurements were carried out using an ARES rheometer(Rheometric Scientific Inc., NJ) equipped with a cone-plate shear cell with a cone angle of 0.04 rad, a diameter of 25 mm and a gap distance of 0.046 mm from 20 ^oC to 50 ^oC . Temperature was controlled by a heating circulators with a water bath (JULABO FS18). Each temperature was kept for 30 min after it reached the temperature before the measurements started, in order to obtain a homogeneous temperature distribution in the shear cell. The expansion of the shear cell was found to be linearly depended on temperature and the gap was opened accordingly for higher temperature. Contrary to the last chapters, the flow curves were measured continuously from low to high shear rate in this chapter in order to avoid any disturbance to the system. To prevent water evaporation during rheological measurements, the meniscus of the aqueous DNA solution in the cone-plate cell was surrounded by an anti-evaporation silicone oil (Ibidi).

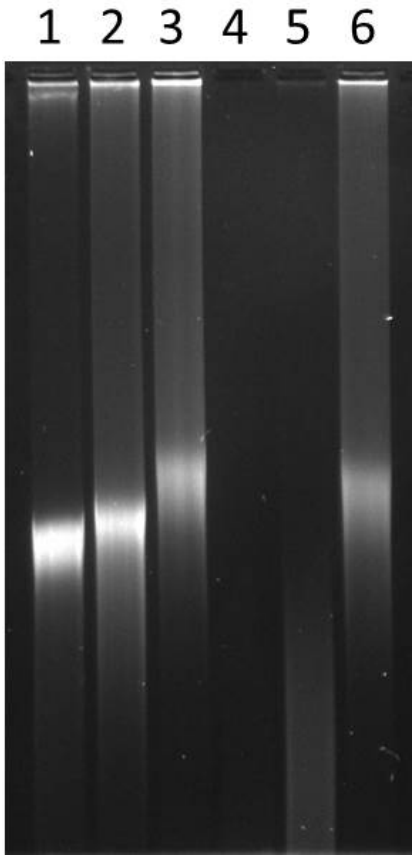

Figure 5.2: Gel electrophoresis of the samples at 6 ^oC under 130 V for 3 hours. Lane 1 to Lane 6 are DNA, DNA-PNIPAm with low grafting density, DNA-PNIPAm with high grafting density and their denatured counterparts, respectively.

5.2.5 Velocity Profile Measurements

The velocity profiles were obtained using the set-up as described in chapter 2. Temperature of the outer cylinder was controlled by a heating circulators with water bath(JULABO FS18) while that of the inner cylinder was controlled by a heating coil which was immersed in the silicone oil inside the inner cylinder.

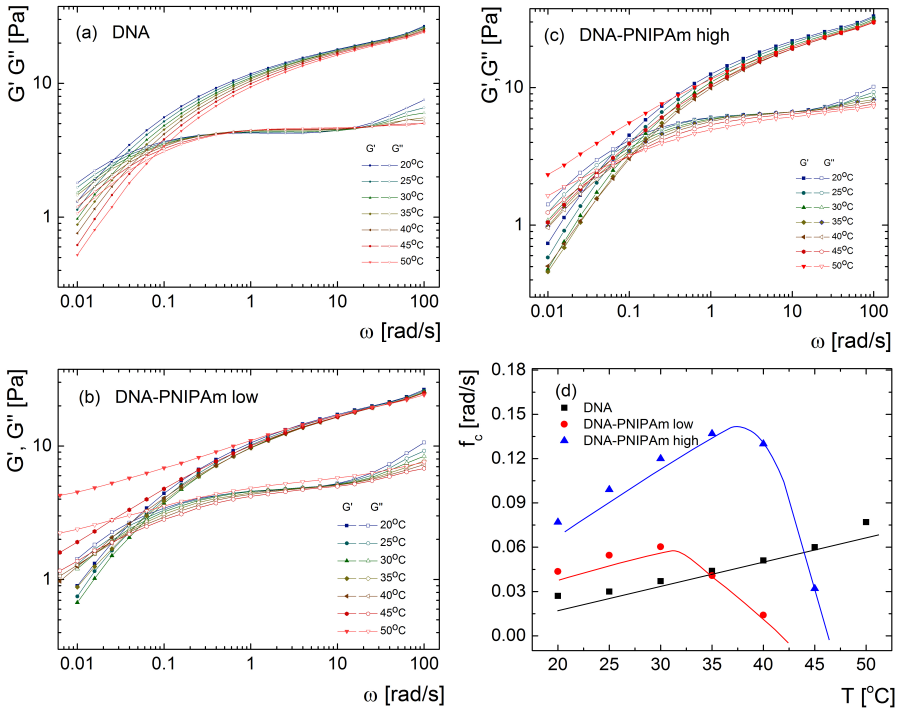

Figure 5.3: The storage G' and loss modulus G'' from 20 to 50^oC for DNA(a), DNA-PNIPAm brush-like polymer with low PNIPAm grafting density(b), and DNA-PNIPAm brush-like polymer with high PNIPAm grafting density(c). The crossover frequency vs. temperature for the samples(d).The lines are guilds to the eyes.

5.3 Results and Discussion

5.3.1 Gel Electrophoresis

Gel electrophoresis shows that the synthesis is successful. First, comparing Lane 1 to Lane 3 in Fig. 5.2, we can see that the sample with higher grafting density migrates slowest due to the higher overall molecular weight. Second, the DNA-PNIPAm brush-like polymers could not be denatured due to the chemically cross-linked strands due to the photochemistry reaction, while pure DNA could be denatured by the high temperature treatment and ran completely through the gel and displays nothing on the gel (compare Lane 4-6 in Fig. 5.2). The denatured low grafting sample migrates much faster than the low grafting

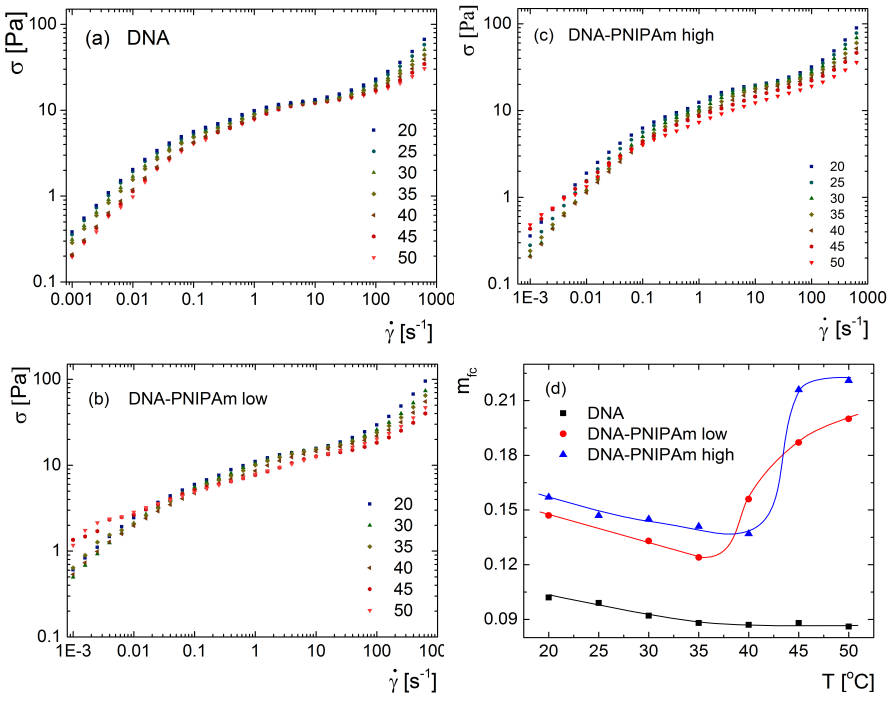

Figure 5.4: The stationary stress σ versus the shear rate $\dot{\gamma}$ from 20 to 50 ^oC, for DNA (a), DNA-PNIPAm brush-like polymer with low grafting density (b), and DNA-PNIPAm brush-like polymer with high grafting density (c). (d) The slope of the plateau for the flow curves m_{fc} vs. temperature for all samples. Note that the values plotted in (d) correspond to the slopes of the second plateau in case two plateaus are present, i.e. between $\dot{\gamma} = 1 - 100\ s^{-1}$. The lines are guilds to the eyes.

density sample since part of its strands are denatured at 95 ^oC. For the same reason, the denatured high grafting density sample migrates a little faster than its undenatured counterpart.

5.3.2 Rheology

Figure 5.3 shows the storage G' and loss modulus G'' for the entangled DNA and DNA-PNIPAm brush-like polymers over a range of temperatures. For pure DNA, both the storage G' and loss modulus G'' decrease while their crossover frequency f_c increases with temperature, see Fig. 5.3a. This is consistent

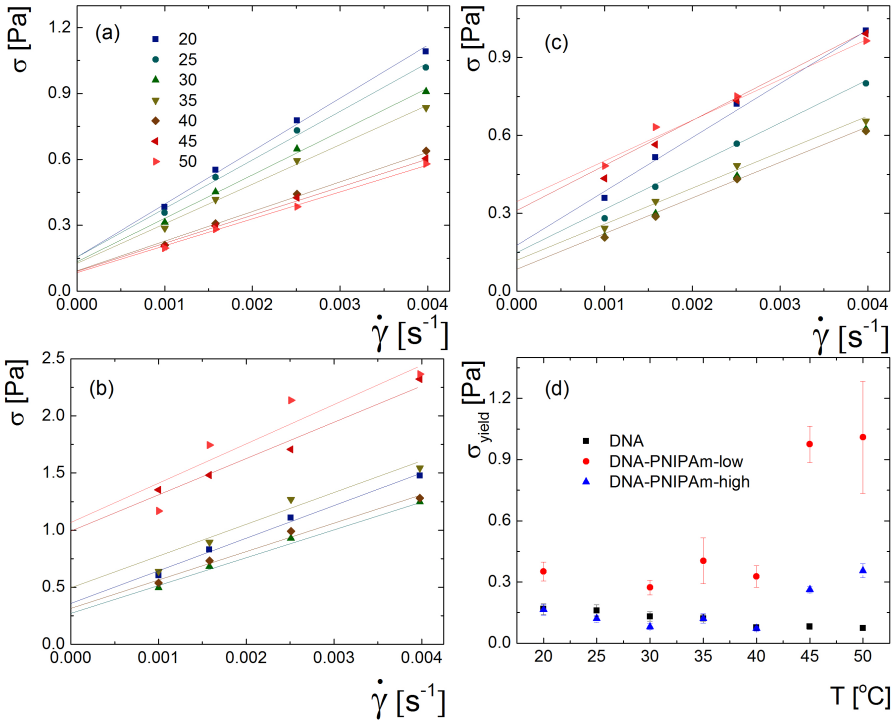

Figure 5.5: The stationary stress σ versus the shear rate $\dot{\gamma}$ from 20 to 50 ^oC on a linear scale in the low shear rate region for DNA, DN-PNIPAm with low grafting density(b) and DNA-PNIPAm with high grafting density(c). The lines show the extrapolation to zero shear at 20 and 50 ^oC.(d) Yield stress σ_{yield} for all samples at different temperatures.

with typical time-temperature superstition for polymers: the system has faster relaxation at higher temperature, see the linear dependence of the crossover on temperature for DNA in 5.3d. Also for the DNA-PNIPAm samples, f_c initially display a positive shift with temperature with decreasing G' and G'', but at temperatures higher than 35 ^oC (for the low grafting density) and 40 ^oC (for the high grafting density), the declining of the storage G' and loss modulus G'' with temperature weakens and the crossover frequency shifts back to lower frequencies, meaning that the dynamics of the systems slow down due to PNIPAm grafting. The low grafting density sample almost becomes a critical gel for at 45 and 50 ^oC, as $G'(\omega)$ is always higher than $G''(\omega)$, while both curves are parallel, at least at the lower frequencies. The high grafting density

sample almost becomes a critical gel at 50 ^oC. As can be seen in Fig. 5.3d, at temperature lower than the LCST of PNIPAm, the crossover frequency of DNA is lower than for the low and the high grafting density sample, indicating that DNA with PNIPAm grafts show faster relaxation. The faster relaxation might be ascribed to the stiffening of DNA due to the grafting, resulting in a lower degree of entanglement. Interestingly, the low grafting density sample responds to temperature at lower temperature compared to that of the high grafting density sample, see the decrease of f_c in Fig. 5.3d. This might be caused by the steric hindrance of PNIPAm, which leads to weaker temperature response.

The flow curves, as constructed by the steady state stress protocol described in the previous chapters, shows similar trends as G' and G'', as can be seen in Fig. 5.4 . For DNA, the shear stress decreases with temperature due to faster dynamics at higher temperatures. There are two sloped plateaus on the flow curves, one from about 0.1 to 1 s^{-1} and the other from about 1 to 100 s^{-1} (see Fig.5.4a). For the DNA-PNIPAm brushlike polymer with low grafting density, the shear stress decreases with temperature and two sloped plateaus are observed at temperatures below the LCST of PNIPAm, while the stress decreases much slower with temperature and the shoulder in the flow curve becomes less pronounced and the flow curve becomes monotonic and a yield stress develops at higher temperatures, see Fig.5.4b. A similar trend is seen for the higher grafting density sample (Fig.5.4c). The shear thinning parameter m_{fc}, as described in Chapter 2, for the three samples are plotted against temperature. The m_{fc} for DNA is much lower than that of the grafted sampled, meaning that it shows strongest shear thinning. m_{fc} increases with grafting density, indicative of less shear thinning. Unlike the monotonous decrease of m_{fc} with temperature for pure DNA, m_{fc} for the PNIPAm grafted DNA first decreases and then increases with temperature, see Fig.5.4d. The first decrease can be attributed to stronger shear thinning due to faster relaxation rate at higher temperature. The increase might be due to weaker shear thinning due to increasing intermolecular attraction with temperature. Similar to the results shown in linear rheology, the attractive interaction sets in at lower temperature for the low grafting sample than that of high grafting density.

The stress σ in the low shear rate region is separately plotted on a linear scale in Fig. 5.5. The σ curve for pure DNA extrapolates to about 0 for all temperatures, see Fig. 5.5a. On the contrary, for DNA-PNIPAm with low grafting density, a yield stress develops of about 1 Pa at zero shear at 45 and 50 ^oC , see Fig.5.5b and d. DNA-PNIPAm with high grafting density shows a yield stress only at 50 ^oC, through much lower than that of the low grafting density sample. The observed yield stress for the DNA-PNIPAm samples complies with the gel formation described above. Clearly, the observation of yielding stress is cause by the so-called solid-to-fluid transition for these attractive polymer gels[119].

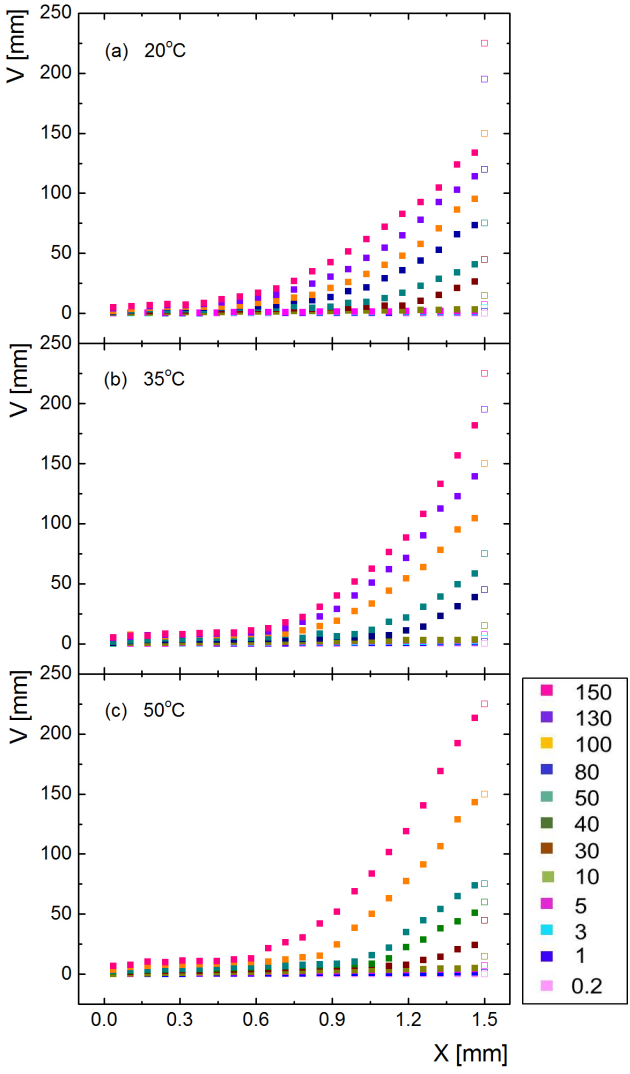

Figure 5.6: Velocity profiles at different shear rates for DNA at 20 ^oC(a), 35 ^oC(b), and 50 ^oC(c). The open points indicate the applied velocities for each shear rate. The applied shear rates in s^{-1} are indicated in the color bar.

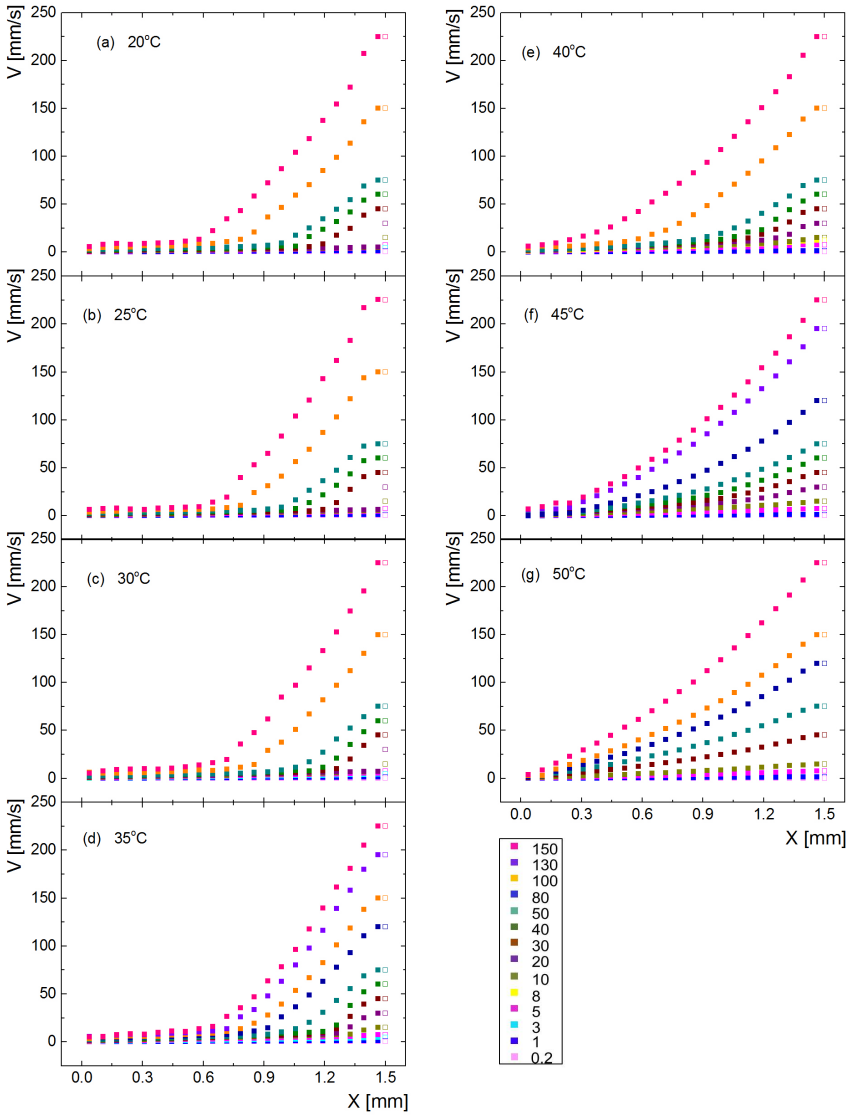

Figure 5.7: Velocity profiles at different shear rates for DNA-PNIPAm brush-like polymer with low PNIPAm grafting density at 20 ^oC(a), 25 ^oC(b), 30 ^oC(c), 35 ^oC(d), 40 ^oC(e), 45 ^oC(f), and 50 ^oC(g). The open points indicate applied velocities for each shear rate. The applied shear rates in s^{-1} are indicated in the color bar.

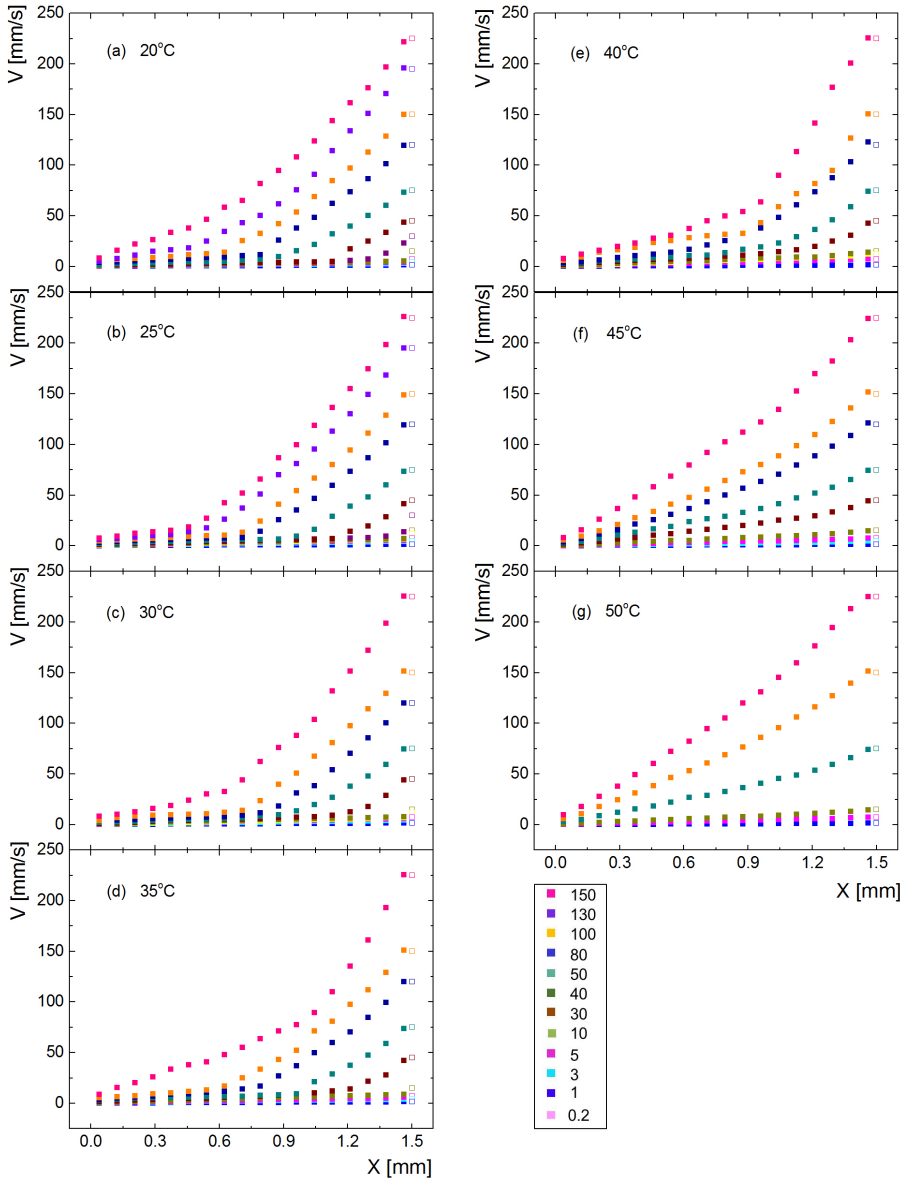

Figure 5.8: Velocity profiles at different shear rates for DNA-PNIPAm brush-like polymer with high PNIPAm grafting density at 20 ^oC(a), 25 ^oC(b), 30 ^oC(c), 35 ^oC(d), 40 ^oC(e), 45 ^oC(f), and 50 ^oC(g). The open points indicate applied velocities for each shear rate. The applied shear rates in s^{-1} are indicated in the color bar.

5.3.3 Velocity Profile and Analysis

The strong shear thinning indicated by the sloped plateau of the flow curve hints to the presence of shear banding. Indeed, as can be seen in Fig. 5.6a, strongly curved velocity profiles are observed at relatively high shear rates from 20 to 50 ^oC for DNA. Wall slip is also observed since the velocity close to the inner moving wall is smaller than the applied velocity. Wall slip is suppressed at higher temperatures. For DNA-PNIPAm with low grafting density, shear banding is also observed at relatively high shear rates from 20 to 35 ^oC, however, the velocity profiles are less curved at higher temperature, see Fig. 5.7. Similar effect are also observed for DNA-PNIPAm with high grafting density, see Fig. 5.8.

The relative slip velocity V_s/V_0 of the velocity profiles in Fig. 5.6-5.8, is given in Fig. 5.9a-c. Pure DNA shows considerably high wall slip between 20 to 50 ^oC, although wall slip decreases with increasing temperature. The relative slip velocity increases with the applied shear rate $\dot{\gamma}_{app}$, up to $\dot{\gamma}_{app} = 20s^{-1}$ where $V_s/V_0 \to 1$, which means that there is almost complete slip. Upon further increase of $\dot{\gamma}_{app}$, V_s/V_0 starts to decrease, see Fig. 5.9a. For the low grafting density sample, wall slip is only present for temperature under 35 ^oC and it is totally suppressed at higher temperatures. A similar effect is also seen for the high grafting density sample except for the fact that wall slip prevails up to 35 ^oC.

Similar to xanthan, most velocity profiles for entangled DNA and DNA-PNIPAm brushlike polymer in Fig 5.6-5.8 display a broad interface. Comparing the R^2 of the linear fit, piecewise linear fit, and the shear thinning fit, as introduced in chapter 2, we classify the velocity profiles into three categories, which are linear velocity profiles, curved velocity profiles and shear banded velocity profiles with sharp interface. For the velocity profiles with a sharp interface, when $R^2_{PWLF} > R^2_{STF}$, we calculate the fraction occupied by the higher shear rate band ε as defined in Chapter 2 and plot it versus the true shear rate, as shown in Fig. 5.10. All the data points for different temperatures fall on a master curve for all three samples through they don't correspond with each other for different samples. This is an indication that the velocity profiles are classic shear banded velocity profiles. More importantly, it shows that the grafting does not affect the flow instability in itself, but only tunes the competing processes.

The curved velocity profiles are still shear banded velocity profiles, since the lever rule can not cease only half way of the shear rate region. The second evidence is that the $m_{fc} - m$ in all the region remains high, while m should be equal to the m_{fc} when there is no shear banding, see Fig. 5.9d-f. Therefore, the curved velocity profiles are still shear-banded velocity profile only with a

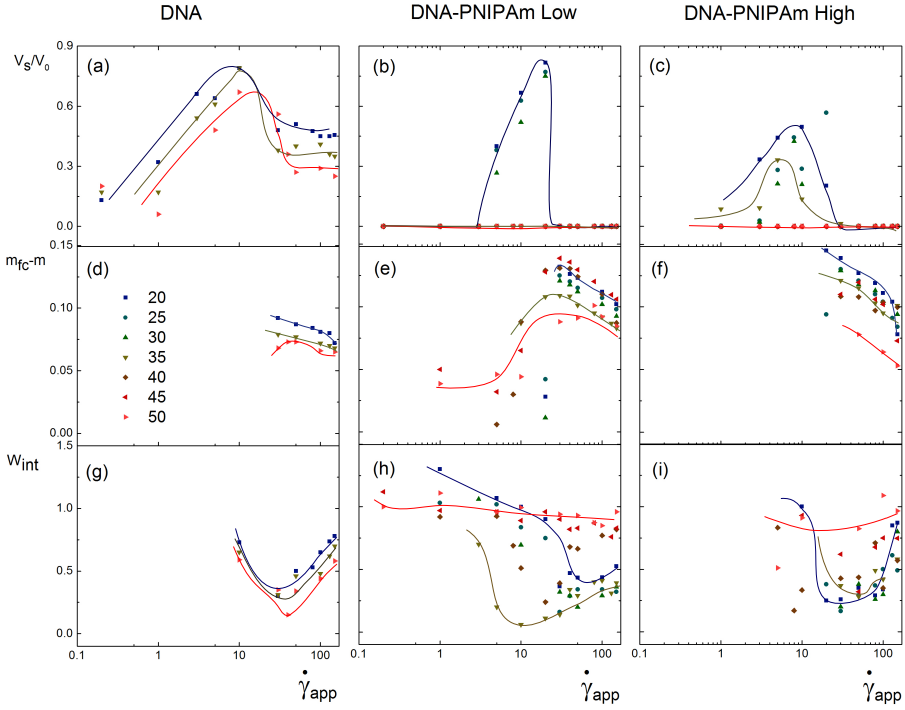

Figure 5.9: (a-c) Relative slip velocity V_s/V_0, (d-f) The difference of the exponents m_{fc} as determined from the flow curve and m as determined from the STF fit, and (g-i) the width of the shear-band interface at various temperature as indicated in the figure versus applied shear rate for 6mg/ml DNA, DNA-PNIPAm brush-like polymer with low PNIPAm grafting density, and DNA-PNIPAm brush-like polymer with high PNIPAm grafting density. The lines are guides-to-the-eye. Typical errors in the data points are ± 0.05 for $m_{fc} - m$.

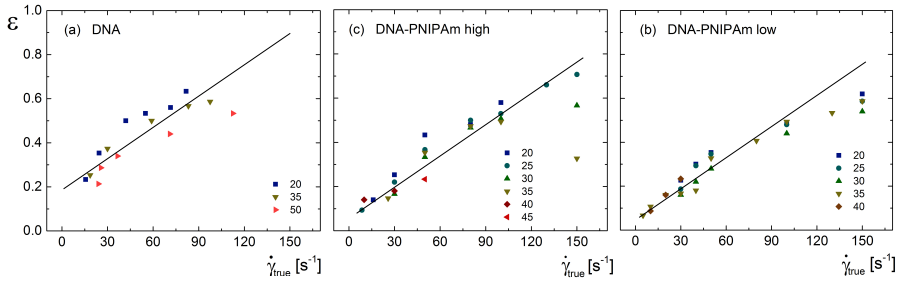

Figure 5.10: The lever-rule plot at various temperatures for 6mg/ml DNA (a), DNA-PNIPAm brush-like polymer with low PNIPAm grafting density (b), and DNA-PNIPAm brush-like polymer with high PNIPAm grafting density (c), where the fraction ϵ of the volume occupied by the high shear-rate band is plotted against the true shear rate, so after correction for the slip. The data points are based on the determination of ϵ from the velocity profiles with a sharp interface. The lines are guides to the eyes.

considerably large interface width. The interface width is given in Fig. 5.9g-i. The interface width first decreases with shear rate up to about $30s^{-1}$ and then increases with shear rate for all three samples. The reason is that the system first enters the shear banding region and then leaves the shear banding region with increasing shear rate. For DNA, Fig. 5.9g, the interface width decreases with temperature, indicating that DNA is more banded due to less wall slip at higher temperature. For DNA-PNIPAm systems, the interface width first decreases with temperature due to more shear banded with less wall slip and becomes less banded with temperature at higher temperature. The difference between the low and high grafting density sample is just that most banded velocity profiles for higher grafting density sample (check the lowest W_{int}) are observed at 40 ^oC rather than that of the low grafting density sample, which is at 35 ^oC.

All the information about the velocity profiles can be summarized in the diagram of states as shown in Fig. 5.11. First, the hatched region shows where we observe significant wall slip, which is almost the full diagram for DNA, while wall slip in DNA-PNIPAm brushlike polymers is largely is restricted to a small area at low temperatures. Second , the open symbols depict the points where sharp shear bands are observed, while the color coding indicates the curvature of the velocity profile. For pure DNA sharp banding only sets in 50 ^oC, while the region increases with increasing temperature. DNA-PNIPAm with low PNIPAm grafting density the sharp banding regions extends to lower shear rates only when the temperature is increased to 35 ^oC, since there is no wall slip, while at

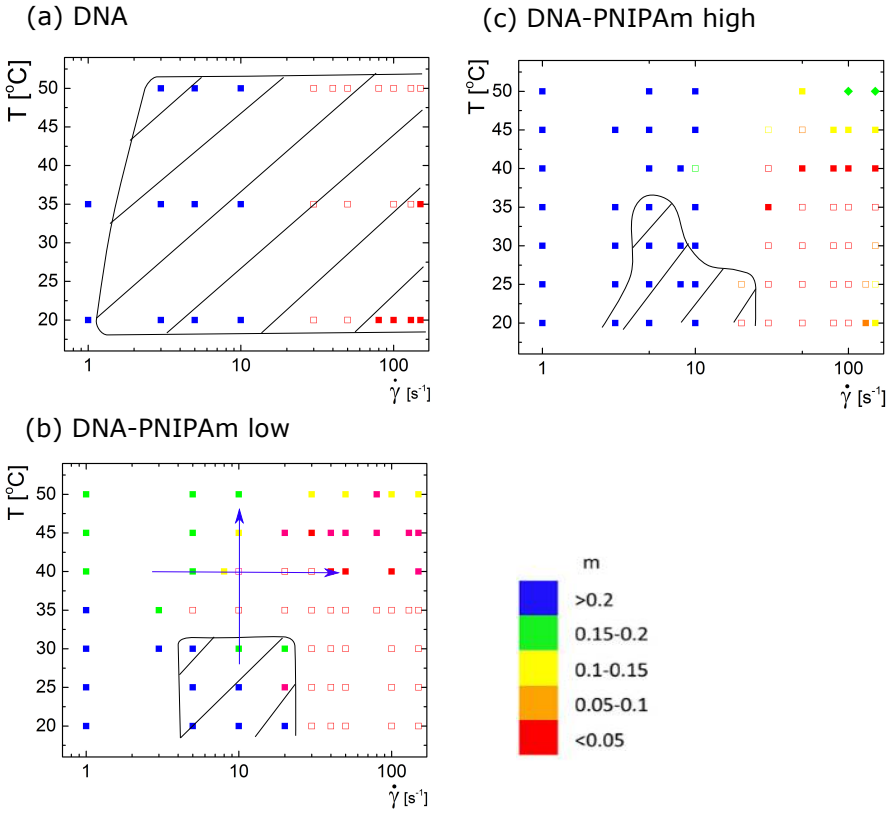

Figure 5.11: The diagram-of-states in the temperature T versus the applied shear-rate plane, where velocity profiles are classified depending on the shear-thinning parameter m which is indicated by the color bar. The open points refer to banded profiles with a sharp interface. The black solid curves indicate the region where more than 20% wall slip occurs. The arrows in (b) show the re-entrance of linear velocity profiles from shear banded velocity profiles

higher temperature the shear banding is largely suppressed. This means that there is a reentrant behavior by increasing the temperature at a fixed shear rate of $\dot{\gamma}_{app} = 10\ s^{-1}$, as indicated by the vertical arrow. At 40 ^oC there is also a reentrant behavior as now the region of shear banding is decreased, as indicated by the vertical arrow. Overall, the profiles are much more curved as indicated by the color coding. The high grafting density sample displays, surprisingly, intermediate behavior. The curvature behavior is similar to the pure DNA, the slip behavior and suppressed shear banding at high temperatures is similar to the low grafting density sample, though a bit shifted.

5.4 Discussion

The question addressed in this chapter is whether the intermolecular attraction between the polymers affects shear band formation in entangled polymeric systems in a similar manner as electrostatic repulsion. To this end we use a system for which we can change the interaction potential while keeping the effective diameter and the degree of entanglement fixed, which was not possible in the systems where the ionic strength was varied. We did this by using PNIPAm grafted DNA, which collapses at temperatures higher than its LCST, as was shown for infinite dilute PNIPAm-grafted DNA[117, 120]

We first showed that the temperature dependence of the blank, so of the pure DNA, is small. Shear banding does become somewhat more profound at higher temperature, which might be attributed to the slight decline of wall slip with temperature, see Fig. 5.9a, as wall slip competes with shear banding, see Chapter 4. Generally wall slip is related to the interfacial strength between the sample and the shear cell. The decline of wall slip with temperature might be caused by the dissociation of ions both for the glass and DNA depends on temperature, so as the interaction between the material and the glass wall. In addition, the viscosity of DNA solution drops, see Fig. 5.4a, which is mainly due to a drop of the viscosity of water with a factor of 2 from 20 ^{o} to 50 ^oC. In interpreting the results of the PNIPAm-DNA system, it is important to realize that the extend of the PNIPAm polymer grafted on the DNA is much smaller than the Debye double layer of the system. As such, it is surprising that the system gels to start with, but as we have seen, the gelation sets in at higher temperatures. This behavior was also observed for PNIPAm-grafted rod-like viruses[116]. As a result, the bonding after gelation is not very strong. On that note, it is interesting that the high grafting density system shows a weaker temperature response. Normally, higher grafting density or high molecular weight of PNIPAm would exhibit higher susceptibility to temperature [121]. Only when the grafting density becomes too high, the PNIPAm on DNA cannot

undergo conformation change at temperature higher than its LCST, due to steric repulsion of the crowded PNIPAm chains. This could be the case, considering the ratio of Pso-PNIPAm to DNA in the reaction. In addition, the crowded PNIPAm could also contribute to the intrinsic stiffness of the main chain as suggested by DNA-protein complex[122, 123, 124]. Further studies, for example using *in situ* atomic force microscopy, are needed to verify this assumption.

PNIPAm-DNA displays both an enhancement and suppression of shear banding, as can be seen in Fig. 5.11b and c. Shear banding is enhanced especially for the low grafting density for temperatures up to 35, see Fig. 5.11. This effect can be fully attributed to the suppressed wall slip at temperatures higher than the LCST of PNIPAm, see Fig.5.9a-c, as in this temperature range the hydrophobicity of PNIPAm enhances the sample-wall interfacial strength. Again, as wall slip competes with shear banding, suppression of wall slip leads to more profound shear banding. The effect of intermolecular attraction on shear banding should be evaluated when there is no wall slip(i.e.$\geqslant 35\ ^oC$).

Interestingly, the suppression of shear banding as testified in Fig. 5.11b, is accompanied with the formation of a gel, as testified in Fig. 5.3b. On a first glance this is surprising, as the modulus of the system increases and it obviously becomes more interconnected. It is known that gels of, for example, associative polymer networks can cause shear banding by itself[44]. So, in principle excess stress in sheared polymeric gels, as under study here, can relax via orientation as well as dissociation or rupture. We observe indeed that a yield stress builds up for high temperature. However, this is at the cost of a less pronounced stress plateau which is less pronounced, see Fig. 5.4. As a result, we observe in the flow profiles again a smooth broadening of the interface up to the point that the flow profile is nicely Newtonian, instead of more strong shear bands or even plug flow above LCST. We conclude that for $T < 35\ ^oC$ PNIPAm-DNA polymers disentangle and orient, while for for $T \geqslant 35\ ^oC$ they disentangle and collapse.

Thus, shear banding of DNA suspensions can be suppressed either by increasing intermolecular attraction, as described in this chapter, or by decreasing intermolecular repulsion as suggested in the previous chapters. The collapse of the backbone due to the attraction will cause a loss in alignment. Therefore, the fact that shear banding is suppressed at high temperatures supports the working hypothesis we posed in the previous chapters, namely that orientational ordering is required to form a sharp interface. In order to further investigate this suggestion, it would be interesting to perform *in situ* confocal microscopy measurements in combination with a counter-rotating cone-plate shear cell, as in Ref. [125], or time-resolved measurements that probe orientation such as neutron scattering and birefringence. In addition, for longer PNIPAm polymers or higher ionic strength, rapture could kick in, as the yield stress will increase.

5.5 Summary

We show in this chapter that shear banding and wall slip can be tunned by grafting an attractive PNIPAm brush to DNA. It causes a reentrant shear banding behavior both in temperature and in shear rate. Approaching the LCST, the DNA-PNIPAm becomes hydrophobic and enhanced the interaction between the wall and the bulk material, thus suppressing wall slip and enhancing shear banding, as both processes compete. However, at higher temperatures, shear banding is largely suppressed, via a smooth widening of the interface W_{int}, until a Newtonian flow profile is recovered. As the high temperature will cause a collapse of the disentangled backbone, the orientation will be lost. These findings therefore support the working hypothesis we posed in chapter 4, namely that orientation is a prerequisite for the formation of sharp interfaces. In addition, the higher grafting density of PNIPAm shows a weaker temperature response as compared to low grafting density sample maybe due to steric hindrance.

Chapter 6

Conclusions

We have studied the flow behaviors of entangled xanthan, DNA and DNA-PNIPAm brushlike polymer using heterodyne dynamic light scattering. We show in this thesis that shear banding and wall slip in entangled semi-flexible polyelectrolytes such as xanthan and DNA can be finely tuned by intermolecular interactions such as electrostatic repulsions or intermolecular attraction. In the following paragraphs, our crucial findings in chapter 2-5, will be summarized.

In Chapter 2, we introduced our experimental set-up to measure velocity profiles, as well as our approach to analyzing these profiles. Here we take into account that there will always be curvature in the velocity profile when the sample is shear thinning, given the curvature of the geometry. Hence we developed an analysis method that can be used to distinguish between non-linear curved profiles due to shear thinning and actual shear banding. In order to do so we introduced a new definition of the interface width W_{int}.

In chapter 3, we presented the velocity profiles of entangled xanthan at different concentrations and ionic strengths. We showed that shear banding can be found when the concentration is sufficiently high, which is connected with the formation of a stress plateau at the high concentration. At this high concentration shear banding with sharp interfaces was observed only at low ionic strength, while it is suppressed at higher ionic strength. This is a surprising finding as the shear thinning factor is not affected by ionic strength. We showed that the suppression of the shear banding occurs via a broadening of the interface. We employed a new analysis methods, which allows to differentiate between the effect that the inhomogeneous stress distribution throughout the co-cylinder shear cell has on the velocity profile for shear thinning fluids, and the broadening of the interface itself. These two effects have led to confusion in

the past concerning the issue of shear banding of polymeric systems. There is a direct relation between flow alignment and the formation of shear bands with a sharp interface, as the broadening of the interface is connected with a strong decrease of flow birefringence. Interpreting the interplay between alignment and shear banding, one should consider that the stiffness and the interaction potential of xanthan both strongly depend on the ionic strength. At high ionic strength, when xanthan is flexible and neutral, this results in a very polymer-like system. Thus the behavior of xanthan may aid to resolve the ongoing dispute concerning shear-banding of highly entangled polymeric systems. However, for a full understanding we need to compare the flow behavior of xanthan with the flow behavior of other systems which are better controlled and with intrinsic stiffness, such that both the effects of stiffness and interaction have on shear band formation can be isolated. To this end we choose DNA.

In chapter 4, the effect of ionic strength on wall slip and shear banding of entangled DNA was systematically studied along with birefringence measurements. When the salt concentration is as low as 0.01 M, there is well defined shear banding along with considerable wall slip , accompanied by high flow-induced birefringence intensity and birefringent patterns. When the salt concentration is 1 M, where the system is the most entangled or polymer-like, almost no shear banding and little wall slip occurs, accompanied by disappearance of birefringent patterns. These findings suggest that in principle stress can be released purely by disentanglement, but that disentanglement combined with sustained orientational ordering is required to form sharp interfaces. In the proximity of a thermodynamic isotropic-nematic phase transition a para-nematic phase is readily formed, thus also the interface between bands. Therefore, shear banding is not a general property for strongly shear thinning polymeric systems, but subtly depends on the molecular properties of the system. It can completely disappear via the widening of the interface, when there is no induced orientational order in the system. We will try to tune this by inducing a mechanism that can cause a collapse of the disentangled polymer.

In chapter 5, we showed that shear banding and wall slip can be tunned by grafting an attractive PNIPAm brush to DNA. It causes a reentrant shear banding behavior both in temperature and in shear rate. Approaching the LCST, the DNA-PNIPAm becomes hydrophobic and enhanced the interaction between the wall and the bulk material, thus suppressing wall slip and enhancing shear banding, as both processes compete. However, at higher temperatures, shear banding is largely suppressed, via a smooth widening of the interface W_{int}, until a Newtonian flow profile is recovered. As the high temperature will cause a collapse of the disentangled backbone, the orientation will be lost. These findings therefore support the working hypothesis we posed in chapter 4, namely that orientation is a prerequisite for the formation of sharp interfaces. In addition,

the higher grafting density of PNIPAm shows a weaker temperature response as compared to low grafting density sample maybe due to steric hindrance.

We will now try to put our findings in a broader perspective. To start with, we observed for all systems that the tuning that we performed for each system, did not influence the flow curves, but did have a pronounced effect on the shear banding behavior. This means that all systems have a very similar underlying constitutive flow curve, including a stress overshoot. There are different pathways in which the excess stress can be released, which clearly depend on the molecular properties. Stress can be released via 1) by disentanglement, and 2) by orientation of the Kuhn segments. The question is how relaxation mechanism influences the flow profile. We observe in all cases that orientation and sharp interfaces are strongly connected. Note here, that similar findings were also done for worm-like micellar systems where the ionic strength was altered, affecting both the flexibility and the contour length[97]. This suggest that orientation stabilizes the shear band interface. This is most strongly supported by our observation on PNIPAm-DNA, where shear banding could be fully extinguished by inducing a collapse of the backbone and therefore of the orientation, while keeping the degree of entanglement and effective volume fraction unaffected. Here the shear stress could not compete with the force that drives the collapse of the backbone. In order to sustain orientation after disentanglement it helps when the system is close to its equilibrium I-N transition, as then a shear induced para-nematic phase is readily formed. However, there could be other mechanisms acting to sustain alignment [108].

This conclusion suggests that neutral flexible polymers cannot form shear bands, which is, however, not the case. We showed by introducing a new analysis method, that curved velocity profiles could hint to shear banding, when the shear thinning factor as obtained from the velocity profile is smaller than the shear thinning factor as obtained from the flow curve. Thus, the only problem for those systems is that the interface becomes to big for the gap. Thus, it would be a challenging, and sample consuming, to perform exactly the same experiment, but then in a cell with the same curvature (so the same ratio R_1/R_2), but with much bigger gap. This means that experiments should be performed in Couette cells with a diameter of at least about $R_1 = 20\ cm$, which requires a lot of sample.

In order to understand the much less pronounced velocity profiles for flexible polymers, one should ask the question why the interface W widens when disentanglement is the only release mechanism, as is clearly the case for flexible polymers. In principle, it can be understood when considering what happens at the moment the polymer looses a entanglement point by means of convection. Suddenly the shear rate should not be scaled anymore by the reptation time but rather by the Rouse time, in order to sustain its orientation. This is the

reason why orientation is lost. For flexible polymers this requires very high shear rates. Still, shear bands could coexist, where a shear band with low degree of entanglement co-exists with a band with a high degree of entanglements. This is clearly not the case. A way to incorporate this effect into the present theory is by considering the convective constraint release theory as used by Adams and Olmsted[7]. In principle both the Rouse and the reptation time are included in this theory, but the parameter that drives the shear band formation, namely the stress diffusivity D[6], or in terms of the curvature viscosity[5], should be connected to the tendency of polymers to collapse.

Further neutron scattering study is undergoing in the lab clarify whether the high shear rate band in DNA is a para-nematic phase. Furthermore, the effect of the polymer stiffness and intermolecular interactions are intertwined in all cases. In that respect our observations are still not conclusive. In order disentangle the different effects, simulations where different parameters can be separately tuned should be conducted.

Whatever the exact mechanism of shear banding might be, we do show that flow instabilities can be subtly tuned in different ways and we observed intriguing phenomena like the reentrant behavior.

Bibliography

[1] P. G. de Gennes. Soft matter (nobel lecture). *Angew. Chem. Int. Ed.*, 31(7):842–845, 1992.

[2] C. J. S. Petrie and M. M. Denn. Instabilities in polymer processing. *AICHE J.*, 22(2):209–236, 1976.

[3] D. G. Baird and D. I. Collias. *Polymer processing: principles and design.* John Wiley & Sons, 2014.

[4] J. F. Agassant, P. Avenas, P. J. Carreau, B. Vergnes, and M. Vincent. *Polymer processing: principles and modeling.* Carl Hanser Verlag GmbH Co KG, 2017.

[5] J. K. G. Dhont. A constitutive relation describing the shear-banding transition. *Phys. Rev. E*, 60(4):4534–4544, 1999.

[6] P. D. Olmsted, O. Radulescu, and C. Y. D. Lu. Johnson–segalman model with a diffusion term in cylindrical couette flow. *J. Rheol.*, 44(2):257–275, 2000.

[7] J. M. Adams, S. M. Fielding, and P. D. Olmsted. Transient shear banding in entangled polymers: A study using the rolie-poly model. *J. Rheol.*, 55(5):1007–1032, 2011.

[8] S. M. Fielding. Triggers and signatures of shear banding in steady and time-dependent flows. *J. Rheol.*, 60(5):821–834, 2016.

[9] S. M. Fielding and P. D. Olmsted. Flow phase diagrams for concentration-coupled shear banding. *Eur. Phys. J. E*, 11(1):65–83, 2003.

[10] M. Cromer, M. C. Villet, G. H. Fredrickson, and L. G. Leal. Shear banding in polymer solutions. *Phys. Fluids*, 25(5):051703, 2013.

[11] P. D. Olmsted and C. Y. D. Lu. Phase coexistence of complex fluids in shear flow. *Faraday Disc.*, 112:183–194, 1999.

[12] C. Y. D. Lu, P. D. Olmsted, and R. C. Ball. Effects of nonlocal stress on the determination of shear banding flow. *Phys. Rev. Lett.*, 84(4):642, 2000.

[13] N. A. Spenley, X. F. Yuan, and M. E. Cates. Nonmonotonic constitutive laws and the formation of shear-banded flows. *JPhy2*, 6(4):551–571, 1996.

[14] O. Radulescu, P. D. Olmsted, J. P. Decruppe, S. Lerouge, J. F. Berret, and G. Porte. Time scales in shear banding of wormlike micelles. *Europhys. Lett.*, 62(2):230, 2003.

[15] X. F. Yuan. Dynamics of a mechanical interface in shear-banded flow. *Europhys. Lett.*, 46(4):542, 1999.

[16] A. W. El-Kareh and L. G. Leal. Existence of solutions for all deborah numbers for a non-newtonian model modified to include diffusion. *J. Nonnewton. Fluid. Mech.*, 33(3):257–287, 1989.

[17] J. F. Berret, G. Porte, and J. P. Decruppe. Inhomogeneous shear flows of wormlike micelles: A master dynamic phase diagram. *Phys. Rev. E*, 55(2):1668–1676, 1997.

[18] M. M. Britton, R. W. Mair, R. K. Lambert, and P. T. Callaghan. Transition to shear banding in pipe and couette flow of wormlike micellar solutions. *J. Rheol.*, 43(4):897–909, 1999.

[19] J. B. Salmon, L. Bécu, S. Manneville, and A. Colin. Towards local rheology of emulsions under couette flow using dynamic light scattering. *Eur. Phys. J. E*, 10(3):209–221, 2003.

[20] M. W. Liberatore, F. Nettesheim, N. J. Wagner, and L. Porcar. Spatially resolved small-angle neutron scattering in the 1-2 plane: A study of shear-induced phase-separating wormlike micelles. *Phys. Rev. E*, 73(2):020504, 2006.

[21] E. Cappelaere, J. F. Berret, J. P. Decruppe, R. Cressely, and P. Lindner. Rheology, birefringence, and small-angle neutron scattering in a charged micellar system: Evidence of a shear-induced phase transition. *Phys. Rev. E*, 56(2):1869, 1997.

[22] G. Porte, J. F. Berret, and J. L. Harden. Inhomogeneous flows of complex fluids: Mechanical instability versus non-equilibrium phase transition. *JPhy2*, 7(3):459–472, 1997.

[23] A. Van Den Noort and W. J. Briels. Coarse-grained simulations of elongational viscosities, superposition rheology and shear banding in model core–shell systems. *Macromol. Theory Simul.*, 16(8):742–754, 2007.

[24] D. Bonn, J. Meunier, O. Greffier, A. Al-Kahwaji, and H. Kellay. Bistability in non-newtonian flow: rheology of lyotropic liquid crystals. *Phys. Rev. E*, 58(2):2115, 1998.

[25] J. B. Salmon, S. Manneville, and A. Colin. Shear banding in a lyotropic lamellar phase. i. time-averaged velocity profiles. *Phys. Rev. E*, 68(5):051503, 2003.

[26] J. B. Salmon, S. Manneville, and A. Colin. Shear banding in a lyotropic lamellar phase. ii. temporal fluctuations. *Phys. Rev. E*, 68(5):051504, 2003.

[27] L. B. Chen, C. F. Zukoski, B. J. Ackerson, H. J. M. Hanley, G. C. Straty, J. Barker, and C. J. Glinka. Structural changes and orientaional order in a sheared colloidal suspension. *Phys. Rev. Lett.*, 69(4):688, 1992.

[28] A. Imhof, A. Van Blaaderen, and J. K. G. Dhont. Shear melting of colloidal crystals of charged spheres studied with rheology and polarizing microscopy. *Langmuir*, 10(10):3477–3484, 1994.

[29] T. Palberg and M. Würth. Multiphase coexistence and non-linear rheology of colloidal. dispersions as observed in a model capillary viscosimeter. *JPhy1*, 6(2):237–244, 1996.

[30] E. Eiser, F. Molino, G. Porte, and O. Diat. Nonhomogeneous textures and banded flow in a soft cubic phase under shear. *Phys. Rev. E*, 61(6):6759, 2000.

[31] E. Eiser, F. Molino, G. Porte, and X. Pithon. Flow in micellar cubic crystals. *Rheol. Acta*, 39(3):201–208, 2000.

[32] H. Jin, K. Kang, K. H. Ahn, and J. K. G. Dhont. Flow instability due to coupling of shear-gradients with concentration: non-uniform flow of (hard-sphere) glasses. *Soft matter*, 10(47):9470 – 9485, 2014.

[33] R. Besseling, L. Isa, P. Ballesta, G. Petekidis, M. E. Cates, and W. C. K. Poon. Shear banding and flow-concentration coupling in colloidal glasses. *Phys. Rev. Lett.*, 105(26):268301, 2010.

[34] M. Cromer, G. H. Fredrickson, and L. G. Leal. A study of shear banding in polymer solutions. *Phys. Fluids*, 26(6):063101, 2014.

[35] J. P. Decruppe, R. Cressely, R. Makhloufi, and E. Cappelaere. Flow birefringence experiments showing a shear-banding structure in a ctab solution. *Colloid. Polym. Sci.*, 273(4):346–351, 1995.

[36] J. F. Berret, D. C. Roux, and P. Lindner. Structure and rheology of concentrated wormlike micelles at the shear-induced isotropic-to-nematic transition. *Eur. Phys. J. B*, 5(1):67–77, 1998.

[37] Y. T. Hu and A. Lips. Kinetics and mechanism of shear banding in an entangled micellar solution. *J. Rheol.*, 49(5):1001–1027, 2005.

[38] E. Miller and J. Rothstein. Transient evolution of shear-banding wormlike micellar solutions. *J. Nonnewton. Fluid. Mech.*, 143(1):15, 2007.

[39] B. S. Douglass, R. H. Colby, L. A. Madsen, and P. T. Callaghan. Rheo-nmr of wormlike micelles formed from nonionic pluronic surfactants. *Macromolecules*, 41(3):804–814, 2008.

[40] N. A. Spenley, M. E. Cates, and T. C. B. McLeish. Nonlinear rheology of wormlike micelles. *Phys. Rev. Lett.*, 71(6):939, 1993.

[41] P. A. Vasquez, G. H. McKinley, and L. P. Cook. A network scission model for wormlike micellar solutions: I. model formulation and viscometric flow predictions. *J. Nonnewton. Fluid. Mech.*, 144(2-3):122–139, 2007.

[42] J. van der Gucht, M. Lemmers, W. Knoben, N. A. Besseling, and M. P. Lettinga. Multiple shear-banding transitions in a supramolecular polymer solution. *Phys. Rev. Lett.*, 97(10):108301, 2006.

[43] E. Michel, J. Appell, F. Molino, J. Kieffer, and G. Porte. Unstable flow and nonmonotonic flow curves of transient networks. *J. Rheol.*, 45(6):1465–1477, 2001.

[44] J. Sprakel, E. Spruijt, M. A. Cohen Stuart, N. A. M. Besseling, M. P. Lettinga, and J. van der Gucht. Shear banding and rheochaos in associative polymer networks. *Soft Matter*, 4(8):1696–1705, 2008.

[45] C. Pujolle-Robic, P. D. Olmsted, and L. Noirez. Transient and stationary flow behaviour of side chain liquid-crystalline polymers: Evidence of a shear-induced isotropic-to-nematic phase transition. *Europhys. Lett.*, 59(3):364, 2002.

[46] L. Ramos, F. Molino, and G. Porte. Shear melting in lyotropic hexagonal phases. *Langmuir*, 16(14):5846–5848, 2000.

[47] I. Kunita, K. Sato, Y. Tanaka, Y. Takikawa, H. Orihara, and T. Nakagaki. Shear banding in an f-actin solution. *Phy Rev Lett*, 109(24):248303, 2012.

[48] B. Lonetti, J. Kohlbrecher, L. Willner, J. K. G. Dhont, and M. P. Lettinga. Dynamic response of block copolymer wormlike micelles to shear flow. *J. Phys. Condens. Matter*, 20(40):404207–404218, 2008.

[49] E. V. Menezes and W. W. Graessley. Nonlinear rheological behavior of polymer systems for several shear-flow histories. *J Polym Sci B Polym Phys.*, 20(10):1817–1833, 1982.

[50] Y. T. Hu, C. Palla, and A. Lips. Comparison between shear banding and shear thinning in entangled micellar solutions. *J. Rheol.*, 52(2):379–400, 2008.

[51] Y. W. Inn, K. F. Wissbrun, and M. M. Denn. Effect of edge fracture on constant torque rheometry of entangled polymer solutions. *Macromolecules*, 38(22):9385–9388, 2005.

[52] C. P. Sui and G. B. McKenna. Instability of entangled polymers in cone and plate rheometry. *Rheol. Acta*, 46(6):877–888, 2007.

[53] T. Schweizer. Shear banding during nonlinear creep with a solution of monodisperse polystyrene. *Rheol. Acta*, 46(5):629–637, 2007.

[54] P. Tapadia and S. Q. Wang. Direct visualization of continuous simple shear in non-newtonian polymeric fluids. *Phys. Rev. Lett.*, 96(1):016001, 2006.

[55] P. Tapadia, S. Ravindranath, and S. Q. Wang. Banding in entangled polymer fluids under oscillatory shearing. *Phys. Rev. Lett.*, 96(19):196001, 2006.

[56] Y. T. Hu, L. Wilen, A. Philips, and A. Lips. Is the constitutive relation for entangled polymers monotonic? *J. Rheol.*, 51(2):275–295, 2007.

[57] P. E. Boukany, S. Q. Wang, S. Ravindranath, and L. J. Lee. Shear banding in entangled polymers in the micron scale gap: a confocal-rheoscopic study. *Soft Matter*, 11(41):8058–8068, 2015.

[58] P. E. Boukany, Y. T. Hu, and S. Q. Wang. Observations of wall slip and shear banding in an entangled dna solution. *Macromolecules*, 41(7):2644–2650, 2008.

[59] P. E. Boukany and S. Q. Wang. Shear banding or not in entangled dna solutions depending on the level of entanglement. *J. Rheol.*, 53(1):73–83, 2009.

[60] P. E. Boukany and S. Q. Wang. Exploring the transition from wall slip to bulk shearing banding in well-entangled dna solutions. *Soft Matter*, 5(4):780–789, 2009.

[61] P. E. Boukany and S. Q. Wang. Shear banding or not in entangled dna solutions. *Macromolecules*, 43(17):6950–6952, 2010.

[62] K. A. Hayes, M. R. Buckley, I. Cohen, and L. A. Archer. High resolution shear profile measurements in entangled polymers. *Phys. Rev. Lett.*, 101(21):218301, 2008.

[63] K. A. Hayes, M. R. Buckley, H. B. Qi, I. Cohen, and L. A. Archer. Constitutive curve and velocity profile in entangled polymers during start-up of steady shear flow. *Macromolecules*, 43(9):4412–4417, 2010.

[64] Y. F. Li, M. Hu, G. B. McKenna, C. J. Dimitriou, G. H. McKinley, R. M. Mick, D. C. Venerus, and L. A. Archer. Flow field visualization of entangled polybutadiene solutions under nonlinear viscoelastic flow conditions. *J. Rheol.*, 57(5):1411–1428, 2013.

[65] Y. F. Li and G. B. McKenna. Startup shear of a highly entangled polystyrene solution deep into the nonlinear viscoelastic regime. *Rheol. Acta*, 54(9-10):771–777, 2015.

[66] S. Manneville, A. Colin, G. Waton, and F. Schosseler. Wall slip, shear banding, and instability in the flow of a triblock copolymer micellar solution. *Phys. Rev. E*, 75(6):061502, 2007.

[67] M. P. Lettinga and S. Manneville. Competition between shear banding and wall slip in wormlike micelles. *Phys. Rev. Lett.*, 103(24):248302, 2009.

[68] P. T. Callaghan and A. M. Gil. Rheo-nmr of semidilute polyacrylamide in water. *Macromolecules*, 33(11):4116–4124, 2000.

[69] M. M. Britton and P. T. Callaghan. Nuclear magnetic resonance visualization of anomalous flow in cone-and-plate rheometry. *J. Rheol.*, 41(6):1365–1386, 1997.

[70] A. Gurung, J. W. Haverkort, S. Drost, B. Norder, J. Westerweel, and C. Poelma. Ultrasound image velocimetry for rheological measurements. *MeScT*, 27(9):094008, 2016.

[71] M.M. Britton, P.T. Callaghan, M. L. Kilfoil, R. W. Mair, and K. M. Owens. Nmr velocimetry and spectroscopy at microscopic resolution in small rheometric devices. *Appl. Magn. Reson.*, 15(3-4):287–301, 1998.

[72] S. Jaradat, M. Harvey, and T. A. Waigh. Shear-banding in polyacrylamide solutions revealed via optical coherence tomography velocimetry. *Soft Matter*, 8(46):11677, 2012.

[73] A. V. Malm, A. W. Harrison, and T. A. Waigh. Optical coherence tomography velocimetry of colloidal suspensions. *Soft matter*, 10(41):8210–8215, 2014.

[74] J. Delgado, H. Kriegs, and R. Castillo. Flow velocity profiles and shear banding onset in a semidilute wormlike micellar system under couette flow. *J. Phys. Chem. B*, 113(47):15485–15494, 2009.

[75] Y. F. Li, M. Hu, G. B. McKenna, C. J. Dimitriou, G. H. McKinley, R. M. Mick, D. C. Venerus, and L. A. Archer. Response to: Sufficiently entangled polymers do show shear strain localization at high enough weissenberg numbers". *J. Rheol.*, 58(4):1071–1082, 2014.

[76] E. J. Hemingway and S. M. Fielding. Edge-induced shear banding in entangled polymeric fluids. *Phys. Rev. Lett.*, 120:138002, 2018.

[77] P. Cheng, M. C. Burroughs, L. G. Leal, and M. E. Helgeson. Distinguishing shear banding from shear thinning in flows with a shear stress gradient. *Rheol. Acta*, 56(12):1007–1032, 2017.

[78] A. Brunet, C. Tardin, L. Salomé, P. Rousseau, N. Destainville, and M. Manghi. Dependence of dna persistence length on ionic strength of solutions with monovalent and divalent salts: A joint theory–experiment study. *Macromolecules*, 48(11):3641–3652, 2015.

[79] T. A. Camesano and K. J. Wilkinson. Single molecule study of xanthan conformation using atomic force microscopy. *Biomacromolecules*, 2(4):1184–1191, 2001.

[80] Y. T. Hu, C. Palla, and A. Lips. Role of electrostatic interactions in shear banding of entangled dna solutions. *Macromolecules*, 41(18):6618–6620, 2008.

[81] H. Tang, T. Kochetkova, H. Kriegs, J. K. G. Dhont, and M. P. Lettinga. Shear-banding in entangled xanthan solutions: tunable transition from sharp to broad shear-band interfaces. *Soft Matter*, 14:826–836, 2018.

[82] W. E. Rochefort and S. Middleman. Rheology of xanthan gum: Salt, temperature, and strain effects in oscillatory and steady shear experiments. *J. Rheol.*, 31(4):337–369, 1987.

[83] H. C. Lee and D. A. Brant. Rheology of concentrated isotropic and anisotropic xanthan solutions. 2. a semiflexible wormlike intermediate molecular weight sample. *Macromolecules*, 35(6):2223–2234, 2002.

[84] H. C. Lee and D. A. Brant. Rheology of concentrated isotropic and anisotropic xanthan solutions. 1. a rodlike low molecular weight sample. *Macromolecules*, 35(6):2212–2222, 2002.

[85] N. B. Wyatt and M. W. Liberatore. Rheology and viscosity scaling of the polyelectrolyte xanthan gum. *J. Appl. Polym. Sci.*, 114(6):4076–4084, 2009.

[86] L. Xu, G. Xu, T. Liu, Y. Chen, and H. Gong. The comparison of rheological properties of aqueous welan gum and xanthan gum solutions. *Carbohydr. Polym.*, 92(1):516–522, 2013.

[87] L. Zhong, M. Oostrom, M. J. Truex, V. R. Vermeul, and J. E. Szecsody. Rheological behavior of xanthan gum solution related to shear thinning fluid delivery for subsurface remediation. *J. Hazard. Mater.*, 244-245:10, 2013.

[88] S. Dumitriu. *Polysaccharides: Structural Diversity and Functional Versatility*. Taylor & Francis, 2nd edition, 2004.

[89] R. S. Graham, E. P. Henry, and P. D. Olmsted. Comment on "new experiments for improved theoretical description of nonlinear rheology of entangled polymers". *Macromolecules*, 46(24):9849–9854, 2013.

[90] G. Marrucci. Dynamics of entanglements: A nonlinear model consistent with the cox-merz rule. *J. Nonnewton. Fluid. Mech.*, 62(2):279–289, 1996.

[91] G. Ianniruberto and G. Marrucci. A simple constitutive equation for entangled polymers with chain stretch. *J. Rheol.*, 45(6):1305–1318, 2001.

[92] S. Q. Wang, Y. Y. Wang, S. W. Cheng, X. Li, X. Y. Zhu, and H. Sun. New experiments for improved theoretical description of nonlinear rheology of entangled polymers. *Macromolecules*, 46(8):3147–3159, 2013.

[93] S. A. Rogers, D. Vlassopoulos, and P. T. Callaghan. Aging, yielding, and shear banding in soft colloidal glasses. *Phys. Rev. Lett.*, 100(12):128304, 2008.

[94] F. Snijkers, R. Pasquino, P. D. Olmsted, and D. Vlassopoulos. Perspectives on the viscoelasticity and flow behavior of entangled linear and branched polymers. *J. Phys.: Condens. Matter*, 27(47):473002, 2015.

[95] D. Risica, A. Barbetta, L. Vischetti, C. Cametti, and M. Dentini. Rheological properties of guar and its methyl, hydroxypropyl and hydroxypropyl-methyl derivatives in semidilute and concentrated aqueous solutions. *Poly*, 51(9):1972–1982, 2010.

[96] A. V. Malm and T. A. Waigh. Elastic turbulence in entangled semi-dilute dna solutions measured with optical coherence tomography velocimetry. *Sci. Rep.*, 7(1):1186, 2017.

[97] D. Gaudino, R. Pasquino, H. Kriegs, N. Szekely, W. Pyckhout-Hintzen, M. P. Lettinga, and N. Grizzuti. Effect of the salt-induced micellar microstructure on the nonlinear shear flow behavior of ionic cetylpyridinium chloride surfactant solutions. *Phys. Rev. E*, 95(3):032603, 2017.

[98] S. Lerouge, M. Argentina, and J. P. Decruppe. Interface instability in shear-banding flow. *Phys. Rev. Lett.*, 96(8):088301, 2006.

[99] M. A. Fardin, B. Lasne, O. Cardoso, G. Grégoire, M. Argentina, J. P. Decruppe, and S. Lerouge. Taylor-like vortices in shear-banding flow of giant micelles. *Phys. Rev. Lett.*, 103(2):028302, 2009.

[100] M. A. Fardin and S. Lerouge. Instabilities in wormlike micelle systems. *Eur. Phys. J. E*, 35(9):91, 2012.

[101] M. A. Fardin, L. Casanellas, B. Saint-Michel, S. Manneville, and S. Lerouge. Shear-banding in wormlike micelles: Beware of elastic instabilities. *J. Rheol.*, 60(5):917–926, 2016.

[102] P. D. Olmsted and C. Y. D. Lu. Phase separation of rigid-rod suspensions in shear flow. *Phys. Rev. E*, 60(4):4397–4415, 1999.

[103] M. A. Valdez, L. Yeomans, F. Montes, H. Acuna, and A. Ayala. Influence of temperature on the slip velocity of semidilute xanthan gum solutions. *Rheol. Acta*, 34(5):474–482, 1995.

[104] S. J. Gibbs, K. L. James, L. D. Hall, D. E. Haycock, W. J. Frith, and S. Ablett. Rheometry and detection of apparent wall slip for poiseuille flow of polymer solutions and particulate dispersions by nuclear magnetic resonance velocimetry. *J. Rheol.*, 40(3):425–440, 1996.

[105] D. R. Tree, A. Muralidhar, P. S. Doyle, and K. D. Dorfman. Is dna a good model polymer? *Macromolecules*, 46(20), 2013.

[106] H. Orin and P. E. Boukany. Microscopic origin of wall slip during flow of an entangled dna solution in microfluidics: Flow induced chain stretching versus chain desorption. *Biomicrofluidics*, 11(4):044118, 2017.

[107] P. E. Boukany, O. Hemminger, S. Q. Wang, and L. J. Lee. Molecular imaging of slip in entangled dna solution. *Phys. Rev. Lett.*, 105(2):027802, 2010.

[108] L. M. Bravo-Anaya, E. R. Macías, J. H. Pérez-López, H. Galliard, D. C. D. Roux, G. Landazuri, F. Carvajal Ramos, M. Rinaudo, F. Pignon, and J. F. A. Soltero. Supramolecular organization in calf-thymus dna solutions under flow in dependence with dna concentration. *Macromolecules*, 50(20):8245–8257, 2017.

[109] B. J. Wood, R. N. Lamb, and C. L. Raston. Static sims study of hydroxylation of low-surface-area silica. *Surf. Interface Anal.*, 23(10):680–688, 1995.

[110] S. Q. Wang, S. Ravindranath, and P. E. Boukany. Homogeneous shear, wall slip, and shear banding of entangled polymeric liquids in simple-shear rheometry: A roadmap of nonlinear rheology. *Macromolecules*, 44(2):183–190, 2011.

[111] E. Fischer and P. T. Callaghan. Is a birefringence band a shear band? *Europhys. Lett.*, 50(6):803, 2000.

[112] K. Merchant and R. L. Rill. Dna length and concentration dependencies of anisotropic phase transitions of dna solutions. *Biophys. J.*, 73(6):3154–3163, 1997.

[113] C. G. Baumann, S. B. Smith, V. A. Bloomfield, and C. Bustamante. Ionic effects on the elasticity of single dna molecules. *Proceedings of the National Academy of Sciences*, 94(12):6185–6190, 1997.

[114] M. E. Helgeson, M. D. Reichert, Y. T. Hu, and N. J. Wagner. Relating shear banding, structure, and phase behavior in wormlike micellar solutions. *Soft Matter*, 5(20):3858, 2009.

[115] Z. K. Zhang, N. Krishna, M. P. Lettinga, J. Vermant, and E. Grelet. Reversible gelation of rod-like viruses grafted with thermoresponsive polymers. *Langmuir*, 25(4):2437–2442, 2009.

[116] N. Krishna Reddy, Z. K. Zhang, M. P. Lettinga, J.K. G. Dhont, and J. Vermant. Probing structure in colloidal gels of thermoreversible rodlike virus particles: Rheology and scattering. *J. Rheol.*, 56(5):1153–1174, 2012.

[117] T. Iwataki, K. Yoshikawa, S. Kidoaki, D. Umeno, M. Kiji, and M. Maeda. Cooperativity vs. phase transition in a giant single dna molecule. *J. Am. Chem. Soc.*, 122(41):9891–9896, 2000.

[118] X. Zhu, C. Yan, F. M. Winnik, and D. Leckband. End-grafted low-molecular-weight pnipam does not collapse above the lcst. *Langmuir*, 23(1):162–169, 2007.

[119] V. Prasad, V. Trappe, A.D. Dinsmore, P. N. Segre, L. Cipelletti, and D. A. Weitz. Rideal lecture universal features of the fluid to solid transition for attractive colloidal particles. *Faraday Disc.*, 123:1–12, 2003.

[120] S.S. Li and C. M. Schroeder. Synthesis and direct observation of thermoresponsive dna copolymers. *ACS Macro Letters*, 7:281–286, 2018.

[121] K. N. Plunkett, X. Zhu, J. S. Moore, and D. E. Leckband. Pnipam chain collapse depends on the molecular weight and grafting density. *Langmuir*, 22(9):4259–4266, 2006.

[122] A. Hernandez-Garcia, D. J. Kraft, A. F. J. Janssen, P. H. H. Bomans, N. A. J. M. Sommerdijk, D. M. E. Thies-Weesie, Marco E. Favretto, R. Brock, F. A. De Wolf, and M. W. T. Werten. Design and self-assembly of simple coat proteins for artificial viruses. *Nat. Nanotechnol.*, 9(9):698, 2014.

[123] I. M. Storm, M. Kornreich, A. Hernandez-Garcia, I. K. Voets, R. Beck, M. A. Cohen Stuart, F. A. M. Leermakers, and R. de Vries. Liquid crystals of self-assembled dna bottlebrushes. *J. Phys.Chem.B*, 119(10):4084–4092, 2015.

[124] A. Hernandez-Garcia, N. A. Estrich, M. W. T. Werten, J. R. C. Van Der Maarel, T. H. LaBean, F. A. de Wolf, M. A. Cohen Stuart, and R. de Vries. Precise coating of a wide range of dna templates by a protein polymer with a dna binding domain. *ACS nano*, 11(1):144–152, 2016.

[125] I. Kirchenbuechler, D. Guu, N. A. Kurniawan, G. H Koenderink, and M. P. Lettinga. Direct visualization of flow-induced conformational transitions of single actin filaments in entangled solutions. *Nat. Commun.*, 5:5060, 2014.

Publications

H. Tang, T. Kochetkova, H. Kriegs, J. K. G. Dhont and M. P. Lettinga. Shear-banding in entangled xanthan solutions: tunable transition from sharp to broad shear-band interfaces. Soft Matter 2018, 14, 826-836.

H. Tang, E. Stiakakis, H. Kriegs, J. K. G. Dhont, and M. P. Lettinga. Tuning shear banding and wall slip by inter-molecular interactions in DNA brushlike polymer. In preparation.

FACULTY OF SCIENCE
DEPARTMENT OF PHYSICS AND ASTRONOMY
LABORATORY FOR SOFT MATTER AND BIOPHYSICS
Celestijnenlaan 200d box 2416
B-3001 Leuven
hu.tang@kuleuven.be
https://www.kuleuven.be/wieiswie/nl/person/00102866